Frequency reference based on acetylene spectroscopy in hollow core fibers and optical phase locks using FPGA based detection and feedback.

Guillaume Baclet

To cite this version:

Guillaume Baclet. Frequency reference based on acetylene spectroscopy in hollow core fibers and optical phase locks using FPGA based detection and feedback.. Physics [physics]. Université de Bordeaux, 2023. English. NNT : 2023BORD0284 . tel-04342798

HAL Id: tel-04342798
https://theses.hal.science/tel-04342798

Submitted on 13 Dec 2023

THÈSE PRÉSENTÉE

POUR OBTENIR LE GRADE DE

DOCTEUR
DE L'UNIVERSITÉ DE BORDEAUX

ÉCOLE DOCTORALE SCIENCES PHYSIQUES DE L'INGÉNIEUR

Spécialité LASERS, MATIÈRES ET NANOSCIENCES

Par **Guillaume BACLET**

Référence de fréquence basée sur la spectroscopie de l'acétylène dans des fibres creuses et asservissement de phase optique basée sur une détection et rétroaction par FPGA

Sous la direction de : **Philippe BOUYER**
et l'encadrement de: **Simon BERNON**

03/11/2023

Membres du jury :

Mr. Daniel BLOCH	DR, LPL, Paris	Président du Jury et Rapporteur
Mr. Jean-Francois CLEMENT	MdC, IEMN Lille	Rapporteur
Mr. Fetah BENABID	DR, XLIM, Limoges	Examinateur
Mr. Giorgio SANTARELLI	IR, LP2N, Talence	Examinateur
Mr. Benoit FAURE	CNES, Toulouse	Invité
Mr. Franck CORREIA	DR, DGA, Paris	Invité
Mr. Philippe BOUYER	DR, LP2N, Talence - Quantum Delta NLD	Directeur de thèse

Contents

Introduction

The field of precision metrology for time and frequency has witnessed significant progress in the recent decades, as atomic clocks allowed to achieve unprecedented levels of accuracy and stability [1]. The efforts toward extreme precision timekeeping stem from the critical role that it plays in a wide range of applications, that goes beyond fundamental scientific research, and includes satellite navigation systems [2], quantum sensing [3], telecommunications networks [4], inertial navigation [5], or even power distribution in smart grids [6]. In some of these applications, the need for high accuracy and portable, embedded time-frequency references have spurred interest in atomic physics solutions such as atomic clock that are at the forefront of time metrology.

Precise atomic clocks are essential for numerous applications that rely on accurate timekeeping. They serve as the foundation for global positioning systems (GPS), providing precise positioning and timing information for a multitude of applications [7]. For applications where the communication with an external satellite is prohibited such as for submarine positioning, cold atoms can be used to sense displacement. This is the basis of cold atoms based inertial navigation [8].

To advance cold atoms technology and address the demand for portable and embedded systems, researchers have focused on developing compact and transportable setups capable to operate in non-laboratory environments. These portable systems open up new possibilities for applications in areas such as geodesy [9] or navigation in remote locations [5]. To perform atom cooling, optical manipulation and imaging in such harsh conditions, there is a need for laser sources locked on absolute frequency references [10]. In current technology, these references are often made using free space atomic spectroscopy [11], which can be a detrimental solution for portability and robustness.

Fibered gas cells, made using hollow-core photonic crystal fibers (HC-PCFs), have emerged as a promising technology for achieving portable and embedded frequency reference for atom cooling [12]. HC-PCFs offer several advantages, including compactness, flexibility, and the ability to have a completely fibered laser system in the telecom range, including the emitting diodes to the frequency reference, amplifiers and modulators. This makes them a good candidate for an embedded frequency reference, and a platform to perform spectroscopic measurements.

These fibered cells provide a controlled and confined environment for the interaction between atoms and laser light. As they confine the light and allow to reach very high intensities and saturations, even in low optical power conditions, they facilitate highly sensitive spectroscopic measurements. Moreover, the small size and robustness of fibered cells make them suitable for field applications and harsh environments, presenting opportunities for portable atomic clock systems [13].

The goal of this PhD work is to leverage acetylene spectroscopy and fibered gas cells to develop a laser system capable of performing cold atom experiments based on Telecom laser [14]. In our efforts to improve the versatility, compactness and robustness of our solution, we tried to use FPGA (Field Programmable Gate Arrays) boards at their best for detection, modulation and locking. These FPGAs can provide answers to the need of versatility and portability of an embedded cold atom experiment while enabling for bandwidth demanding applications. The use of FPGA platform has also been extended in this work to create a simple architecture of optical phase lock loop for Raman beams. We achieve a low noise phase lock using the FPGA board itself for phase detection and feedback. Such phase lock development could be used to coherently manipulate atomic wave functions in transportable apparatus.

While we focus here on the cold atom application of optical phase lock loops (OPLL) [15], they have originally been developed for telecommunication applications [16]. Research on OPLL initially started with pursuit of robust coherent optical communication links for long-distance transmissions [17]. However, erbium doped fiber amplifier (EDFA) and challenges associated with the implementation of OPLL dampened the enthusiasm for coherent communication at that time [18] [19]. Nevertheless, there has been a recent resurgence of interest in OPLL research, driven by its potential applications in specialized fields like free-space intersatellite optical communication links [20] and high-bandwidth optical communication [21].

This manuscript will be divided in two parts, the first part focuses on the spectroscopy of HC-PCF filled with acetylene gas for laser frequency stabilisation, and the second part, focuses on the building and evaluation of an OPLL architecture centred around a FPGA to build phase coherent lasers.

In the first part, we start by presenting existing solutions of frequency standard based on the molecular gas spectroscopy. We then present the theoretical background for the modulation transfer spectroscopy technique we have used to lock a laser to a free space reference and to an HC-PCF cell. We discuss the role of the fiber geometry and design on the spectroscopy signal we expect to observe. We then present the tools we have developed to measure and characterize the frequency stability.

A second chapter in this part presents the experimental setup used to implement the modulation transfer spectroscopy on telecom lasers, as well as the measurements of the external parameters, measured coincidentally with the frequency of the locked laser. The effect of those external parameters are quantified by varying every parameter independently in a controlled way while monitoring the laser's frequency stability. The results of these measurements are presented in a third chapter, and are used to characterize the final frequency stability measurements.

The first chapter of the OPLL part will present the background of Raman transition and the need for phase coherent laser. It also discusses the physics of semiconductor lasers frequency tuning in external cavity configurations. The different architecture possible for OPLLs are presented in this chapter with a focus on digital OPLLs. The tools used for phase stability measurements and characterisation are then presented. In the last section of this chapter, we present the experimental setup that has been used to lock the lasers.

The second chapter presents the transfer function of the OPLL. The impact of the laser and FPGA board on the final phase stability is then discussed. In particular, this chapter compares the performance of the phase lock method we have developed for:

- Two commonly used sets of lasers (2×780 nm External Cavity Diode Laser (ECDL) and 2×1533 nm RIO Plannex laser diodes)
- Two commercially available FPGA boards with embedded analog to digital and digital to analog conversion components (Red Pitaya 14 bits and ALPHA250 from Koheron)

We discuss in particular the specific characteristics of the lasers and boards that most strongly affect the loop performance. Finally, the result of the phase stability achieved with our digital OPLL is presented and discussed.

Part I

Acetylene Spectroscopy in hollow core fibers

Chapter 1

Theory of molecular spectroscopy in hollow-core fibers

1.1 Acetylene frequency standards

In atom optics experiments, the electronic transitions that are used to manipulate the external and internal degrees of freedom are addressed by single-frequency, narrow linewidth lasers emitting at specific wavelengths. Due to environment fluctuations, the frequency of these lasers fluctuates out of the acceptable frequency range. For typical laser cooling purpose, the frequency stability should be better than the natural width of the transitions. For the electronic orbital transition between the first levels of the alkali, the linewidth is of the order of few megahertz. [22]

For such laser cooling applications, there is then a need to lock the laser to an absolute frequency reference. In general the lasers used emit directly at the wavelengths of the targeted transitions, at the limit of the visible and the infrared. The lasers frequencies are therefore directly referenced to the atomic transition they are supposed to control. This is achieved by deriving part of the beam towards a saturated absorption optical setup. This type of bench performs sub-Doppler spectroscopy of a cell containing atomic vapor of the atom of interest [23]. The other part of the beam can then be finely and quickly tuned to nearby frequencies using acousto-optic modulators (AOM) or electro-optic modulators (EOM) as needed.

If this solution works well for Rubidium (Rb) and Caesium (Cs), it is less efficient for other species such as Potassium (K). Indeed, the hyperfine structure of K atom is so close together that the different transitions are separated by less than the natural width of the state line [24]. The spectroscopy usually mixes the hyperfine signals and it is difficult to discriminate on which transition the control is carried out.

Over the past 10 years a new type of frequency doubled telecom laser have been developed for Rb and K experiments. The transition of interest for atomic cooling of Potassium is indeed at 766 nm and that of Rubidium at 780 nm. These wavelengths are accessible by laser frequency the telecom radiation at respectively 1533 nm and 1560 nm. Furthermore, in this range, it is possible to achieve high power using fiber amplifier technology doped with Erbium ions (EDFA). These laser architectures have the advantage of being compact, powerful, and very robust, while having good spectral properties and being agile in frequency.

For these architectures, it is interesting to look for new references allowing to directly lock their frequency in the telecom range. The typical requirement is to obtain a long term stability better than ~ 200 kHz, which represents a relative stability $\lesssim 10^{-9}$.

Contrary to alkali species for which the transitions are between electronic orbitals and therefore hold a large electronic dipole strength, the acetylene transition in the C-band corresponds to rotational and vibrational excitation of the molecule which are weakly coupled to electromagnetic waves. Such transitions have small electric dipole strength and long lifetime that make them appealing to realize a good frequency reference.

The most abundant isotope of acetylene is $^{12}C_2H_2$ with above 97% occurrence. This isotope of acetylene is a good candidate for a frequency reference [25] in the C-band for many telecom application [26]. It presents some transition, (P14 and P24), very close to the double of the Potassium D2 and D1 transitions respectively. One should note that the acetylene isotope $^{13}C_2H_2$ has been proposed as a secondary representation of the second by the BIPM (P16) [27].

By using acetylene-filled free space cells for spectroscopy and laser locking, precise frequency stabilization within the telecom band has already been achieved, with performance reaching fractional frequency instabilities down to $4\ 10^{-13}$ at 1s [28], [29], [30].

In the next two sections we discuss the specificity and the main characteristics of free space and fibered cells [25] [31].

1.1.1 Free space cells

Free space cells or bulk glass cells are commonly used for frequency reference. The primary purpose of these glass cells is to securely hold and protect the gas, maintaining it at an appropriate pressure and purity required for high precision spectroscopic measurements. The cell is most of the time composed of glass with sometimes the addition of quartz or sapphire windows depending on the exact application's needs of the spectroscopy realised. Glass has the advantage to be very chemically stable and seldom absorbs the molecules.

Bulk cells are often build with wedged windows to prevent reflection and minimize unwanted optical interference effects, such as Fabry-Perot interference fringes, which could add unwanted components to the spectroscopy signal detected using.

As detailed below, for our targeted performance, we need a low pressure (1 Pa) pure acetylene cell, which can be a challenge to manufacture. We were able to obtain such a cell thanks to the Institute of Scientific Instruments of the Czech Academy of Sciences.

To enhance the spectroscopy in the bulk cells, many techniques were developed to increase the interaction length between the light and the sample. Multi-pass cells like the Herriott cell [32] allow for long interaction path in a restricted volume. Indeed, using mirrors placed around the gas cell, the beams can be reflected to optimally pass multiple times in the volume. Deferent design for multi-pass cell were proposed such as the White cell [33], the Robert cell [34] or a toroidal multipass cell [35] as shown in Fig 1.1.

Advancements in micro-fabrication techniques have also allowed for the development of miniaturized bulk cells [10]. Compact cells offer portability and integrability allowing for robust and accurate frequency reference for embedded systems [36] (see Fig 1.2a). A limitation for these micro-fabricated cell is the limited interaction length. This limited length can be partially compensated by increasing the atom-light interaction using guided modes on a chip, that confine strongly both the gas and the light [37] as shown in Fig 1.2b.

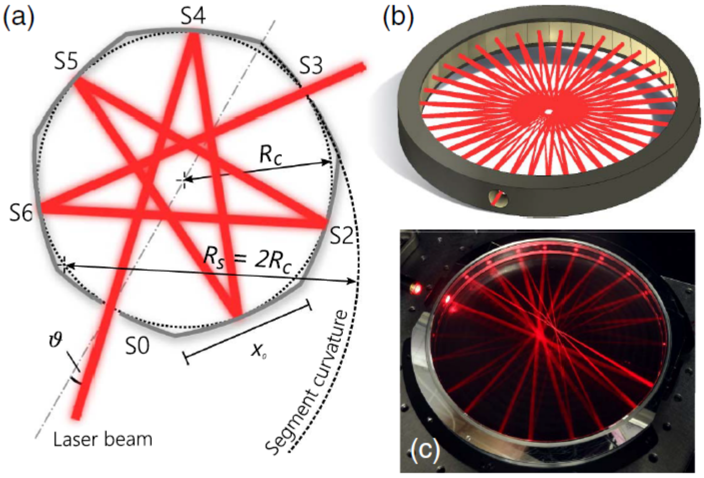

Figure 1.1: Herriott cells examples. Multipass toroidal cell for spectroscopy as described in [35]

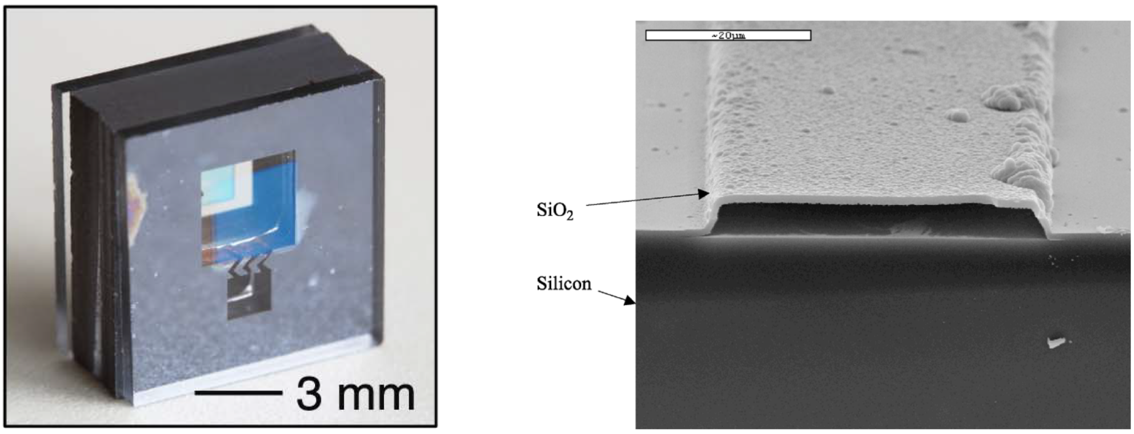

(a) (b)

Figure 1.2: Microfabricated cells. (a) A microfabricated cell for spectroscopy [36]. (b) A cell on a chip using guided modes of light [37].

1.1.2 Fibered cell

The idea to use guided modes of light to increase the interaction between the light and the gas has been naturally extended to the use of hollow core fibers. Fiber optics in the telecom band have long since demonstrated exceptionally low loss performances that allowed long distances signal transmission. It is now ubiquitous. Furthermore by creating a fully fibered gas frequency reference, one would allow to enhance the frequency stability and precision of lasers with an integrated and ready to use solution.

The need for a gas reference in the fiber makes hollow-core fiber an ideal candidate for these applications. Hollow-core fibers offer the advantages of both convenience of use, and very long interaction length, as a fews kilometres of fiber can easily fit in a small container once the fiber is winded up.

However, as discussed in section 1.3, careful consideration has to be taken when designing a hollow core fiber based spectroscopy cell. Among other critical points, hollow-core fiber exhibit multimode behaviour [38] which are detrimental for spectroscopy performance [31].

Furthermore the filling and closing of these fibers has proven to be a challenge, with many solutions proposed and studied [39], [38]. The closing issue can be circumvented using vacuum boxes at each fiber end and injecting the light in the fiber as one would do with a regular bulk cell [40]. If performant, this solution is however not satisfying for harsh environment as it obliges to go through a free space injection and prevent an all fibered integration.

Nevertheless, hollow-core fiber have proven to be good candidate for frequency stability application, and the possibility to integrate a frequency reference to a fully fibered, robust telecom laser system has motivated the study of the spectroscopy of gas in these fibers. Stability achieved using hollow-core fibers are not comparable to the one of spectroscopic bulk cells, but some work have shown fractional frequency stability of $3\ 10^{-12}$ [31] at 1s. This is very promising for laser cooling applications that typically require, $\sim 10^{-10}$ to achieve Bose-Einstein Condensation in laboratory conditions.

1.2 Theory of sub Doppler spectroscopy

1.2.1 Rovibrational molecular transitions

The fundamentals of molecular spectroscopy are quite similar to atomic spectroscopy. However, while alkali atoms absorb light in the 10^{14} Hz range through electronic transitions, molecules such as C_2H_2 have transitions in the IR range through rovibrational transitions. These transitions correspond to the change in vibrational and rotational states of the molecules. In Fig 1.3 we illustrate the different type of vibrational modes. In this work, we will focus on the spectroscopy of $\nu_1 + \nu_3$ modes as the frequency of these modes is close to the C telecom band, and close to the double of potassium transition used in atomic cooling around 1533 nm. The additional existence of rotational modes give rise to a comb like structure depicted in Fig 1.5

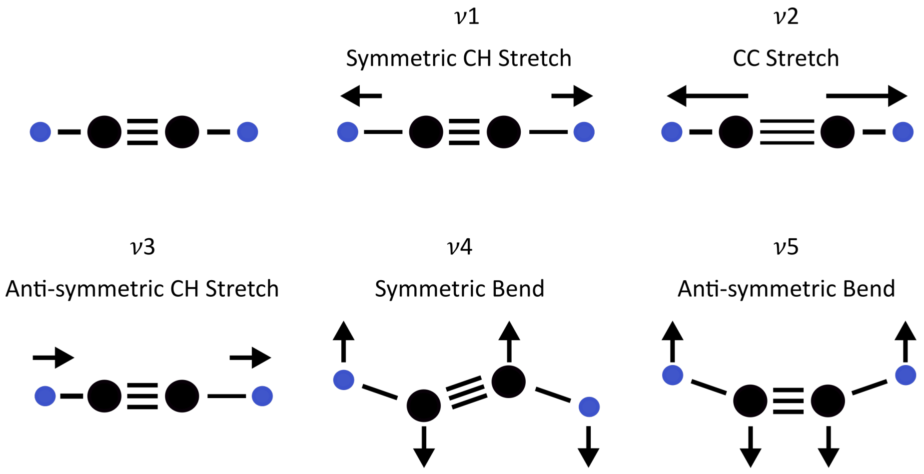

Figure 1.3: Vibrational modes of the acetylene molecule. Each mode is resonant at a specific frequency. For the 1533 nm region, the combination $\nu_1 + \nu_3$ is responsible for the absorption. Each vibrational mode gives a comb of transition due to rotational modes.

The ro-vibrational transitions are grouped in three branches P,Q and R. All corresponding to different types of transitions. A molecule has many rotational levels "J" on every vibrational level. Due to selection rule [41], level $(\nu = 0, J)$ can only couple to a level $(\nu' = 1, J')$ with $\Delta J = J' - J = \pm 1, 0$. For each value of ΔJ corresponds a different branch P, Q or R. We are interested in this work in a specific transition of the P branch $(\Delta J = +1)$ (see Fig 1.4).

Notably, one can see that the P and R branch on Fig 1.5 have a particular shape. This is due to the thermal distribution of the different rotational levels of the gas as the envelope of the lines show a Maxwellian distributions. The inner structure of lines of even parity having a lower intensity is due to symmetry consideration of the molecule [41].

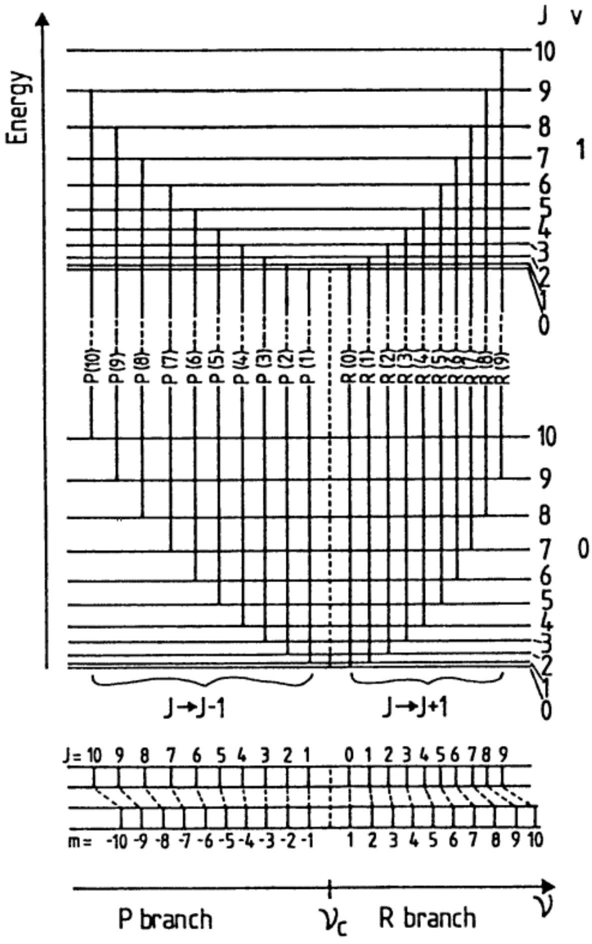

Figure 1.4: Vibrational-rotational spectrum when the rotational constant is smaller in the upper vibrational state. Figure taken from reference [41] in chapter 4.

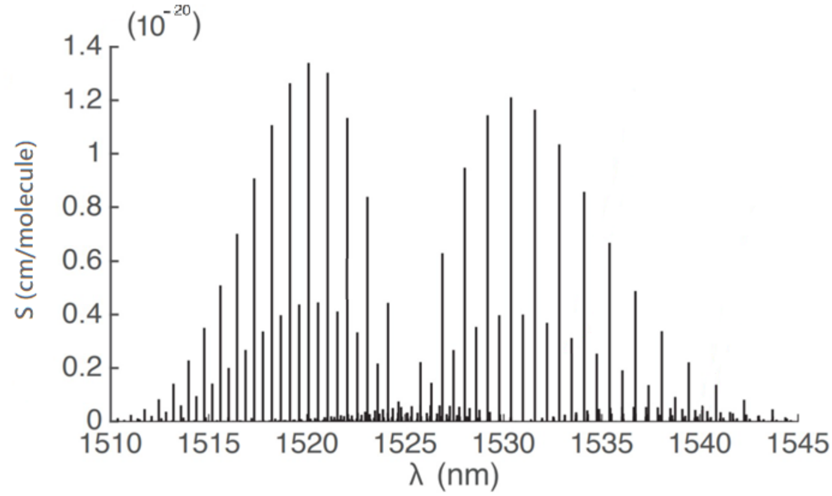

Figure 1.5: Absorption lines intensities for one molecule of acetylene per unit of volume, in the units of the HITRAN database [42] (centimetre–gram–second system of units).

1.2.2 Doppler effect

Due to thermal agitation, all the molecules have different velocities. Due to Doppler effect this means that the resonant frequency of every molecule will be different in the lab framework. The apparent shift will be proportional to the scalar product of the wavevector of the incident wave and the speed vector of the molecule. The lineshape of the broadened transition will thus follow the same distribution as the speed distribution for a thermal cloud (gaussian) (see Fig 1.6). This type of broadening is called "inhomogeneous" as the contribution of the molecules is different for every velocity classes. By selecting molecules of particular velocity classes, one can reduce this broadening.

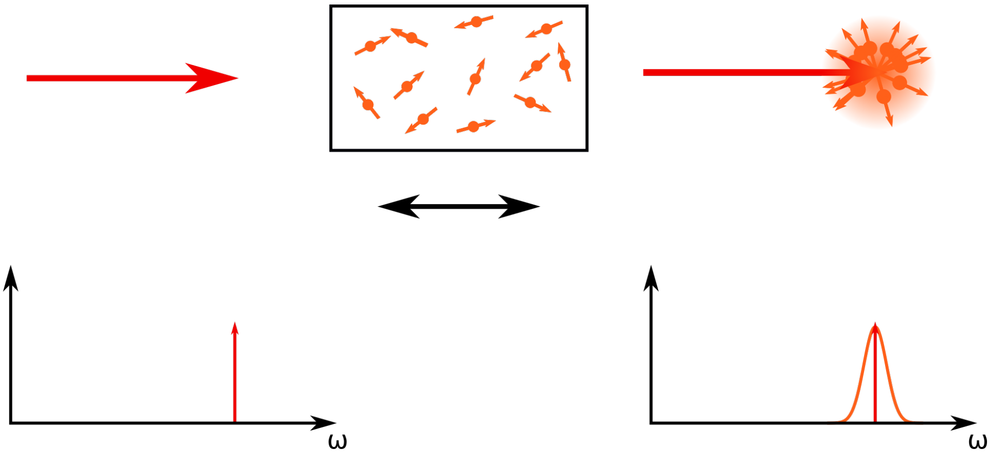

Figure 1.6: Representation of the Doppler effect. The different speeds in the cloud leads to different effective frequency observed by the molecules. The distribution in speeds get imprinted on the absorbed beam that goes through the gas, as each individual molecule resonance is shifted through Doppler effect.

Several techniques exist to reduce the lineshape of a broadened transition. We detail below the principles of a few of these methods, saturated absorption spectroscopy (SAS) [43], electromagnetically induced transparency (EIT) [44], coherent population trapping (CPT) [45], Ramsey interferometry [46], [47]...

EIT is a technique using a three state configuration ($|1\rangle$, $|2\rangle$, $|3\rangle$). One strong pump beam couples two states (i.e $|2\rangle \rightarrow |3\rangle$) in such a way that it creates a Autler-Townes doublet. This opens a transparency window for a second probe beam tuned on resonance with the transition $|1\rangle \rightarrow |2\rangle$ [44] The width of the transparency window is equal to the Rabi frequency of the pump beam.

CPT requires a similar 3 level structure than EIT. The intensities of both beams used are equal. For CPT, both beams have the same Rabi frequency and contribute the same in the diagonalization of the Hamiltonian creating an effective dark state. To create this dark state, phase coherence of the laser is important as it is created through interference between the two optical transitions (which was not a requirement for EIT as the probe beam does not contribute to the Autler-Townes doublet) [48].

EIT is observed as the transmission of a probe beam, while CPT is observed as the decrease in fluorescence of the atoms, that are in the dark state.

We develop below in detail on saturated absorption spectroscopy that has a closer link to the method used in this work. This techniques uses two contra-propagating beams, one called a "pump" beam which will saturate the transition for a specific resonating class of speed, and another beam called the "probe" beam which is absorbed by the medium and exhibit a so called Lamb dip, at the frequency where the Doppler effect cancels out the detuning of the probe and pump beams 1.7.

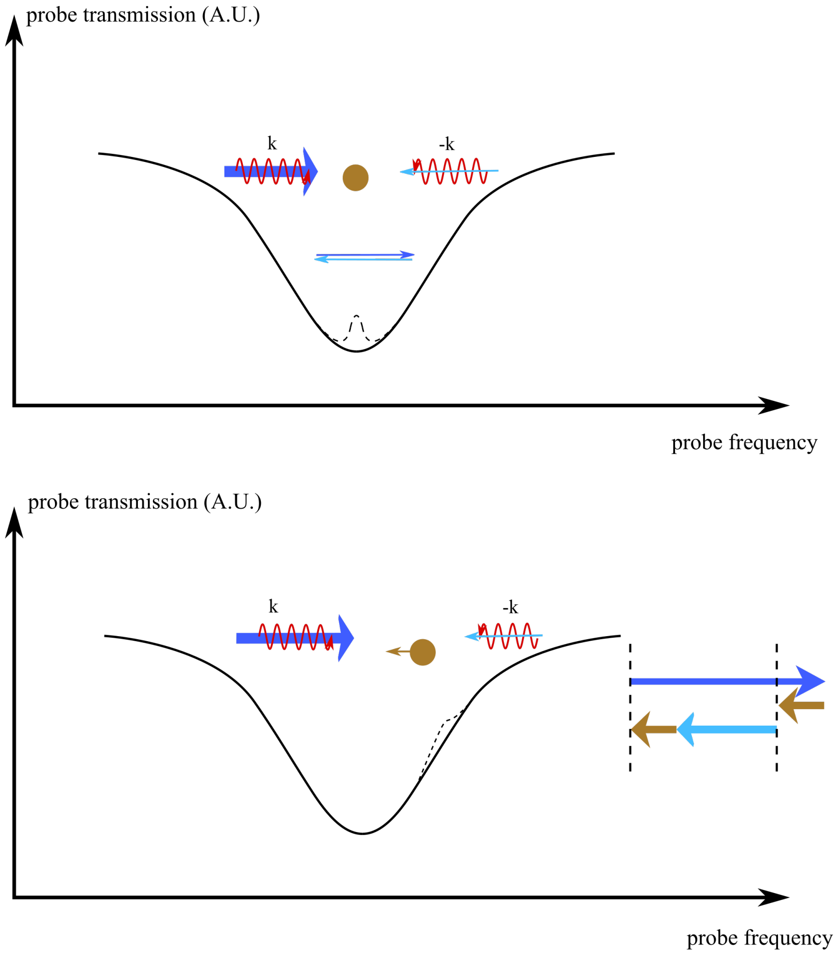

Figure 1.7: Representation of the SAS velocity class selection. The Doppler broadened profile can be reduced by addressing only one class of speeds in the cloud. In order to do so, a beam is send in one direction, saturating one class of speed. When another beam is sent through the medium, the transmission profile will show a local maximum for this saturated velocity class. (a) When both pump and probe have the same frequency, the Lamb dip is centered on the zero velocity class (b) for different frequencies of pump and probe a certain non zero velocity class can be resonant simultaneously with both beams. Most of the time, retroreflected beams are used to address the zero velocity class.

The absorption lineshape observed in SAS is a Lorentzian function. The SAS dispersion-like signal obtain using lock in detection is most often used in AMO experiments as an error signal for frequency locking. Indeed by using a feedback loop on this signal, one can use the spectroscopy of an atomic cloud to stabilise the frequency of a laser.

SAS is one of the most simple technique one can use for laser stabilisation on a molecular or atomic reference, it is however sensitive to many sources of noise and fluctuations.

We present below another technique based on four-wave mixing in a gas, that is more suitable for our need of high precision spectroscopy in hollow-core fibers.

1.2.3 Modulation Transfer Spectroscopy

Modulation transfer spectroscopy is a sub-Doppler technique that uses the non linearity of a medium to mix two contra-propagating beams, resulting in a coherent electromagnetic field with a modulation *copied* from onto the other beam. In this section we detail the calculation of the lineshape one can expect using modulation transfer spectroscopy (MTS) as detailed in [49], [50] and [51].

In section 1.2.3.1 we first model the ro-vibrationnal transition of acetylene as a two level system (TLS) coupled with the electric field. Secondly, in section 1.2.3.2, we describe the light-matter interaction for an optically thin molecular gas sample as in [52]. Then in section 1.2.3.3 we use a third-order development of the density matrix to obtain an expression of the reemited modulated field.

1.2.3.1 Two level system interacting with an electric field

We consider the molecular gas to be a collection of two-level systems, coupled to an electromagnetic field. We first expand on the description of each individual TLS. Statistical mixtures of TLS are studied in section 1.2.3.2 where we perform a velocity average.

The two states $|a\rangle$ and $|b\rangle$ are described by two independent wave functions Ψ_a and Ψ_b respectively. The states are separated in energy by a quantity $\hbar\omega_0$ with ω_0 the *transition frequency*.

The two level system could be described by a wave function $\Psi(t)$ such that, in the absence of decoherence,

$$|\Psi(t)\rangle = a(t)\,|\Psi_a\rangle + b(t)\,|\Psi_b\rangle\,. \tag{1.1}$$

$\Psi(t)$ is a so called *pure state*. To account for decoherence processes, we describe the TLS's evolution using the density operator. This operator can be represented by a density matrix $\rho(t)$ in the $\{\Psi_a,\,\Psi_b\}$ basis, as

$$\rho(t) = \begin{pmatrix} \rho_{aa} & \rho_{ba} \\ \rho_{ab} & \rho_{bb} \end{pmatrix} = \begin{pmatrix} aa^* & ab^* \\ ab^* & bb^* \end{pmatrix}. \tag{1.2}$$

One can note that the diagonal elements of the density matrix represent the *populations*, which are the probabilities of finding the TLS in the states $|a\rangle$ or $|b\rangle$. And the off diagonal elements are the *coherences* that describes the phase relationship between the two states and are related to the dipole moment of the TLS. In the following we aim at calculating the density matrix's expression, as it is directly linked to the reemited field we want to determine.

The population of states a and b are assumed to have an exponential decay [53]. We note γ_a and γ_b the decay constant of probability amplitudes a and b respectively, and γ_{ab} the decay constant of the dipole moment of the TLS. In the absence of any broadening mechanisms, the relation $\gamma_{ab} = \frac{1}{2}(\gamma_a + \gamma_b)$ is verified [52]. γ_{ab} is the decay constant of the dipole moment, it measures the damping of the TLS coherence that result in an uncertainty in the TLS transition frequency. Therefore the quantity γ_{ab} is also called the homogeneous linewidth.

However in the case of this study, broadening mechanisms will be accounted for such that one finds $\gamma_{ab} \geq \frac{1}{2}(\gamma_a + \gamma_b)$. γ_a, γ_b and γ_{ab} will therefore be considered independent. The so called broadening mechanisms will be detailed further in section 1.3, for now we only consider that it changes the homogeneous spectral linewidth γ_{ab}.

Additionally, because we are working with molecular gases represented by a statistical mixture of TLS, we have to consider a broadening caused by the different velocities of the molecules. Each individual molecule's resonance frequency is shifted due to Doppler effect which causes a broadening of the apparent linewidth. As this type of broadening is caused by the statistical mix of different TLS, this broadening will be called *inhomogeneous*, in opposition to the *homogenous* broadening which was the same for each TLS considered.

To describe the interaction between the electric field and the TLS, we consider the TLS in the presence of an electric field $\overrightarrow{E} = E\exp(i\omega t)$. The interaction between the two-level system and the field can be very well approximated by an interaction Hamiltonian $H_{int} = -\hat{\mathrm{d}}.\overrightarrow{E}$ where $\hat{\mathrm{d}}$ is the electric dipole moment.

$\hat{\mathrm{d}}$ can be thought as an analogous of the classical dipole moment which is the *displacement* of the charge in the dipole. Here $\hat{\mathrm{d}}$ does not describe an actual displacement, but a change in the position distribution of the charge in the molecule for different states. For parity arguments of the electric dipole moment, only the off diagonal elements of $\hat{\mathrm{d}}$ are non zero. Furthermore, as the transition dipole moment is a measurable quantity, the relation $\langle a|\hat{\mathrm{d}}|b\rangle = \langle b|\hat{\mathrm{d}}|a\rangle^*$ is satisfied. We note this quantity $p = \langle a|\hat{\mathrm{d}}|b\rangle$ in reference to the *polarisability* which will be defined later.

Introducing this quantity to describe the interaction between the TLS and the electric field allows us to describe the evolution of the system using the optical Bloch equations [54]

$$\dot{\rho}_{aa} = -\gamma_a \rho_{aa} - i\frac{pE}{\hbar}(\rho_{ab} - \rho_{ba}); \tag{1.3}$$

$$\dot{\rho}_{bb} = -\gamma_b \rho_{bb} + i\frac{pE}{\hbar}(\rho_{ab} - \rho_{ba}); \tag{1.4}$$

$$\dot{\rho}_{ab} = -(\gamma_{ab} + i\omega_0)\rho_{ab} - i\frac{pE}{\hbar}(\rho_{aa} - \rho_{bb}); \tag{1.5}$$

$$\rho_{ba} = {\rho_{ba}}^*. \tag{1.6}$$

We now have modelled the evolution individual TLS and its interaction with the electric field, we can now look at the evolution equation for a statistical mixture of the gas.

1.2.3.2 Flux of density matrices

We have described the molecules as TLS density matrix and derived their equation of evolution under an electromagnetic field drive. Now we aim at reversing the problem and calculating the electric field emitted by a gas of molecules described by a collection of density matrices. In the following we will first represent the molecular gas by a distribution of density matrices with different states, describing their specific velocities and initial conditions. We will then obtain the polarisability in every point of space at a given time by integrating the distribution of density matrices to account for the flux of molecules at this specific position. Then by integrating the local polarisabilities over the whole sample, we will retrieve the global polarisability. This global polarisability corresponds to a source dipole that reemits electric field that is accounted for in the Maxwell's equations.

A molecule in the gas is characterised by its initial state ($\alpha = a$ or b), at the time t_0 when it was a position z_0 with velocity v. Neglecting collision between molecules, we can consider the velocity v constant for each molecule. Due to its interaction with the electromagnetic field and the environment, the density matrix of this molecule will evolve over time. We note

$$\rho = \rho(\alpha, z_0, t_0, v; t) \tag{1.7}$$

the density matrix at time $t > t_0$ of a particle that was in state $|\alpha\rangle$, position z_0 and velocity v at time t_0.

The polarisation P being the density of dipole moments, it can be calculated using the expected value of the transition dipole moment $\hat{\mathrm{d}}_{ab}$,

$$\langle \hat{\mathrm{d}}_{ab} \rangle = \mathrm{Tr}(\rho \hat{\mathrm{d}}_{ab}) = p[\rho_{ab}(\alpha, z_0, t_0, v; t) + \rho_{ba}(\alpha, z_0, t_0, v; t)], \tag{1.8}$$

where $p = \langle a| \overrightarrow{\mathrm{d}} |b\rangle$.

To deduce the macroscopic polarisation of the medium at position z and time t (z, t), one needs to sum the contribution of every molecule at (z, t) regardless of the state α, position z_0, time t_0 and velocity v of excitation.This means that the density matrices (expression 1.7) need to be summed over α, z_0, t_0, v, and evaluated for (z, t).

In order to integrate the density matrices, we introduce $\lambda_\alpha(v, z_0, t_0)$ as the number of molecules in the α state per unit of time and unit of volume. We have then

$$\rho(v, z, t) = \sum_{\alpha=a,b} \int_{-\infty}^{t} dt_0 \int dz_0 \lambda_\alpha(v, z_0, t_0) \rho(\alpha, z_0, t_0, v; t) \delta(z - z_0 - v(t - t_0)), \tag{1.9}$$

Where δ is the Dirac distribution.

If we assume that λ_α does not vary over time and space in the cloud (i.e in a homogeneous cloud), it can be taken out of the integral, which gives

$$\rho(v, z, t) = \sum_{\alpha=a}^{b} \lambda_\alpha(v) \int_{-\infty}^{t} dt_0 \rho(\alpha, z - v(t - t_0), t_0, v; t), \tag{1.10}$$

The density matrices that we have described represent molecules in the gas with different velocities. To derive the evolution of the system, one needs to take into account the molecules going in and out of a infinitesimal element of space which is represented by the flux derivative

$$\partial = (\partial/\partial t) + v(\partial/\partial z). \tag{1.11}$$

that accounts for both purely temporal evolution (EM field interaction, collisions) and flux contributions.

Applied to the partial density matrices and by inserting the derivative in the integrand, we get the quantity

$$\begin{aligned}\partial\rho(v,z,t) = \sum_{\alpha=a}^{b}\lambda_\alpha(v)\rho(\alpha,z,t,v;t) + \sum_{\alpha=a}^{b}\lambda_\alpha(v)\Bigg[\int_{-\infty}^{t}\Bigg(\frac{\partial}{\partial t}\rho(\alpha,z-v(t-t_0),t_0,v;t)\\ - v\frac{\partial}{\partial z}\rho(\alpha,z-v(t-t_0),t_0,v;t)\Bigg)dt_0\Bigg] + v\frac{\partial}{\partial z}\rho(v,z,t),\end{aligned} \tag{1.12}$$

$$\begin{aligned}\partial\rho(v,z,t) &= \sum_{\alpha=a}^{b}\lambda_\alpha(v)\rho(\alpha,z,t,v;t) + \sum_{\alpha=a}^{b}\lambda_\alpha(v)\Bigg[\int_{-\infty}^{t}\frac{\partial}{\partial t}\rho(\alpha,z-v(t-t_0),t_0,v;t)\\ &\quad - v\frac{\partial}{\partial z}\rho(\alpha,z-v(t-t_0),t_0,v;t)dt_0\\ &\quad + \int_{-\infty}^{t}v\frac{\partial}{\partial z}\rho(\alpha,z-v(t-t_0),t_0,v;t)dt_0\Bigg]\\ &= \sum_{\alpha=a}^{b}\lambda_\alpha(v)\rho(\alpha,z,t,v;t) + \sum_{\alpha=a}^{b}\lambda_\alpha(v)\int_{-\infty}^{t}\frac{\partial}{\partial t}\rho(\alpha,z-v(t-t_0),t_0,v;t)dt_0,\end{aligned} \tag{1.13}$$

We need to sum over the different quantum states. We remind that the time t_0 in the third argument of $\rho(\alpha,z_0,t_0,v,t)$ is the time at which the TLS gets excited in the state α. Therefore it follows directly that

$$\rho(\alpha,z,t,v,t) = \begin{pmatrix}\delta_{a\alpha} & 0\\ 0 & \delta_{b\alpha}\end{pmatrix} \tag{1.14}$$

Where $\delta_{\alpha\alpha}$ is the Kronecker symbol. We can write the first term of eq 1.13 as a matrix

$$\sum_{\alpha=a}^{b}\lambda_\alpha(v)\rho(\alpha,z,t,v;t) = \begin{pmatrix}\lambda_a & 0\\ 0 & \lambda_b\end{pmatrix} \tag{1.15}$$

To link this density matrix flux element to the electric field we combine eq 1.15 for the first part of eq 1.13 and optical Bloch equations 1.3 to 1.6 for the second part, we get

$$\partial\rho_{aa} = \lambda_a - \gamma_a\rho_{aa} - i(\frac{pE(z,t)}{\hbar}(\rho_{ab}(v,z,t) - \rho_{ba}(v,z,t))), \tag{1.16}$$

$$\partial\rho_{bb} = \lambda_b - \gamma_b\rho_{bb} + i(\frac{pE(z,t)}{\hbar}(\rho_{ab}(v,z,t) - \rho_{ba}(v,z,t))), \tag{1.17}$$

$$\partial\rho_{ab} = \rho_{ab}(i\omega_0 - \gamma_{ab}) - i(\frac{pE(z,t)}{\hbar}(\rho_{aa}(v,z,t) - \rho_{bb}(v,z,t))), \tag{1.18}$$

$$\rho_{ba} = \rho^*_{ab}, \tag{1.19}$$

We now have a system of differential equations describing the local populations and coherences and their relation to the electric field. We can then write these equations in term of partial polarisation

$$P(v,z,t) = p[\rho_{ab}(v,z,t) + \rho_{ba}(v,z,t)], \tag{1.20}$$

It appears that only the knowledge of the coherences is necessary to get an expression of the polarisability. We will develop in the last part the expression of the coherences. We give first the explicit link between the polazisability of the medium and the reemitted electric field using Maxwell's equations.

One can find the relationship between the electric field $E(z,t)$ and the polarisation $P(z,t)$ using the wave equation obtained via the Maxwell equations in matter (with $D = \epsilon_0 E + P$):

$$\nabla^2 \wedge E + \frac{1}{c^2}\frac{\partial^2 E}{\partial t^2} = -\mu_0 \frac{\partial^2 P}{\partial t^2} \tag{1.21}$$

If we consider the case of a monochromatic wave

$$E(z,t) = \mathcal{E}(z,t)\cos(\omega t - kz) \tag{1.22}$$

where the frequency ω is assumed close to the transition frequency ω_0, and much larger than the transition linewidth, we can decompose the induced polarization in two quadrature components, in phase and out of phase with the incident E field

$$P(v,z,t) = \mathcal{S}(v,z,t)\sin(\omega t - kz) + \mathcal{C}(v,z,t)\cos(\omega t - kz) \tag{1.23}$$

The polarization $P(v,z,t)$ is linked to the field emitted by a dipole excited by the field $E(z,t)$, $P(v,z,t)$ is mostly in phase opposition, meaning $S \ll C$ (see [52]). In this approximation S is directly the amplitude of $P(v,z,t)$. We then use the notation $\mathcal{P} = S$. Assuming slowly varying envelope approximation (SVEA) for E ($\frac{\partial\mathcal{E}}{\partial t} \ll \omega\mathcal{E}$; $\frac{\partial\mathcal{E}}{\partial z} \ll k\mathcal{E}$; $\frac{\partial\mathcal{P}}{\partial t} \ll \omega\mathcal{P}$), we can neglect the higher order derivatives in the wave equation 1.21. we obtain

$$k\frac{\partial E}{\partial z} - \frac{k}{c}\frac{\partial E}{\partial t} = -\mu_0\omega^2 P \tag{1.24}$$

and considering $P(v,z,t)$ is in quadrature of $E(z,t)$ we can simplify the cos and sin in the expression 1.22 and 1.23 and we obtain

$$k\frac{\partial\mathcal{E}}{\partial z} - \frac{k}{c}\frac{\partial\mathcal{E}}{\partial t} = \frac{-ik^2}{2\epsilon_0}\mathcal{P} \tag{1.25}$$

Under the assumption that the fields and polarization do not vary along the sample, one assumes $\mathcal{E}$ and $\mathcal{P}$ as z independent. In the steady state we obtain

$$\mathcal{E} = -\frac{ikL}{2\epsilon_0}\mathcal{P} \tag{1.26}$$

The equation 1.26 obtained here can be used to described how an electric field is generated by a polarization in a medium. Therefore, to calculate the field reemitted by the molecules, one can calculate the polarization imprinted on the molecular gas by the spectroscopy field, and use relation 1.26.

We now have the expression of the reemitted electric field as a function of the polarization, and an expression of the polarization as a function of the density matrices coherences (eq 1.20). We develop in the next part on the third order development of the density matrix, to express the coherences in the presence of the pump and probe MTS laser beams.

1.2.3.3 Third order development of density matrix in the presence of 3 perpetuating electric fields

We describe here the four wave-mixing (FWM) involved in the emission of the MTS signal. Two sidebands of a modulated beam and a third contra-propagating beam (the probe) mix in the medium to generate a fourth wave that can be measured through a beatnote with the third beam. We first describe the three electric fields involved in the FWM then, to have an expression of the measured signal's lineshape, we need a third order development of the density matrix. The third order density matrix element is the non linear term responsible for the FWM process.

For sub-Doppler MTS, two contra-propagating beams are used : a modulated pump beam and an unmodulated probe beam.

The unmodulated probe can be written

$$E_{probe} = \frac{1}{2}\mathcal{E}_0 e^{i(\omega t + k_s z + \varphi_0)} + cc, \tag{1.27}$$

and the modulated pump can be written

$$E_{pump} = \frac{1}{2}\mathcal{E}_{pump} e^{i(\omega+\Delta)t + Msin(\Omega t) - k_p z + \varphi} + cc, \tag{1.28}$$

with Δ the frequency shift between the probe and the pump, Ω the modulation frequency and M the modulation factor. This expression can be expanded as a Fourier serie

$$E_{pump} = \frac{1}{2}\mathcal{E}_{pump} \sum_{n=-\infty}^{+\infty} J_n(M) e^{i(\omega+\Delta+n\delta)t - k_p z + \varphi_n} + cc, \tag{1.29}$$

where J_n is the Bessel function of order n of the first kind.

In the following we will only consider two sidebands of the pump interacting with the probe, and then sum over all possible couple of sidebands in the pump beam. The two considered sidebands will be expressed as

$$E_{\pm} = \frac{1}{2}\mathcal{E}_{\pm} e^{i((\omega+\Delta+n_{\pm}\delta)t - k_p z + \varphi_{\pm})} + cc. \tag{1.30}$$

To describe the non linear interaction in the medium in term of four wave-mixing, we consider the process in which two sidebands of the pump and the probe interact. Due to the phase matching condition in a FWM process, the sum of the wave-vectors of the fields involved needs to be 0. This means that one photon of the pump needs to be absorbed and one reemitted, and one photon of the probe is absorbed. In this condition the resulting wave respects the phase matching condition with a reemitted wavevector in the direction of the probe [55] (see Fig 1.9).

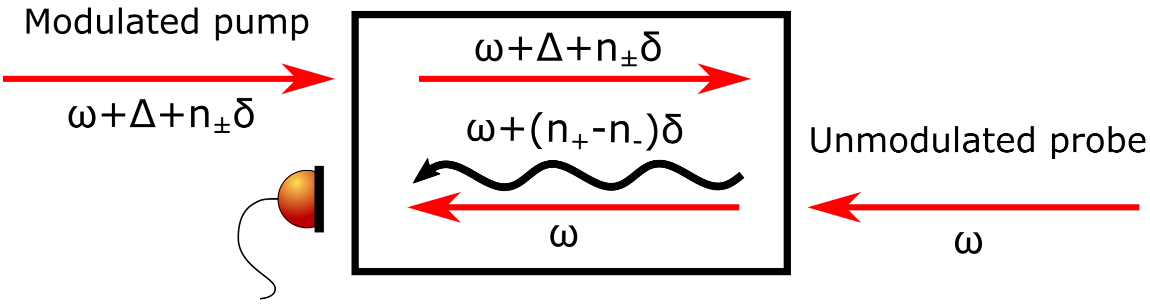

Figure 1.8: Interaction of two sidebands of the pump with the probe inside the medium. The reemitted field is at a frequency $\omega + (n_+ - n_-)\delta$ and $\omega + (n_- - n_+)\delta$.

The reemitted wave has maximum intensity when the one photon and three-photon transition to the excited state are resonant. These resonant conditions $\omega_0 = \omega + \Delta + n_+\delta - k_p v$ and $\omega_0 = \omega + \Delta + n_+\delta - k_p v - (\omega + \Delta + n_-\delta - k_p v) + \omega + k_s v$ give the maximum intensity for

$$\omega = \omega_0 - \Delta - n_+\delta - \frac{k_p}{k_p + k_s}(\Delta + n_-\delta) \tag{1.31}$$

and for the velocity group $(k_p + k_s)v = \Delta + n_-\delta$. In the case were $k = k_s = k_p$, these resonance conditions become $\omega = \omega_0 - \Delta/2 - (n_+ - n_-/2)\delta$ and $kv = \Delta/2 + n_-\delta/2$ [50].

In process presented in Fig 1.9 we present in the first case the $n_+\delta$ sideband as the absorbed one and the $n_-\delta$ for the stimulated emission. We can also look at the symmetrical process by changing $n_+\delta$ in $n_-\delta$ as shown in the second case (see Fig 1.9).

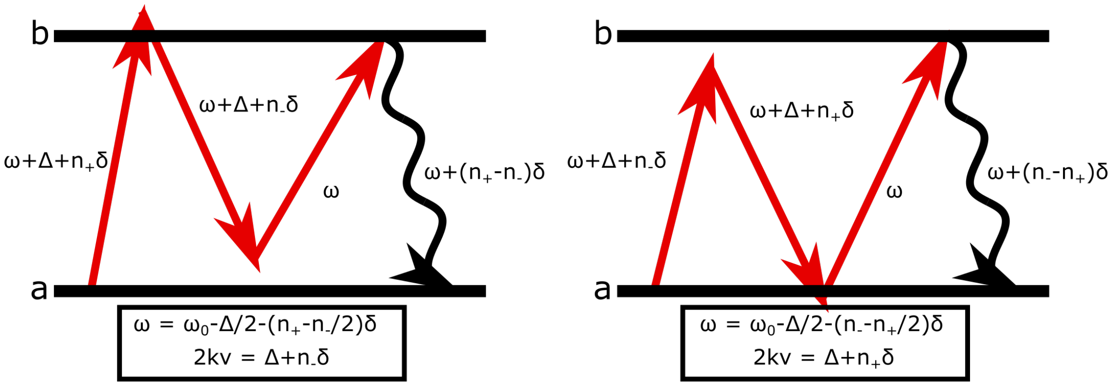

Figure 1.9: Four-wave mixing process. The two sidebands can interact with two different processes depending on which sideband first interacts with the atom. Each process is resonant for a different class of speed and frequency.

For the sake of simplicity we will consider in the following that $k = k_s = k_p$.

The resulting lineshape is the sum of the lineshapes of each process repeated for each sideband in the pump. As stated previously, each resulting lineshape can be calculated using the density matrix (eq 1.20 and 1.26). We now need a third-order development of the density matrix, as it is required for the FWM calculus of the sidebands and the probe.

To get an expression of the resulting polarization with those incident fields, one can obtain the expression of the density matrix component ρ_{ab} by perturbation expansion the fields and making the rotating wave approximation.

We start from equations 1.16 to 1.19. Those equations couple the populations to the coherences which make it difficult to find an analytical solution for non trivial electric fields (other than monochromatic plane waves). To decouple these equations, we can make the hypothesis that the electric fields have small intensities, so are only a perturbation of the TLS. This effectively means making the hypothesis that $p|E| \ll \hbar\gamma_{a,b,ab}$, with E the total electric field i.e. the low saturation intensity approximation. The perturbative calculation is carried out using the decomposition of the total electric field as a sum of plane waves, each order of approximation allowing to account for one more term in the sum.

$$\partial\rho_{aa} = \lambda_a - \gamma_a\rho_{aa} - i(\frac{pE(z,t)}{\hbar}(\rho_{ab} - \rho_{ba})), \tag{1.32}$$

$$\partial\rho_{bb} = \lambda_b - \gamma_b\rho_{bb} + i(\frac{pE(z,t)}{\hbar}(\rho_{ab} - \rho_{ba})), \tag{1.33}$$

$$\partial\rho_{ab} = \rho_{ab}(i\omega_0 - \gamma_{ab}) - i(\frac{pE(z,t)}{\hbar}(\rho_{aa} - \rho_{bb})), \tag{1.34}$$

$$\rho_{ba} = \rho_{ab}^*, \tag{1.35}$$

On the zero order of perturbation i.e in the absence of electric field, the TLS is at equilibrium. We note n_α the equilibrium population of level α and $n = n_b - n_a$, we have

$$\lambda_a = \gamma_a n_a - \gamma_{ab} n_b, \tag{1.36}$$

$$\lambda_b = \gamma_b n_b, \tag{1.37}$$

$$\rho_{ab}^{(0)} = \rho_{ba}^{(0)*} = 0. \tag{1.38}$$

The Bloch equations for the next order calculation can then be written as

$$\partial\rho_{aa} = \gamma_a(n_a - \rho_{aa}) + \gamma_{ab}\rho_{bb} - i(\frac{p}{\hbar}(\rho_{ab} - \rho_{ba}))\sum_\mu E_\mu exp(i(\omega_\mu t - k_\mu r + \phi_\mu)), \tag{1.39}$$

$$\partial\rho_{bb} = \gamma_b(n_b - \rho_{bb}) + i(\frac{p}{\hbar}(\rho_{ab} - \rho_{ba}))\sum_\mu E_\mu exp(i(\omega_\mu t - k_\mu r + \phi_\mu)), \tag{1.40}$$

$$\partial\rho_{ab} = \rho_{ab}(i\omega_0 - \gamma_{ab}) - i(\frac{p}{\hbar}(\rho_{aa} - \rho_{bb}))\sum_\mu E_\mu exp(i(\omega_\mu t - k_\mu r + \phi_\mu)), \tag{1.41}$$

with E_μ the coefficients of the plane wave decomposition of the electric field.

One can see that the population are zero for every odd order of perturbation, and coherences are zero for even orders of perturbation. For example in equation 1.40, to get order 1 of perturbation, ρ_{bb} is taken at order 1 but $\rho_{ab} - \rho_{ba}$ is taken at order 0 for the product $(\rho_{ab} - \rho_{ba})E$ to be order 1. As $\rho_{ab}^{(0)} = \rho_{ba}^{(0)} = 0$ and $(n_b - \rho_{bb}^{(0)})$, $\rho_{bb}^{(1)} = 0$ too.

In first order, solving eq 1.41 and neglecting the rapidly oscillating term in the exponential gives

$$\rho_{ab}^{(1)} = i(\frac{p}{\hbar}n)) \sum_\mu E_\mu \frac{exp(-i(\omega_\mu t - k_\mu r + \phi_\mu))}{\gamma_{ab} + i(\omega_\mu - \omega_0 - k_\mu v)}, \tag{1.42}$$

We can use this expression of $\rho_{ab}^{(1)}$ in the second order development of ρ_{bb} and ρ_{aa}. We can then reiterate the development for the third order of the coherences (detail in Annex C). We finally obtain

$$\begin{aligned}\rho_{ab}^{(3)} = -i\frac{n}{8} \sum_{\mu,\nu,\lambda=0,+,-} \frac{e^{i(\Phi_\mu - \Phi_\nu + \Phi_\lambda)}}{L_{ab}(\mu - \nu + \lambda - \omega_0)} & \left\{ \beta_\mu \beta_\nu \beta_\lambda \left[\frac{1}{L_a(\mu - \nu)} + \frac{1}{L_b(\mu - \nu)} \right] \right. \\ & \left. \times \left[\frac{1}{L_{ab}(\mu)} + \frac{1}{L_{ab}^*(\nu)} \right] \right\}\end{aligned} \tag{1.43}$$

with

$$\Phi_X = \omega_X t - k_X z + \varphi_X, \tag{1.44}$$

$$L_{ab}(\mu - \nu + \lambda - \omega_0) = \gamma_{ab} + i[\omega_\mu - \omega_\nu + \omega_\lambda - \omega_0 - (k_\mu - k_\nu + k_\lambda)v], \tag{1.45}$$

$$L_\alpha(\mu - \nu) = \gamma_\alpha + i[\omega_\mu - \omega_\nu - (k_\mu - k_\nu)v], \tag{1.46}$$

$$\beta_X = p\mathcal{E}_X/\hbar \tag{1.47}$$

This gives us a general expression for the third-order density matrix describing the FWM process involved in MTS. Lets consider the first process in figure 1.9, and look only at the induced polarization term emitted at frequency $\omega + (n_+ - n_-)\delta$.

In this case, eq 1.43 becomes

$$\begin{aligned}\rho_{ab}^{(3)}(v) = -i\frac{n}{8}\beta_+\beta_-\beta_0 \frac{e^{i(\omega + (n_+ - n_-)\delta)t + kz + \varphi + \varphi_0}}{\gamma_{ab} + i(\omega + (n_+ - n_-)\delta - \omega_0 + kv)} \sum_{\alpha=a,b} & \left\{ \frac{1}{\gamma_\alpha + i(n_+ - n_-)\delta} \right. \\ \times \left[\frac{1}{\gamma_{ab} + i(\omega + \Delta + n_+\delta - \omega_0 - kv)} + \frac{1}{\gamma_{ab} - i(\omega + \Delta + n_-\delta - \omega_0 - kv)} \right] & \\ \left. + \frac{1}{\gamma_\alpha + i(2kv - \Delta - n_-\delta)} \left[\frac{1}{\gamma_{ab} + i(\omega - \omega_0 + kv)} + \frac{1}{\gamma_{ab} - i(\omega + \Delta + n_-\delta - \omega_0 - kv)} \right] \right\}. &\end{aligned} \tag{1.48}$$

The density matrix element in 1.48 is velocity dependent. We define the velocity average by the integration of the Doppler profile, that we assumed to be a Maxwellian distribution of rms thermal velocity u.

$$\langle \rho \rangle = \int_{-\infty}^{+\infty} \frac{dv}{u\sqrt{\pi}} \mathrm{e}^{(-v^2/u^2)} \rho(v). \tag{1.49}$$

For velocity integration we assume that $\Delta, \delta \ll ku$. It corresponds to the situation where all optical frequencies are well within the Doppler broadening. At the first order in γ/ku, we obtain

$$\begin{aligned} \langle \rho_{ab}^{(3)}(\omega + (n_+ - n_-)\delta) \rangle = & -\frac{i}{8} n \beta_+ \beta_- \beta_0 \frac{\sqrt{\pi}}{ku} \\ & \times \frac{\mathrm{e}^{i[(\omega + (n_+ - n_-)\delta)t + kz + \varphi + \varphi_0]}}{\gamma_{ab} + i(\omega + \Delta/2 - \omega_0 + (n_+ - n_-/2)\delta)} \sum_{\alpha = a,b} \frac{F(\Delta + n_-\delta)}{\gamma_\alpha + i(n_+ - n_-)\delta}, \end{aligned} \tag{1.50}$$

with

$$F(x) = \exp\left[-(x/2ku)^2\right]. \tag{1.51}$$

With equation 1.26 and equation 1.20, we can then write the field reemitted by two pump sidebands and the probe by the first process of figure 1.9, noted $\mathcal{E}^r(+)$,

$$\mathcal{E}^r(+) = \frac{-kL}{8\epsilon_0} n \beta_+ \beta_- \beta_0 p \frac{\sqrt{\pi}}{ku} \frac{F(\Delta + n_-\delta/2)}{\gamma_{ab} + i(\omega + \Delta/2 - \omega_0 + (n_+ - n_-/2)\delta)} \sum_{j=\alpha} \frac{1}{\gamma_\alpha + i(n_+ - n_-)\delta} \tag{1.52}$$

The second process re-emits a similar field, noted $\mathcal{E}^r(-)$, obtained by changing n_+ in n_- and n_- in n_+. This gives the lineshape of the reemitted FWM field for two sidebands of the pump.

Now that we have an expression of the contribution of two sidebands of the pump, we can look specifically in the frequency region of interest for MTS (near δ) and sum over the contribution of every sidebands of the pump in this frequency region.

As we can see on the Fig 1.9, 2 pump sidebands of order n_+ and n_- will interact with the probe via FWM process resulting in a component at $(n_+ - n_-)\delta$. Then results in a reemitted field in the direction of the probe. It can be written by reordering each term with $p = n_+ - n_-$:

This resulting field will beat with the probe field to yield a signal at frequency $p\delta$. Looking at the case $p = 1$, one can write the lineshape of the reemited field S as the sum of lineshapes of reemited fields for FWM processes between pump sidebands of order n and $n - 1$:

$$S(\delta) = \sum_{n \in \mathbb{K}} J_n(M) J_{n-1}(M) S(n, n-1) \tag{1.53}$$

The lineshape $S(n, n+1)$ is the sum of $\mathcal{E}^r(-)$ process as in eq 1.52 summed with the $\mathcal{E}^r(-)$ process, the resulting expression for the normalised lineshape of the MTS signal is

$$S(\delta) = \sum_{n,\alpha} J_n(M) J_{n-1}(M) \frac{C_\alpha}{\gamma_\alpha + i\delta} \left[\frac{1}{\gamma_{ab} + i[\nu + (n+1)\delta/2]} + \frac{1}{\gamma_{ab} - i[\nu + (n-2)\delta/2]} \right], \tag{1.54}$$

where $\nu = \omega - \omega_0 + \Delta/2$, γ is the optical dipole relaxation rate, γ_α is the relaxation rate of level α and C_α is a coefficient depending on incident beam polarization (see also [49](eq 6)).

1.2.4 Numerical simulation

In the following, two simulations of the MTS signal have been performed. Figures 1.10, 1.11, 1.12, and 1.13 correspond to simulations with a selection of the velocity classes considered with the hypothesis of a small modulation factor $M \ll 1$. It therefore exhibits a quadruplet as only the sidebands $\{-1; 0\}$ and $\{0; 1\}$ will be reemitting a field at a frequency δ. For figure 1.14 the simulation is carried with the analytical velocity integration in formula 1.54 and for a varying modulation factor.

Influence of the modulation frequency on the lineshape

A study of the MTS signal lineshape under different modulation frequency δ is shown in Fig 1.10. The integration on velocities is done numerically. The limits on the velocity integration is represented on the figure. We chose velocity classes around ω_0 and the red vertical lines represent the limit of the numerical velocity integration kv_{lim} in eq 1.48 and 1.49.

Figure 1.10 shows the error signal in the low modulation limit ($M \ll 1$). In this limit only the J_0 and J_1 terms are significant. The lineshape S (in 1.54) only has 4 significant components, each separated by $\delta/2$. For $\gamma_{ab} \ll \delta$, the 4 components are distinguishable. For $\gamma_{ab} \gg \delta$ the signal is merged in one "dispersion-like" lineshape for every demodulation phase of the MTS signal as seen on figure 1.10d. As can be seen on the figure, the amplitude of the dispersion signal is reduced when γ_{ab} is increased. An optimal size of this amplitude seems to be reached when $\delta = \gamma_{ab}$ i.e. when the dispersion shape are merged.

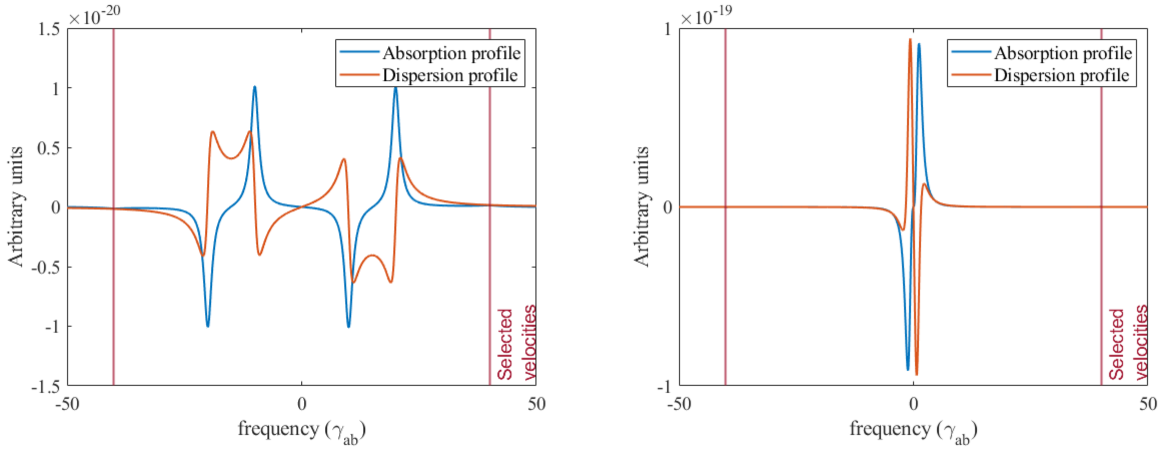

(a) $\delta = 20\gamma_{ab}$, $M = 0.05$ (b) $\delta = \gamma_{ab}$, $M = 0.05$

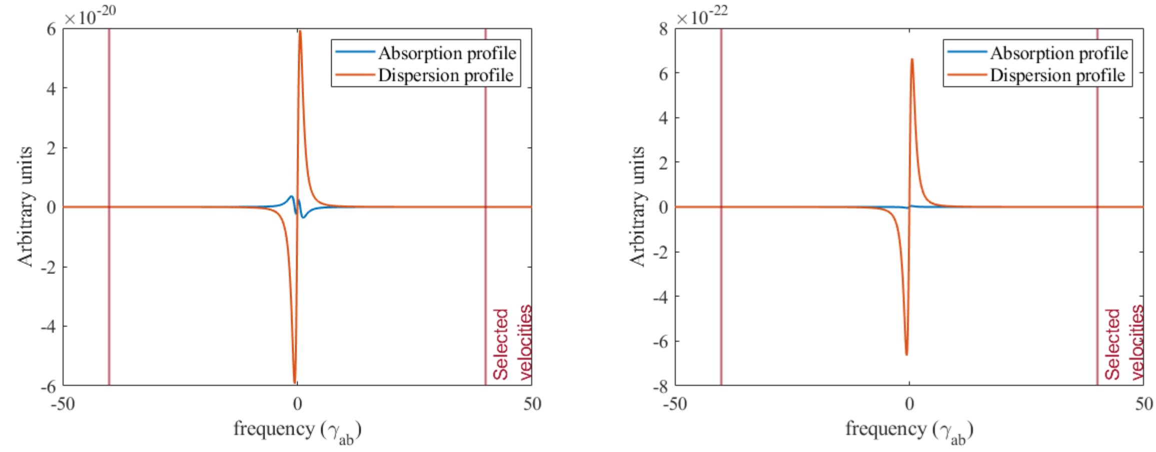

(c) $\delta = 0.1\gamma_{ab}$, $M = 0.05$ (d) $\delta = 0.001\gamma_{ab}$, $M = 0.05$

Figure 1.10: Lineshapes of MTS signal for different modulation frequencies. Velocity integration is performed numerically from eq 1.48. Horizontal axis is in units of the effective linewidth of the molecule γ_{ab}. Vertical axis is in arbitrary units. The relative amplitude can be compared but they depends on the γ_a lifetime chosen here at $\gamma_a = 0.2\gamma_{ab}$. Only the modulation frequency is changed from 20, 1, 0.1, 0.001 γ_{ab} for figures a, b, c and d respectively.

Influence of the selected velocities on the lineshape

A study of the selected velocities impact has been conducted. In the hypothesis of a cold sample, the signal observed with MTS is changed as the velocity distribution is changed. Fig 1.11 shows the impact of velocity in the $\gamma_{ab} \ll \delta$ limit. Fig 1.12 and Fig 1.13 shows the influence of velocity class on the $\gamma_{ab} \gg \delta$ limit.

We find that only in the case $\delta \gg \gamma_{ab}$ (1.11) the MTS signal is significantly changed, as the contributing velocities classes are spaced by $\delta/2$ for the $\mathcal{E}^r(+)$ and $\mathcal{E}^r(-)$ components of the signal as one can see in Fig 1.9. One can also note that the $\mathcal{E}^r(\pm)$ components are resonant for $\omega = \omega_{ab} - (n_\pm - n_\mp/2)\delta$ as predicted in Fig 1.9.

In Fig 1.11 we can see that each of the 4 features of the lineshape 1.11a is related to the optical response of a single velocity class centred at $kv = \frac{-\delta}{2}$ (1.11b), $kv = \frac{\delta}{2}$ (1.11c) and $kv = 0$ (1.11d). This indicates that the lineshape is not induced by a single coherent process and that each feature is actually independent from the others.

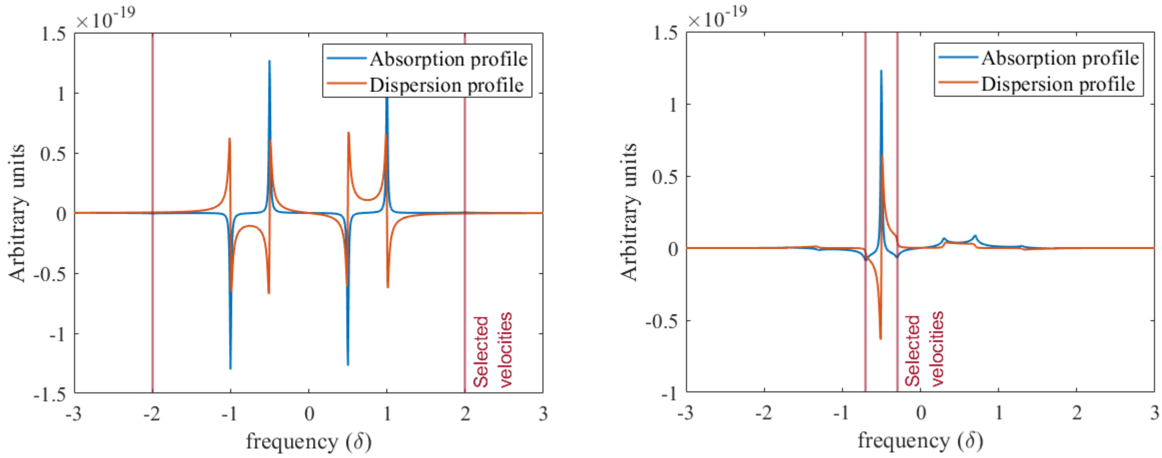

(a) Velocity classes centred around $kv = 0$, $\Delta kv = 4\delta$

(b) Velocity classes centred around $kv = \frac{-\delta}{2}$, $\Delta kv = 0.2\delta$

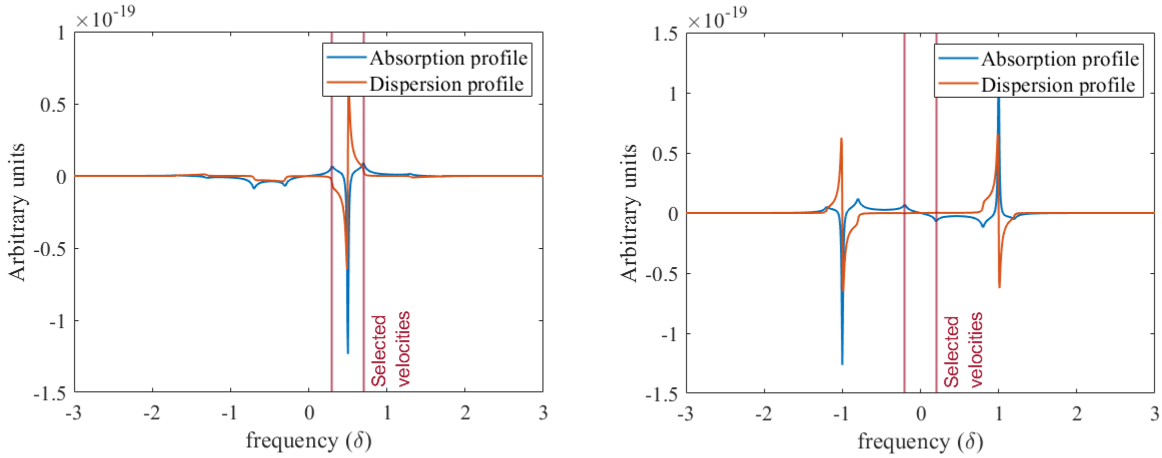

(c) Velocity classes centred around $kv = \frac{\delta}{2}$, $\Delta kv = 0.2\delta$

(d) Velocity classes centred around $kv = 0$, $\Delta kv = \frac{\delta}{2}$

Figure 1.11: Lineshape of the MTS signal for different velocity distributions of molecules in the $\delta \gg \gamma_{ab}$ limit.

For $\delta \ll \gamma_{ab}$ (Fig 1.12 and 1.13) the homogeneous broadening dominates over any velocity selectivity of MTS. As it could have been expected, the signal amplitude is constant for $kv \gg \gamma_{ab}$ and reduces when $kv \ll \gamma_{ab}$. Physically this corresponds to having less atoms participating in the FWM process. In Fig 1.13 it is however possible to see an asymmetry in the error signal for asymmetric velocity classes .

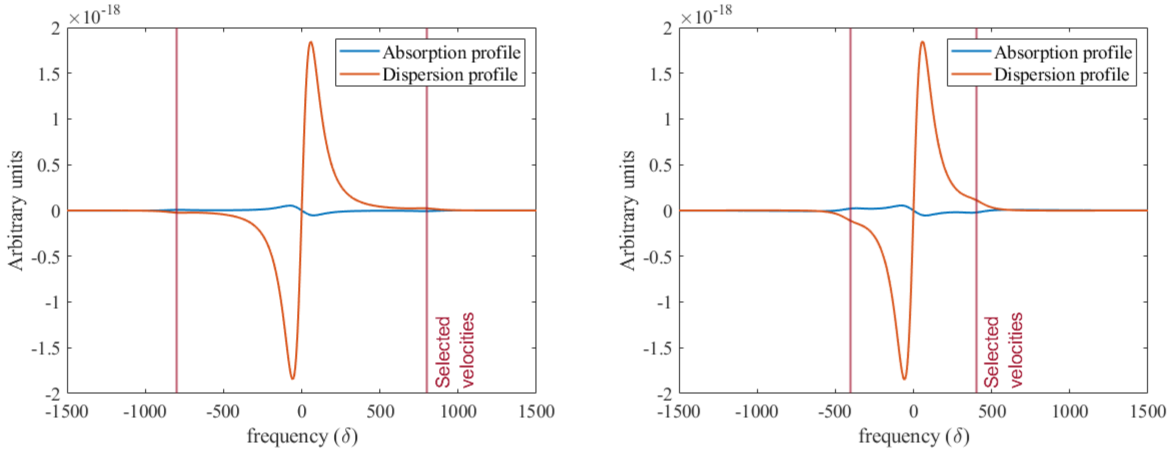

(a) Velocity classes centred around $kv = 0$, $\Delta kv = 800\delta$

(b) Velocity classes centred around $kv = 0$, $\Delta kv = 400\delta$

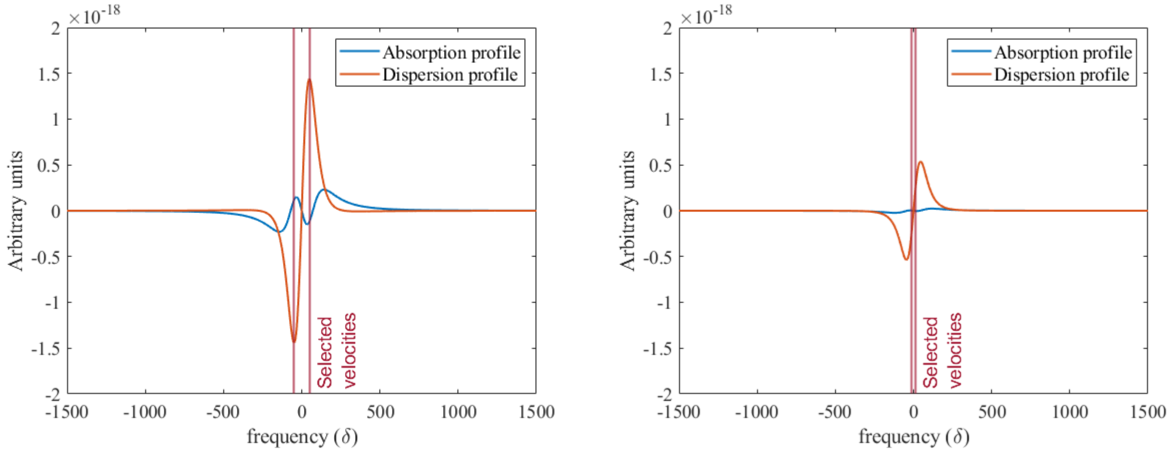

(c) Velocity classes centred around $kv = 0$, $\Delta kv = 50\delta$

(d) Velocity classes centred around $kv = 0$, $\Delta kv = 10\delta$

Figure 1.12: Lineshape of the MTS signal for different velocity distributions of molecules for $\delta = \gamma_{ab}/100$.

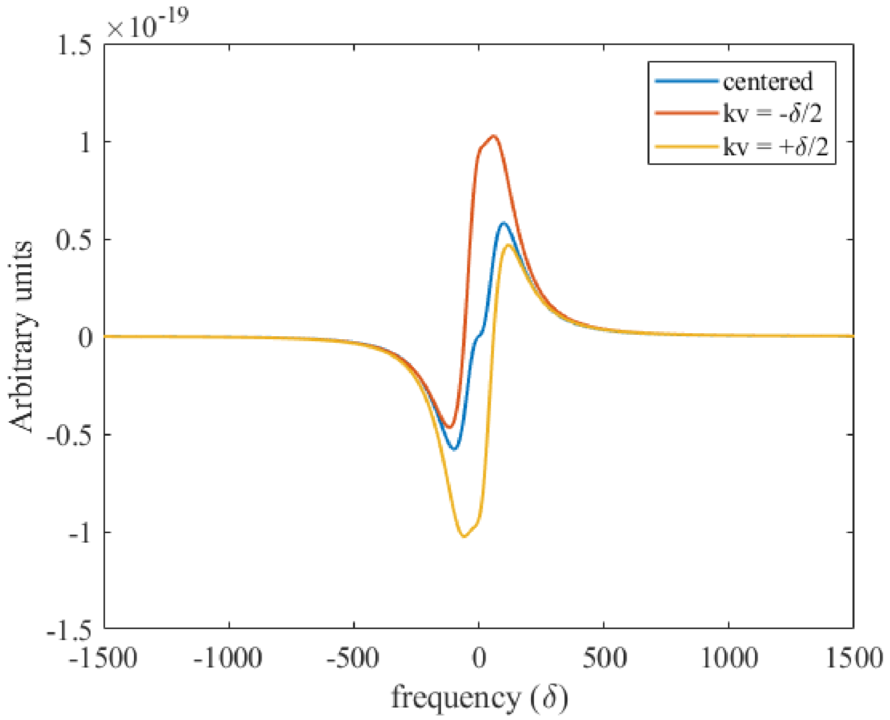

Figure 1.13: Lineshape of the MTS signal for different velocity distributions of molecules for $\delta = \gamma_{ab}/100$. Velocity classes centred around $kv = 0$, $kv = \frac{-\delta}{2}$, and $kv = \frac{\delta}{2}$ with $\Delta kv = 0.2\delta$. It is possible to see an asymmetry of the MTS signal if the velocities are centred on the resonance of $\mathcal{E}^r(+)$ or $\mathcal{E}^r(-)$. Note that the vertical scale is zoomed compared to Fig 1.12 while the normalisation is the same (ie the signals have much smaller amplitudes)

Optimisation of the MTS signal for generation of an error signal

In this PhD work, we aim at using the MTS signal as an error signal for laser frequency stabilisation. Therefore we need a good signal to noise ratio (SNR) and we need the error signal to have a steep slope to have the best possible frequency sensitivity.

We have seen previously that the MTS signal is usable as an error signal in the $\gamma_{ab} \gg \delta$ region (see Fig 1.10). The study of the lineshape will therefore be conducted in this regime.

Furthermore, we can also change the modulation factor which in turns changes the lineshape. By increasing the modulation factor M, more terms come into play in the summation of Eq. 1.53. This is due to the higher order Bessels functions that become non-negligible.

In Fig 1.14, we trace the amplitude and slope of the error signal as a function of experimentally tunable parameters: the modulation frequency δ and modulation factor M. Similar results were obtained in [56]. The numerical calculation for the lineshape is done using Eq. 1.54 where the velocity integration was done analytically.

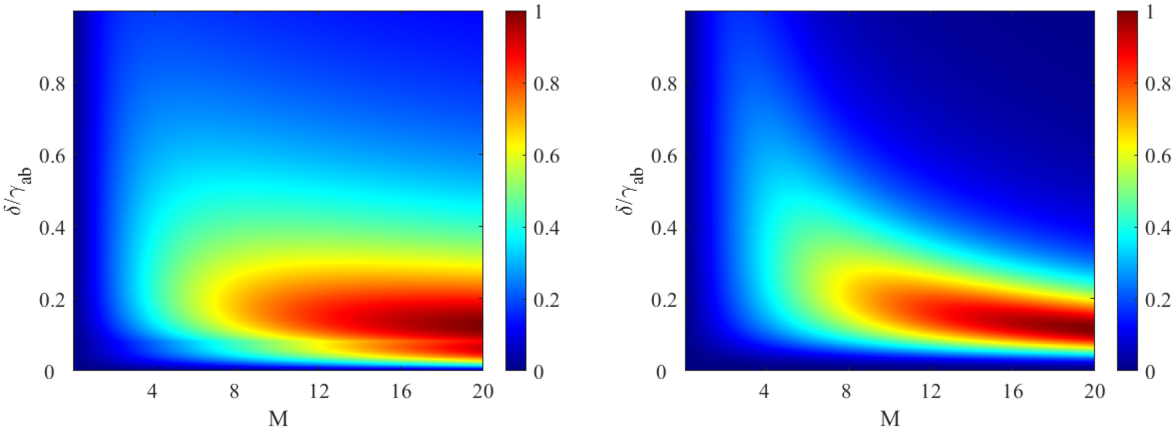

(a) Amplitude of the MTS signal.

(b) Slope of the MTS signal.

Figure 1.14: MTS signal amplitudes (a) and slope (b) for different parameters. The data represented correspond to the maximum of amplitude and slope for every possible demodulation phase and are normalized for the maximum amplitude or slope.

While the intuitive understanding of the lineshape in previous sections was carried using a low modulation amplitude, we see in Fig 1.14a that there is a lot to gain in using a large modulation amplitude M. From Fig 1.14, it seems that a rule of thumb for the optimal parameters is $M\delta = 2\gamma_{ab}$. This formula is actually quite intuitive because $M\delta$ corresponds roughly to the spectral extension of the Fourier transform of the modulated signal.

1.2.5 Residual Amplitude Modulation

When using a phase modulation technique for spectroscopy and laser stabilisation, residual amplitude modulation (RAM) is often observed in optical signals. Indeed, optical components don't have a constant power transmission for all wavelengths which result in amplitude modulation of the light at the same modulation frequency than the modulation's frequency. This can be detrimental for stabilisation and spectroscopy, as it can result in a demodulated signal with a shape different from the one predicted by theoretical models.

In addition, as shown in the previous section, a large amplitude of the modulation frequency would be interesting to optimise the SNR. This requires to drive strongly the modulator which generally results in an increased RAM.

RAM can be studied with a numerical simulation by adding a small modulation in amplitude. For the sake of simplicity it will be chosen sinusoidal. In the Fourier frequency domain, a sinusoidal modulation in amplitude at a frequency f_{RAM} is represented as two in-phase sidebands spaces by $\pm f_{RAM}$

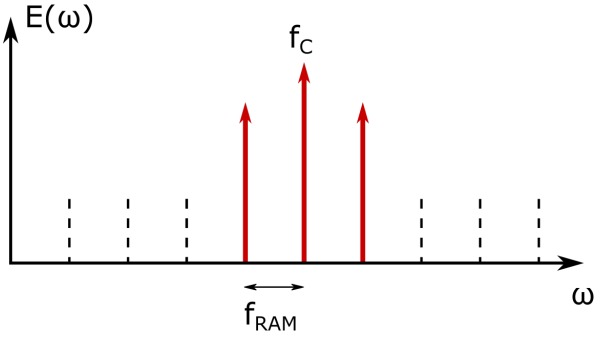

Figure 1.15: natural broadening.

With a sinusoidal modulation we can simply add a small perturbation to the sidebands $(J_1 \rightarrow J_1 + \delta_{RAM},\ J_{-1} \rightarrow J_{-1} + \delta_{RAM})$. Note that the Bessels functions are in opposition phase while the amplitude perturbation has the same phase for both sidebands.

This results in a asymmetry in the MTS error signal after demodulation as seen in Fig 1.16. This asymmetry will reduce the frequency stability. Indeed power fluctuations of the pump beam results in a shift of the locking frequency points. It thus couples power fluctuations to frequency fluctuations in a laser stabilisation scheme.

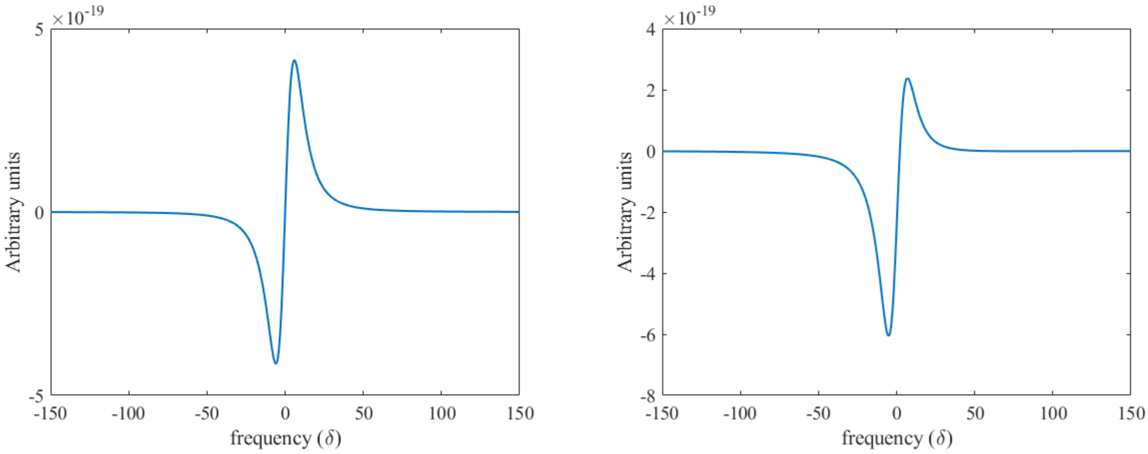

(a) $\delta = 0.1\gamma_{ab}$, $M = 0.05$, NO RAM. (b) $\delta = 0.1\gamma_{ab}$, $M = 0.05$, 1% RAM

Figure 1.16: Lineshapes of the MTS signal in the absence and presence of RAM. The RAM is expressed as the ratio between the modulation amplitude (AM) part of the field and the phase modulation (PM) of the field.

1.3 Fibre parameters influence on sub Doppler spectroscopy

In the previous section we studied theoretically the different MTS signals one can expect given a set of the modulation parameters and TLS's transition. In this section we focus on the influence of the experimental conditions on the MTS signal. In particular we concentrate on the specificity of hollow core fiber spectroscopy.

1.3.1 Natural broadening

Spectral transition lines are never strictly monochromatic. While many experimental conditions can be responsible for the spectral broadening, the transition is in-itself a non purely monochromatic process. This is called the *natural broadening.*

We consider a TLS defined by two states a and b. The states a and b are defined as *eigenstates* of the Hamiltonian operator describing the time evolution of the TLS in the *absence* of electromagnetic field. This means that one can write the TLS Hamiltonian as a diagonal matrix in a eigenvector basis consisting of states a and b. If a TLS is prepared in one of these states, it stays indefinitely in one of these states.

However we are looking at transition lines, which require the coupling of these states by an electromagnetic field. This is described by adding an interaction Hamiltonian with non diagonal components [57] in the basis a,b. This results in a total Hamiltonian which is no longer diagonal in this basis, meaning that the states a and b are no longer eigenstates of the system when the TLS is coupled with a electromagnetic field. Therefore the system is no longer stable in those states, they have a finite lifetime.

A simple model to describe the TLS coupled to the field is the damped oscillator [58] which shows the Lorentzian response characterised by its width often noted γ.

In our case, acetylene molecules have a weak coupling to the electromagnetic field for the P14 transition [42] meaning that the system is close to an isolated TLS [59]. This means that the excited state is long lived. In the previously described model, it corresponding to a weakly damped oscillator in the previously described model [58]. This result in a very narrow Lorentzian profile, experimentally measured at a few Hz [25].

1.3.2 Pressure broadening and shift

The natural linewidth of the transition is in general not directly observable, as it is broaden by various mechanisms.

The first homogenous broadening is pressure broadening. As the pressure of the gas is increased, more collisions will occur causing a dephasing of the vibrational states that lead to a loss of coherence. This shorter coherence time implies that the linewidth of the transition will be broadened. The pressure broadening for acetylene has been measured in [30] at $\Gamma_{pressure} = 225\text{kHz/Pa} \times \text{P}$ for pressure ranging from P = 0.6 Pa to 10 Pa which are the typical pressure range we will be using in this work.

As the pressure broadening is due to collisions in the gas, it is proportional to the total pressure of the gas.

Furthermore, as two molecules get close to each other, their interaction shifts the energy levels involved in the transition. If the emission happens during the collision while the energy level are shifted, the transition frequency observed is shifted. Collisions are not instantaneous events, and to understand the pressure shift, it is better to consider the mean distance between two molecules, which gives the mean shift in frequency between the energy levels. The pressure shift for the P14 transition has been characterised [60]. In this work we have not measured the absolute frequency of the laser. We were indeed only interested in the stability of the laser.

1.3.3 Transit time broadening

Transit time broadening is due to the fact that the molecules are interacting with the probe and pump beam for a limited amount of time. This comes from the finite size of the beam, and the transverse thermal velocity of the molecules. Molecules will spend a limited time interacting with the beam, reducing the effective coherence time, which translates to a broadening of the transition.

If we approximate the beam to an homogeneous beam of radius w_0, the time spent by the molecule in the beam can be approximated by the beam size divided by the average thermal velocity. The transit time broadening is the inverse of this interaction time. As the beam is not a square homogeneous beam, proportionality factor should be modified for increased accuracy [30] , [61]. In this work we will be using the following expression for transit time broadening [30]:

$$\Gamma_{transit} = \frac{0.19}{w_0}\sqrt{\frac{2k_BT}{M_{C_2H_2}}}. \tag{1.55}$$

The factor 0.19 accounts for the gaussian enveloppe of the beam.

1.3.4 Multimode inhomogeneous broadening

The light propagation inside a fibre can be described as a sum of guided modes. These modes are characterised by different propagating constants. For a given free space frequency injected in the fibre, if more than one transverse mode is propagating in the fibre, more than one class of speeds will be resonant with the injected beam.

If we look at eq 1.31, we can see that a shift can be created in the resonance frequency of the MTS if the propagating constant of the pump k_p and the probe k_s are changed.

If we compare the case (1) $k = k_p = k_s$ to the case (2) $k_p \neq k_s$ with $n_+ - n_- = \pm 1$, we find a shift $\Delta\omega_{21} = \delta(\frac{k_p}{k_p+k_s} - \frac{1}{2})$ or $\Delta\omega_{21} = \delta(\frac{n_p}{n_p+n_s} - \frac{1}{2})$ with n_p and n_s the effective propagation indices of the pump and the probe.

Using typical indices values for PBG fibers [62] for the two most transmitted modes on a 7 cell Kagome fiber, modulation amplitudes in the order of magnitudes used in this work ($\delta = 10$ MHz) with a probe either in the fundamental mode LP$_{01}$ or in the LP$_{11}$ mode, we calculate a frequency shift of the resonance frequency of the MTS signal $\Delta\omega_{21} =\sim 300$ Hz. This shift is orders of magnitudes below the frequency instability measured with the fibers in this work. It can therefore not explain the measured shift.

However, experimental measurement of SAS and EIT signals using different modes for pump and probe in a fiber have been conducted by the XLim. Experimentally, shifts of ~ 10 MHz were observed in the work of Thomas Billotte's thesis [38] when going from the propagation of the pump and probe in the same mode (LP$_{01}$-LP$_{01}$ or LP$_{11}$-LP$_{11}$) to the propagation in two different modes (LP$_{01}$-LP$_{11}$) in SAS measurements. We don't explain fully the magnitude of these shift observed in SAS and EIT, and it is possible that such phenomenon would also affect MTS and thus our spectroscopy of the fibers.

This can be an issue particularly when the mode content of a fibre can very due to environmental condition. It has also been shown in [30] that multimode fibre lead to instability in the spectroscopy coupled to environmental noise (eg. thermal fluctuation in [30]).

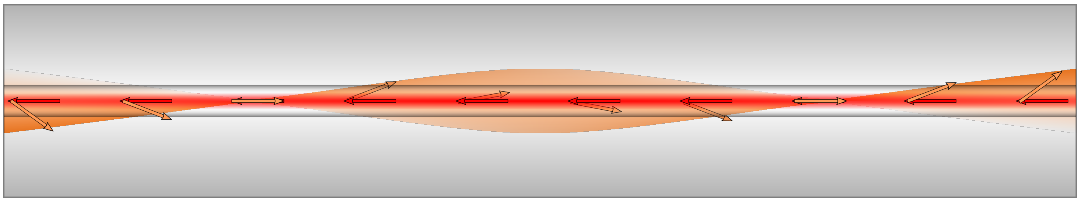

Figure 1.17: Representation of the propagation of different modes in the fiber. Each mode as a different propagation constant (wavevector) which leads to a broadening.

1.4 Tools for stability measurements

In this section, we aim at quantifying the different external parameters that could cause a reduction in frequency stability of a laser system locked on acetylene trapped in a hollow-core fibre. We first define the tools needed for measuring and representing the stability of a frequency signal. We then measure the variation in frequency caused by a controlled variation of an external parameter. This measure of the spectroscopy's sensitivity aims at explaining the mechanism limiting the fibre performance.

In this section, we cover the tools used to quantify the frequency stability of the laser system studied. We give the mathematical framework for the reading of a figure of merit, the Allan deviation. We also detail the experimental setup used as a frequency reference for the measurement of Allan deviation, and provide information on the acquisition tools developed for long term recording of laser's frequency.

1.4.1 Allan deviation

The output of any real oscillator like a laser deviates from the ideal single sin wave. A model widely accepted and used to represent the noise in any real oscillator is [63]

$$V(t) = (V_0 + \epsilon(t)) \sin[2\pi\nu_0 t + \phi(t)], \tag{1.56}$$

where ϵ and ϕ are random processes, named the *amplitude noise* and *phase noise* respectively. V_0 and ν_0 are the nominal signal amplitudes and frequency respectively, and are considered constant. For this work, we will neglect the contribution of ϵ and focus on the phase noise. The *stability* of the signal will be characterized by a figure of merit (i.e a variance, a power spectral density...) which will qualify the contribution of ϕ to the $V(t)$ signal's fluctuation. The lower the contribution the better the stability.

The measurement of frequency stabilities can be seen in two different ways, either by the spectral representation of the signal, or in the time domain by using variances. The spectral density of a random signal is defined as the Fourier transform of the autocorrelation function of one of its parameters. Looking at eq 1.56, 4 different spectra might be of interest. The spectrum of the entire time serie $V(t)$, the spectral density of $\epsilon(t)$, the spectral density of $\phi(t)$ noted $S_\phi(\omega)$ and the spectral density of $\dot{\phi(t)}$ noted $S_{\dot{\phi(t)}}(\omega)$. For very stable oscillators, only $S_\phi(\omega)$ and $S_{\dot{\phi(t)}}(\omega)$ are of interest [64].

It is however preferred for some frequency standard users to use variances as it gives an intuitive reading of the expected frequency shift that a source will undergo during a given period of time [63]. For technical reasons, the signal represented as spectral density is preferred for short term measurements as it is acquired using Fast Fourier Transform (FFT) analysers, while time-domain techniques for measuring variances is preferred for longer timescales, with a limit at around 1 Hz [65]. The variance can be defined as the mean-square value of a certain parameter of the signal. We will see in this section that one can also construct variances using the spectral densities. Variances are most used on the *fractional frequency instability* [64] defined below.

We define an instantaneous frequency

$$\nu(t) = \nu_0 + \frac{1}{2\pi}\frac{d\phi(t)}{dt}, \tag{1.57}$$

and the frequency noise as

$$\Delta\nu(t) = \nu(t) - \nu_0 = \frac{1}{2\pi}\frac{d\phi(t)}{dt}. \tag{1.58}$$

A useful quantity to characterise the frequency stability of an oscillator regardless of its nominal frequency is the normalised frequency fluctuation, also called $fractional\ frequency\ instability$

$$y(t) = \frac{\Delta\nu(t)}{\nu_0}. \tag{1.59}$$

There are two ways to characterise oscillators, spectral densities using the Fourier domain representation of the signal, and variances of the averaged frequency fluctuations in time domain. It is possible to use the Fourier transform to go from one representation to the other [64], [63].

In practice the signal is sampled with a frequency counter, that gives the average frequency $\bar{y_i}$, which is the average value of $y(t)$ over the time τ starting at time t_n. We first consider a measurement with no dead time, meaning that $t_n = (n-1)\tau$.

A variance widely used for the characterisation of oscillators is the Allan variance defined as

$$\sigma_y^2(\tau) = \frac{1}{2}\Big\langle (\bar{y_2} - \bar{y_1})^2 \Big\rangle, \tag{1.60}$$

with $\langle \dots \rangle$ the expectation value. As it is impossible to measure directly the expectation value of a random variable, we use an estimator of the Allan variance which is

$$\sigma_y^2(\tau, m) = \frac{1}{2(m-1)}\sum_{i=1}^{m-1}(y_{\bar{i}+1} - \bar{y_i})^2. \tag{1.61}$$

It should be noted that the Allan variance can be calculated from the power spectral density of the signal (see Section 3.3 [66]). We derive below their relation.

$$\sigma_y^2(\tau) = \frac{1}{2}\Big\langle \Big(\frac{1}{\tau}\int_{t_{k+1}}^{t_{k+2}} y(t')dt' - \frac{1}{\tau}\int_{t_k}^{t_{k+1}} y(t')dt'\Big)^2 \Big\rangle, \tag{1.62}$$

because we are taking the expected value of the $\bar{y_i}$, this relation is true for every value of k

$$\sigma_y^2(\tau) = \frac{1}{2}\Big\langle \Big(\frac{1}{\tau}\int_{t}^{t+\tau} y(t')dt' - \frac{1}{\tau}\int_{t-\tau}^{t} y(t')dt'\Big)^2 \Big\rangle. \tag{1.63}$$

Introducing $h_\tau(t)$ as

$$h_\tau(t) = \begin{cases} -\frac{1}{\sqrt{2}\tau} & \text{for} \quad -\tau < t < 0 \\ +\frac{1}{\sqrt{2}\tau} & \text{for} \quad 0 \le t < \tau \\ 0 & \text{for} \quad \text{otherwise} \end{cases} \tag{1.64}$$

one can write the Allan variance as the expectation value of a convolution product

$$\sigma_y^2(\tau) = \left\langle \left(\int_{-\infty}^{+\infty} y(t')h_\tau(t-t')dt' \right)^2 \right\rangle. \tag{1.65}$$

Using the Parseval theorem one can write equation 1.65 in the Fourier domain

$$\sigma_y^2(\tau) = \int_{0}^{+\infty} S_y(f)|H_\tau(f)|^2 df, \tag{1.66}$$

with H_τ the Fourier transform of h_τ and S_y the one sided power spectral density (PSD) of y.

It is then possible to interpret the Allan variance as the power of the signal filtered with a transfer function H_τ with $|H_\tau(f)|^2 = 2\frac{\sin^4(\pi\tau f)}{(\pi\tau f)^2}$. This representation gives quite an intuitive link between the Allan variance and the different type of noises which are characterised by their PSDs.

$$\sigma_y^2(\tau) = 2\int_{0}^{+\infty} S_y(f)\frac{\sin^4(\pi\tau f)}{(\pi\tau f)^2} df, \tag{1.67}$$

The different type of experimental noises that can be observed in an oscillator are commonly modelled with power law function [66] $S_y(f) = h_\alpha f^\alpha$ with $-2 < \alpha < 2$. Table 1.1 presents the different noises typically present in oscillators, as well as the respective slope in the corresponding Allan variance.

$S_y(f)$	Type of noise	$\sigma_y^2(\tau)$
$h_{-2}f^{-2}$	Random walk in frequency	$(2\pi^2 h_{-2}/3)\tau$
$h_{-1}f^{-1}$	Flicker frequency noise	$2h_{-1}\ln 2\tau^0$
$h_0 f^0$	White frequency noise (= random walk in phase)	$h_0/2\tau^{-1}$
$h_1 f^1$	Flicker phase noise	$h_1[1.038 + 3\ln(2\pi f_h\tau)]/(4\pi^2)\tau^{-2}$
$h_2 f^2$	White phase noise	$[3h_2 f_h/(4\pi^2)]\tau^{-2}$

Table 1.1: Different types of noise commonly found in oscillators represented in power spectral density and Allan variances. It is necessary to introduce f_h as a cutoff frequency in the integral 1.67 as it diverges for $\alpha \leq 0$. This is experimentally always verified as all measuring device has a limited bandwidth towards high frequency. The value for the slope of $\sigma_y^2(\tau)$ are presented in the $2\pi f_h\tau \gg 1$ limit.

Thus one can identify the dominating noise type using the Allan variance representation of the signal.

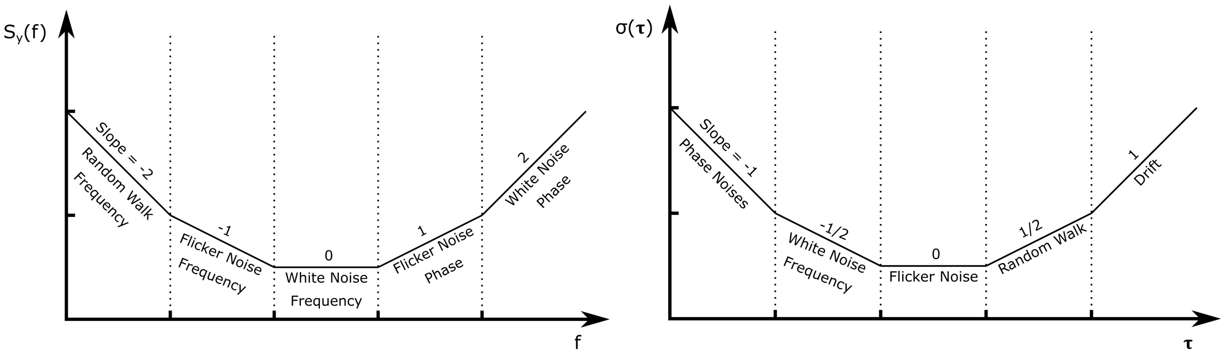

(a) (b)

Figure 1.18: (a) Representation of the common noises found in experimental conditions (b) Corresponding Allan deviation of the common types of noises.

1.4.2 Frequency reference and counter

Frequency comb principle

To determine the stability of a signal, we measure the deviation over time of this signal compared to a reference signal. In the case of laser stability, we need to compare the signal to an optical frequency reference. In the experiment presented here, we used a frequency comb. This is a device that transposes the stability of a microwave reference in the optical domain. The frequency comb we use is a commercial mode-locked femtosecond laser broadened from Menlo Systems. This allows for the generation of light whose spectrum can be described as a serie of so called *comb tooth* regularly spaced. The spacing between the tooth is determined by the repetition rate ω_r of the laser (as a repeated signal can be represented by the Fourier transform of the signal multiplied by a Dirac comb).

Because the carrier frequency of the laser is not necessary commensurate with the envelope pulses repetition rate, each pulse is phase shifted by a quantity $\Delta\Phi$ (see fig 1.19). This result in a frequency shift of $\omega_c = \frac{\Delta\Phi}{\Delta t}$ with $\Delta t = 1/2\pi\omega_r$.

The frequency comb signal can thus be effectively represented as $\omega_n = \omega_c + n\omega_r$ with n typically a very large number ($\sim 10^6$). While ω_c and ω_r are RF frequencies and, ω_n is typically an optical frequency.

As the phase velocity and the group velocity inside the cavity are not the same, each light pulse in the laser does not have the same absolute phase. The relationship between the phase velocity and the group velocity can be changed by changing the index inside the cavity, by changing the laser pump for example. The length of the cavity can also be changed independently to allow for a locking of both the repetition rate of the pulses and the offset of the carrier frequency of the laser.

If the spectrum of the laser is wide enough, it is possible to monitor the beat frequency of the tooth $2n$ and the frequency doubled tooth n: $2\omega_n - \omega_{2n} = 2(n\omega_r - \omega_c) - (2n\omega_r - \omega_c) = \omega_c$. Together with the monitoring of the laser repetition rate, this allows for the stabilisation of the tooth frequencies ω_n to fractional frequency stabilities comparable to RF microwave sources. In our case, the repetition rate of the laser is measured by measuring the 4th harmonics of the laser output, downmixing this signal with a DRO referenced by the microwave source and measuring the resulting beatnote on a photodiode.

In our case, we will use a Menlo F1500 comb, which is a mode-locked femtosecond laser broadened in a highly non linear fibre. It will be referenced to a microwave source, an oven controlled crystal oscillator (OCXO) (NEL 1326A) which provides a 10 MHz signal with a fractional frequency stability Allan deviation of 2 10^{-12} at 1s .

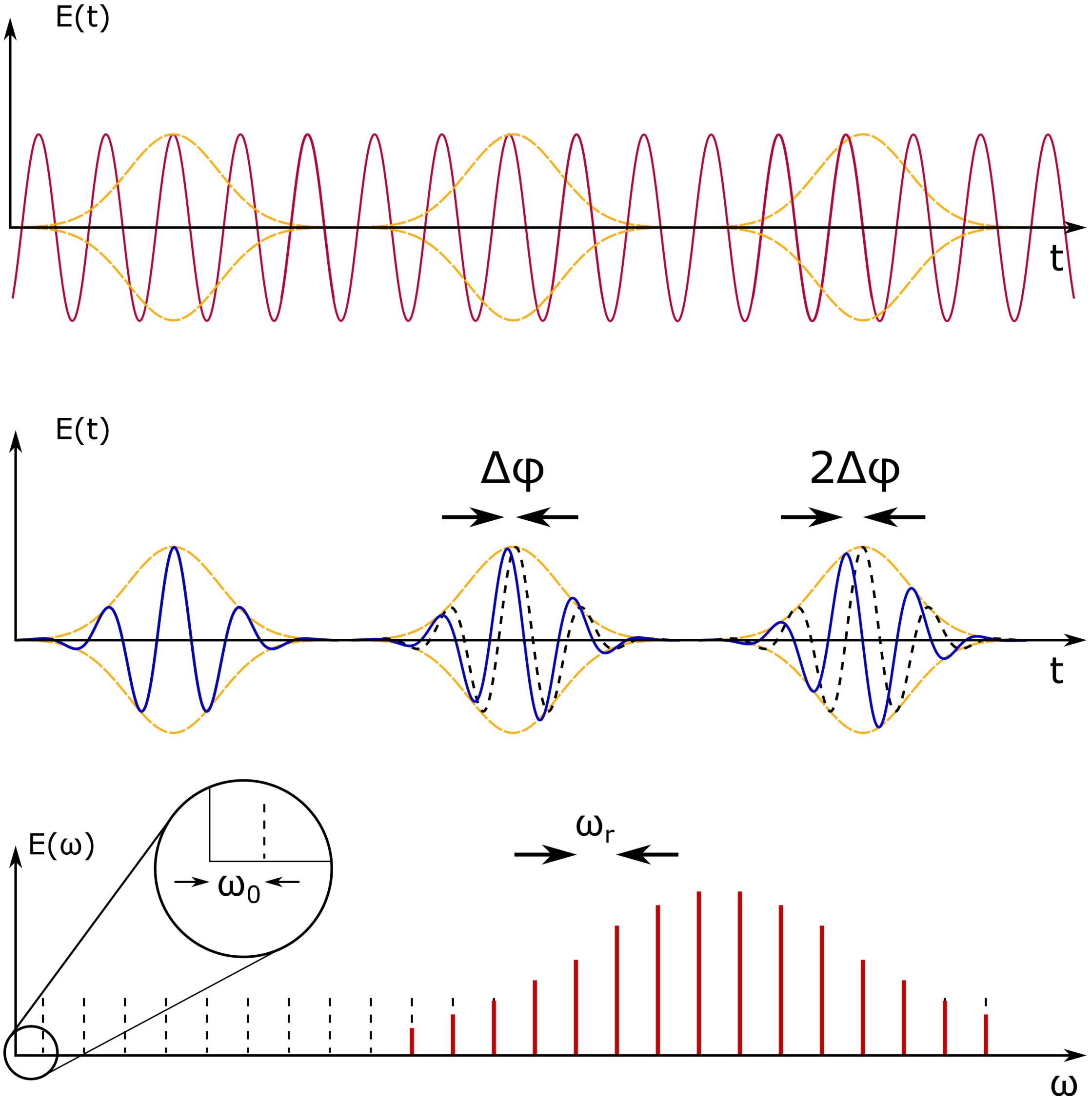

Figure 1.19: Consecutive pulses of a mode locked femtosecond laser and frequency representation of the laser's output.

FPGA frequency counter

The measurement of the fractional frequency stability are performed by analysing the stability of the beatnote between the laser locked on the reference cell and the laser locked on the fibre. The frequency of this beatnote is recorded using a frequency counter implemented with a RedPitaya board. As discussed in section 1.4.1, one can access most of the important information on an oscillator using a time series of the frequency output of the signal. A frequency counter has been implemented to measure the beat frequency of the reference cell locked laser with the laser locked on the fibre.

The Redpitaya board is equipped with $125 MHz$ ADCs whose performances are detailed in [67]. Those ADCs will be used to directly sample the beat signal, chosen to be at $\sim 3MHz$. The signals frequency is then counted using the frequency counter FPGA module presented in section C.1. This module outputs the number of oscillations of the signal averaged over a sampling period of $\tau = 1s$. The detection of each oscillation is carried using a threshold detector method. This number of oscillations is then recorded by the FPGA and can be converted back to a frequency.

The limit of this detection scheme has been tested with a Rigol DG4162 signal generator that fed a 3 MHz signal whose Allan deviation is shown in fig 1.20. It has a frequency stability starting at 5.10^{-17} at 1s, averaging at 1.10^{-17} at 15s and staying below 1.10^{-16} at 100s. So we see that the Redpitaya frequency counter will not be a limiting factor in measuring the Allan deviation of the laser's beat as it is orders of magnitudes below the reference cell's deviation (see section 2.1.3).

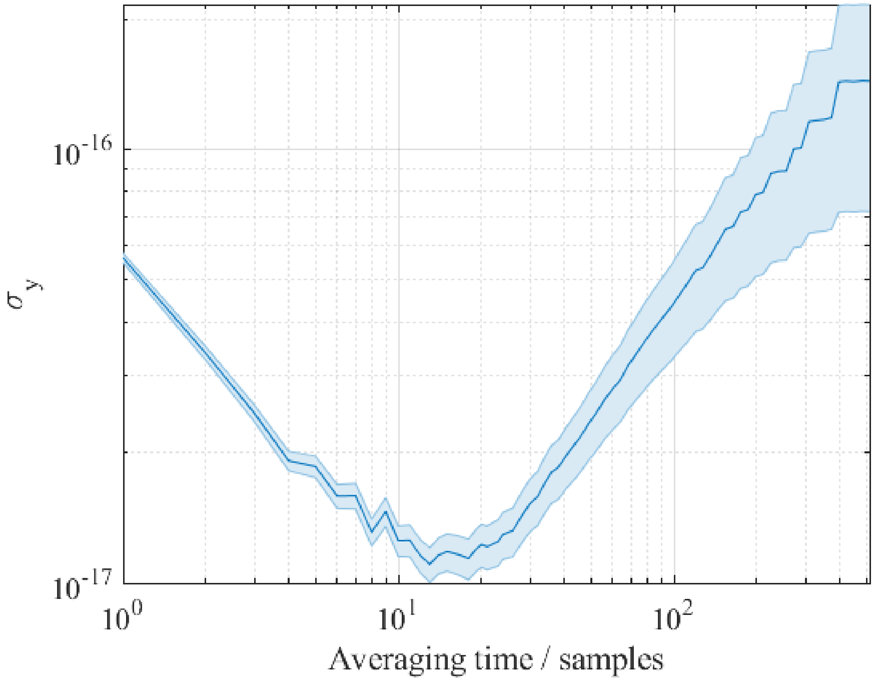

Figure 1.20: Allan deviation of the Rigol DG4162 signal's *fractional frequency instability*, with the normalisation frequency used being the P14 acetylene transition optical frequency. This normalisation is used to show the limit of detection when we consider the beat signal of the cell and fibre laser to be constant. The sample duration is 1 s.

We have shown that we can use the RedPitaya to measure and characterise the frequency of the beat between reference laser and the fiber locked laser in replacement of the comb. The frequency measurement will be used to characterise the fiber's stability.

1.5 Conclusion

In this chapter we have first presented the spectroscopy of acetylene molecule transitions, in particular the specificity of ro-vibrational transitions in the IR range compared to atomic transition in the same range and highlighted the resulting implications for spectroscopic measurements. We have then presented the different cells and geometries that are commonly used in the community to realize the spectroscopy of acetylene.

The chapter then proceeds to dissect various broadening mechanisms that impact the linewidth of transitions in acetylene. We have in particular discussed the Doppler broadening and we presented a technique, the MTS (Modulation Transfer Spectroscopy), to obtain a sub-Doppler signal that can be used for locking. We have also presented a numerical study of the impact of various experimental parameters such as the modulation amplitude and frequency on the MTS signal and shown that an optimal set of parameters can be reached.

We then discussed pressure broadening and shift, highlighting the role of collisions in the gas and their effect on the accuracy of the spectroscopy. Transit time broadening has then been analysed, stemming from the finite interaction time of molecules with the probing beam, further contributing to linewidth broadening. Additionally, multimode inhomogeneous broadening, induced by different propagating constants in fiber modes, has been examined for its influence on resonance frequency shifts in spectroscopy.

To close this chapter, we have presented the tools used to characterise the stability measurements of our laser systems. This section introduces Allan deviation as a metric for assessing frequency signal stability. It details the mathematical framework for Allan deviation, providing insights into its calculation and significance in evaluating oscillator stability. The chapter concludes by a description of the experimental setup for measuring Allan deviation, including a bulk cell as frequency reference and the implementation of a frequency counter for precise frequency stability analysis.

Chapter 2

Experimental Setup

In this chapter we detail the experimental setup used to carry the spectroscopy of acetylene in the hollow-core fibre, and to characterise the frequency stability of the laser locked on the hollow-core fibre. For frequency measurement, an optical comb was used in the beginning of this work. Unfortunately, it broke down during this PhD work. A second reference had to be built. A laser locked on a free space cell of low pressure acetylene gas is used as a reference with performances allowing for characterisation of the fibre without the need of the frequency comb. The setup and performance of this reference cell is presented first.

2.1 Reference Cell Setup

2.1.1 Optical bench

For the reference setup 2.1, a free space cell is used. It is custom made by Institute of Scientific Instruments, Academy of Sciences of the Czech Republic. The free space cell contains 0.5 Pa of C_2H_2 with no buffer gas. It is closed by 2 quartz wedged and coated windows to avoid reflections. The cell is 25 cm long, it is mounted on the bench in such a way to have a total of 3 passes for the two overlapping beams.

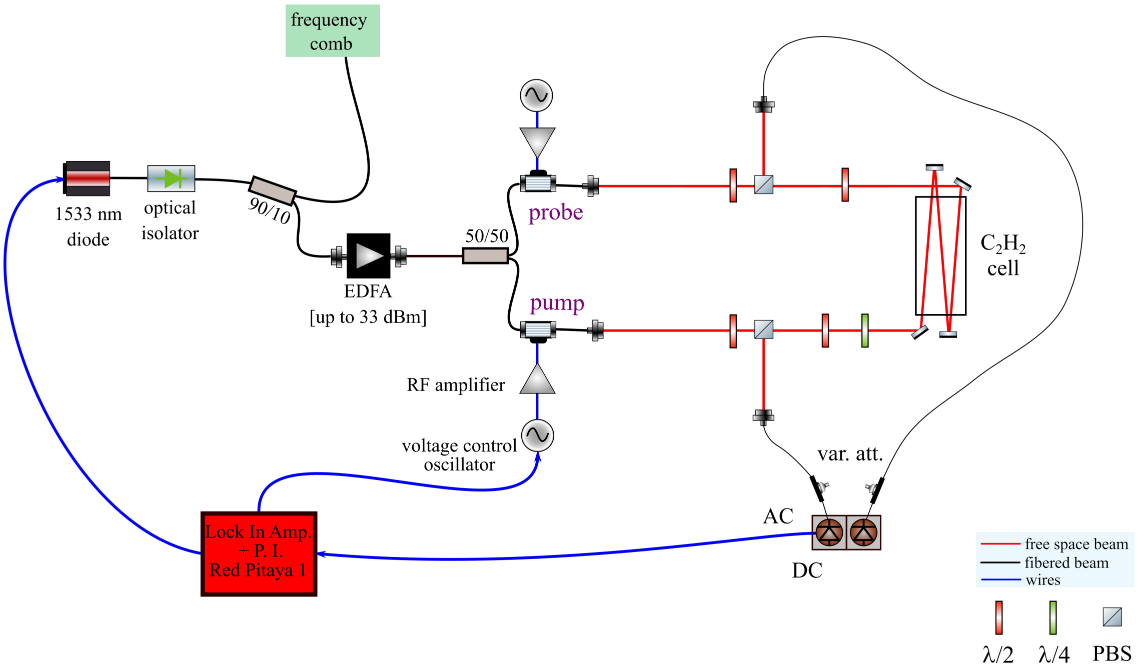

Figure 2.1: Free space setup used for MTS spectroscopy on a reference bulk cell.

The laser used is a 1533 nm RIO PLANNEX diode. It is powered by a µquans electronic board (38032-41) allowing for temperature and current driving and monitoring. It also has 2 input ports with high gain and low gain current modulation. The laser linewidth has been measured to be below 15 kHz, which should not be a limitation on the spectroscopy.

The laser diode is protected by a fibred isolator (AFR PMI-1-1530-P-2LQF). The light is separated by a 90/10 splitter (AFR PMFC-1550-410F-001). 10% is used for a beat detection inside the Menlo frequency comb. This was used to measure the laser frequency stability shown in Fig 2.11. The rest of the light is fed in a 2W Keyopsys EDFA. The light is then split to form the probe and pump arms.

The pump arm has a 80 MHz acousto-optics modulator (AOM) (G&H PM-fiber-Q) which is modulated in frequency. Because of the frequency dependence of the AOM's transmission, some residual amplitude modulation (RAM) is observed (see Fig 2.2). This introduces modulation amplitude of both the residually coupled zero order light but also the injected first order. The zero order will not be frequency shifted. This zero order pump component can interact with the probe via FWM inside the cell. It creates an undesired parasitic signal on the probe at the modulation frequency.

To avoid this phenomenon, a second AOM is used on the probe arm at an operating frequency shift a few MHz away from the pump's AOM frequency. This doesn't prevent some zero order probe light to interact with the modulated zero order pump. Nevertheless, the zero order beams are both greatly reduced in amplitude making the wave resulting from the FWM interaction between the zero order interaction much weaker and essentially disappearing in the noise. The typical RAM beatnote intensity gets reduced from -29 dB (Fig 2.3) to -29 dB -29dB $= -58$ dB (Fig 2.3) compared to the measured signal.

The light going out of the AOMs then passes through a Glan-Taylor polariser that

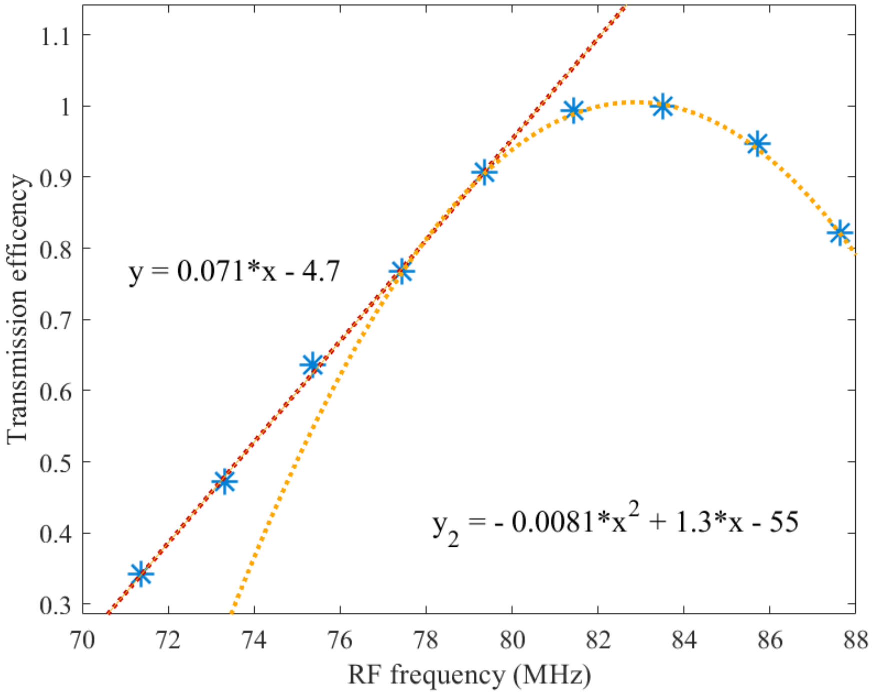

Figure 2.2: Experimental power response of the AOMs vs the input RF frequency. As the AOM's are fibred, the transmitted power depends on the RF shift frequency. The displacement of the beam inside the AOM can reduce the coupling to the outgoing fibre. The transfer function of the AOM can be fitted linearly in the range [70-80] MHz. Near the maximum of transmission, it can be fitted by a quadratic function.

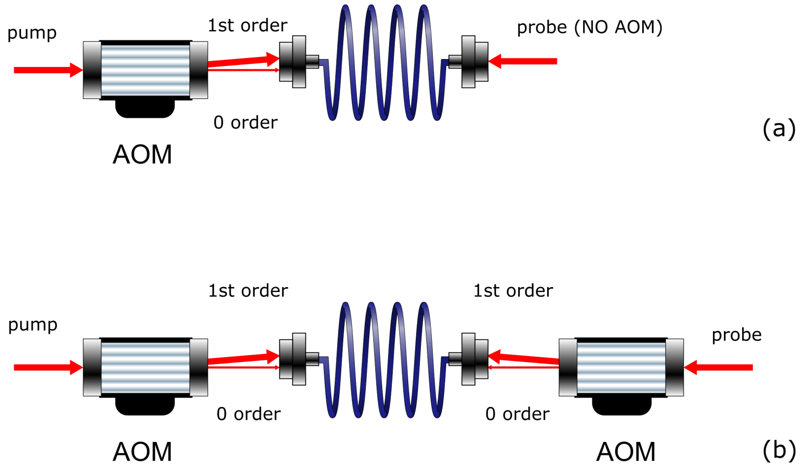

Figure 2.3: (a) AOM zero order diffraction leakage in the fibre with no AOM to shift the probe frequency. The zero order frequency that is modulated in amplitude will beat with a strong unmodulated probe signal. (b) AOM zero order diffraction leakage in the fibre with AOM to shift the probe frequency. The zero order modulated probe beam can beat with either a strong shifted 1st order probe beam, leading to a beatnote far from the demodulation frequency; or it can beat with the zero order leakage of the probe's AOM which will have a reduced impact on the demodulated signal compared to (a).

filters the beam's polarization. It then passes through a half waveplate followed by a polarizing beam splitter cube (PBS). This allows for power control of the beam. After the cube, polarization optics are used to match the pump and probe polarization inside the multi-pass cell. This maximises the MTS signal. The signal is picked up on a custom balanced photodiode that compensates for common mode fluctuations on the two arms of the bench.

2.1.2 Electronic Setup

During this work, an effort has been made to get most of the electronic function needed with an FPGA. This provides the ability to modify the electronic functions by software and still remains an embedded system. Nonetheless we still need electronics for frequency generation and optimisation of communication of the FPGA board with analog signals. The electronics used for frequency generation are detailed in this section.

Free space modulation and demodulation parameters

The different frequencies δ needed for the spectroscopy are dictating the design of the electronic chain for the pump's AOM. We will need to provide a RF signal with a frequency modulation δ and modulation factor M corresponding to the parameters of the MTS optimisation carried in section 1.2.3. This gives a good starting point but some exploration around this starting point can be required to get a more favourable SNR and slope. Indeed the RAM on the bench can modify the MTS signal in an unpredicted manner.

For the free space cell, the very narrow linewidth means that low modulation frequency are required to preserve the sharpness of the error signal ($\sim$ 10kHz). However the environmental noise coupled to a low absorption signal gives a poor SNR for $\delta \simeq 10$ kHz. In practice, we converged to a modulation frequency of 60 kHz.

On Fig 1.14 one can see that the higher the modulation parameter M, the higher will be the amplitude of the signal. In the case of a frequency modulation (as carried by an AOM), the modulation parameter is the ratio of the modulation amplitude over the modulation frequency. To maximise the signal amplitude, the modulation amplitude is selected to be the highest possible, ($M = 22.5$ with M the ratio of the modulation amplitude over the modulation frequency, called the modulation factor). However, a modulation amplitude too large means that the RF signal fall out of the AOM's bandwidth (see Fig 2.2). This limits the maximum modulation factor acceptable with our setup to $M = 22.5$.

Free space setup

As presented in section 2.1.1, the AOM needs a RF frequency centred around 80 MHz. This RF signal is generated with a minicircuit Voltage Controlled Oscillator (VCO) (ZOS-100+). This VCO can be tuned from 50 MHz to 100 MHz, allowing for important modulation amplitudes. It has a modulation bandwidth of 100 kHz which is sufficent for the free space cell linewidth spectroscopy. It is controlled and modulated with one of the output DAC of a Redpitaya [68]. The output of the VCO is fed into an amplifier (ZHL) and the resulting RF wave is sent into the G&H AOM.

2.1.3 Results

Due to a multiple air conditioning and electrical breakdowns, the frequency comb originally used in this project has been critically damaged and could not be replaced despite few attempts at the factory. Fortunately, a reference bulk cell setup has been developed and characterised with the comb prior to its final (see section 2.1.1) and could be used instead. The original intent was to use the cell as a three corner hat component together with the comb to get an absolute fractional frequency stability measurement of the fiber setup. In Fig 2.4 we show the performance of the free space reference which has been characterised with the frequency comb before it get damaged.

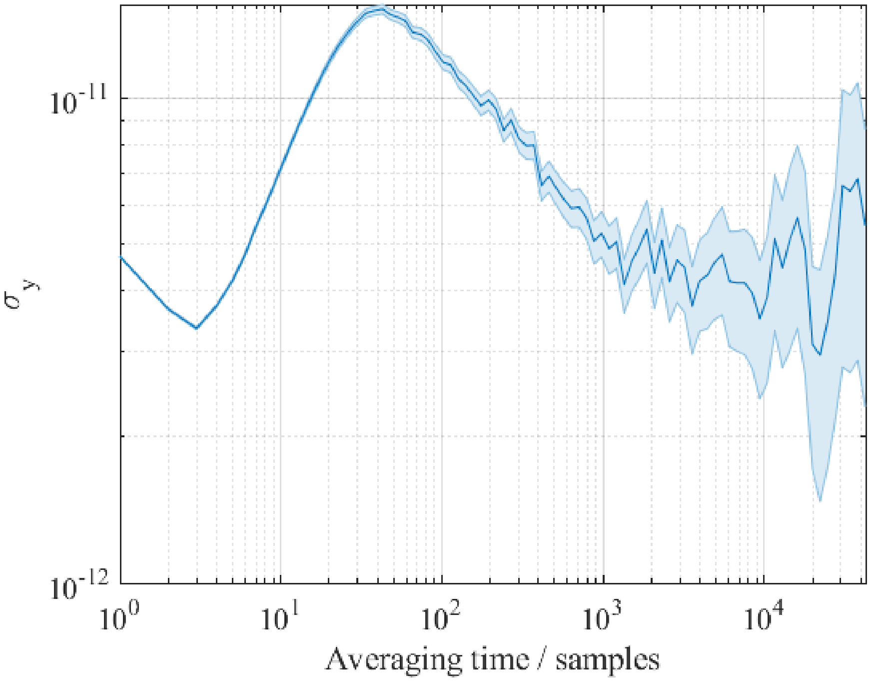

Figure 2.4: Allan deviation of the reference cell measured with the frequency comb. The bump at 40s is on the same timescale than the air conditioning cycles in the lab. The fractional frequency stability is 1 order of magnitude below the one measured with the fibre stabilised laser. This makes the cell a viable frequency reference to measure the fibre stability. The sample duration is 1s.

One can see on figure 2.4 that the Allan deviation of the cell is on a $1/\tau^{1/2}$ slope before and after the bump at 40s, which indicates the presence of frequency white noise (see table 1.1). This is expected as we are locking the frequency and not the phase of the laser. We can see a peak of noise at $\sim 40s$ which is close the period of the AC system in the room. Furthermore, the Allan deviation at timescales shorter than $\sim 40s$ has the same value as the OCXO used as frequency reference for the comb. Without more information, we could not determine which of the free space cell reference or the frequency comb was a limit for the measurement in Fig 2.4.

In section 3.1.6, we will see that all the measurements we carried on the different hollow core fibres had a fractional frequency stability above a few 10^{-11}. This is one order of magnitude larger than the free cell reference. After the comb breakdown, we therefore safely decided to use the free cell spectroscopy as a reference for all the fractional frequency stability measurements.

2.2 Fibre characterisation setup

To characterise the fiber spectroscopy to the reference setup, we lock a laser to the hollow-core fiber spectroscopy and compare the frequency of this laser to the one locked to the reference cell. The bench is based on the same MTS architecture than the reference bench. It allows measurement of external parameters such as power and polarization fluctuations.

2.2.1 Optical bench

A second setup, based on the primary reference setup is used for the fibre-stabilised laser lock. The laser used is also a 1533 nm RIO PLANEX diode powered by the same *μquans* electronics. It is also protected by a fibred isolator and 10% of the light is split for frequency analysis. The other 90% of the light is used as input for an second 2W Keopsys EDFA. The amplified light is split between a pump arm and a probe arm.

Both pump and probe go through G&H PM-fiber-Q AOMs. The probe AOM is driven by a fixed frequency RF source and the pump AOM RF driving field is frequency modulated to perform MTS. The center frequency of the probe and pump AOM are shifted by a few MHz for RAM reduction.

To perform further analysis on the fibre reference frequency stability, some elements have been added to the setup : a half-waveplate followed by a PBS filters the polarisation and another half-waveplate and PBS allow for power control. Both of the reflexion on the PBS cubes are monitored on low bandwidth (300 Hz) photodiodes, recorded every second by a Redpitaya. This setup is repeated for both the pump and the probe in order to evaluate the polarization and power fluctuations of the two beams before the fibre. This measurement device allow to look for correlation of the frequency instability to other fluctuations. It is also possible to monitor the state of one of the beams after the fibre simply by rotating the PBS cubes after the fibre.

After the cube, a half-waveplate and a quarter-waveplate are placed for optimum injection of the light in the fiber. This allows to find an optimum for the MTS in amplitude and SNR.

2.2.2 Fibred setup

In the fibre, the transition lineshape is much wider (from few MHz to tens of MHz), meaning that the modulation required for the different fibres should be of the same order. We cannot generate these modulations with the same material than for the free space cell.

The frequency modulations required for the fibred setup are higher than for the reference setup, and having a high modulation factor is still an advantage for the MTS signal (section 1.2.3). To reach high modulation factors with a 600 kHz modulation frequency, a source that can be tuned on a few MHz is required. Such a modulation range is easier

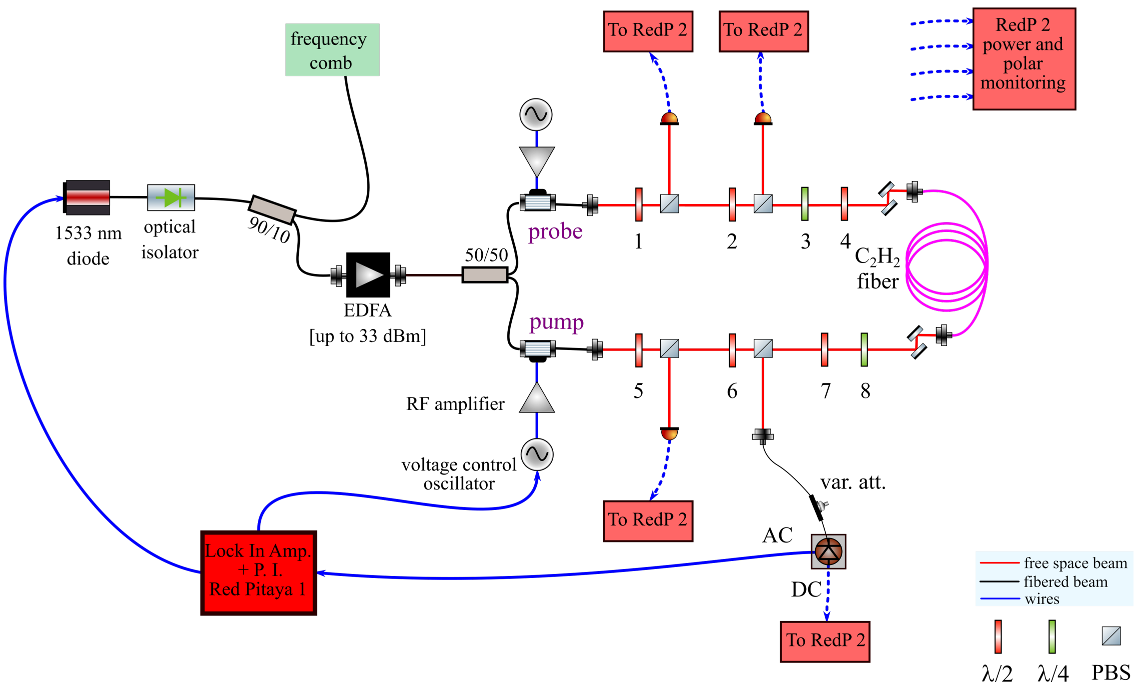

Figure 2.5: Fibre setup used to perform MTS spectroscopy on a PMC fibre. The architecture is the same than the reference bench with the addition of PBS that allow for monitoring of the power and the polarisation of the beams. It is possible to monitor beams as they go in the fibre, or as they go out simply by rotating the PBS by 90°.

to reach for a high frequency RF source, such as a ∼ 420 MHz VCO (minicircuit ZX95-470A-S+). This source can be tuned from 410 MHz to 470 MHz, which means that if it is mixed with a 500 MHz source, a 80 MHz signal can be generated with a frequency tunable over few MHz and controlled via the ZX95-470A-S+ frequency. The beat signal is filtered and amplified as presented in Fig 2.6. This allows us to generate and control a 80 MHz RF signal via the V-tune port of the VCO which is direclty connected to the RedPitaya.

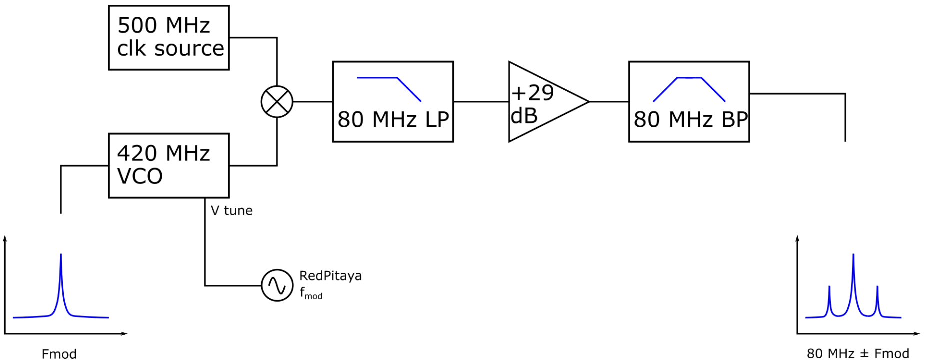

Figure 2.6: Bloc diagram of the electronic chain used to generate the AOM signal from the RedPitaya.

2.2.3 Fibred modulation and demodulation parameters

For the hybrid fibre, the measured lineshape is 7.6 MHz. The optimal parameters for the MTS have been obtained by scanning the modulation frequency, modulation amplitude and phase demodulation.

For each set of parameters, we have recorded the error signal obtained when the laser is scanned through the resonance. As the optimisation is not as direct than the free cell, a scan of the modulation parameters was conducted (see Fig 2.7). Typical data are shown in Fig 2.7 and Fig 2.8, the demodulated signal is filtered with a 5 kHz bandwidth for Fig 2.7 and Fig 2.8.

In Fig 2.7, we present the MTS obtained when the demodulation phase is scanned from 0° to 90° which allows to retrieve the optimal demodulation phase as the amplitude of the error signal changes depending on the demodulation phase as expected in section 1.2.3. The four plots corresponds to 4 different modulation frequency (400 kHz, 500 kHz, 600 kHz, 800 kHz). The data are taken with a repetition rate of $\sim$ 1.2s between each phase measurement.

In Fig 2.8, we show the scan with different views for clarity, for the 600 kHz modulation frequency case.

To characterise the error signal for every value of δ, we define the slope, amplitude and noise. The maximum and minimum points of the signal are found, the amplitude difference and slope is defined as the amplitude and slope between these two points. The noise level is determined as the RMS level of the signal in the region outside of the error signal. From this noise level we can derive a signal to noise ratio (SNR) by comparing the noise level to the amplitude of the error signal. The result of this study of the error signal is shown in Fig 2.9.

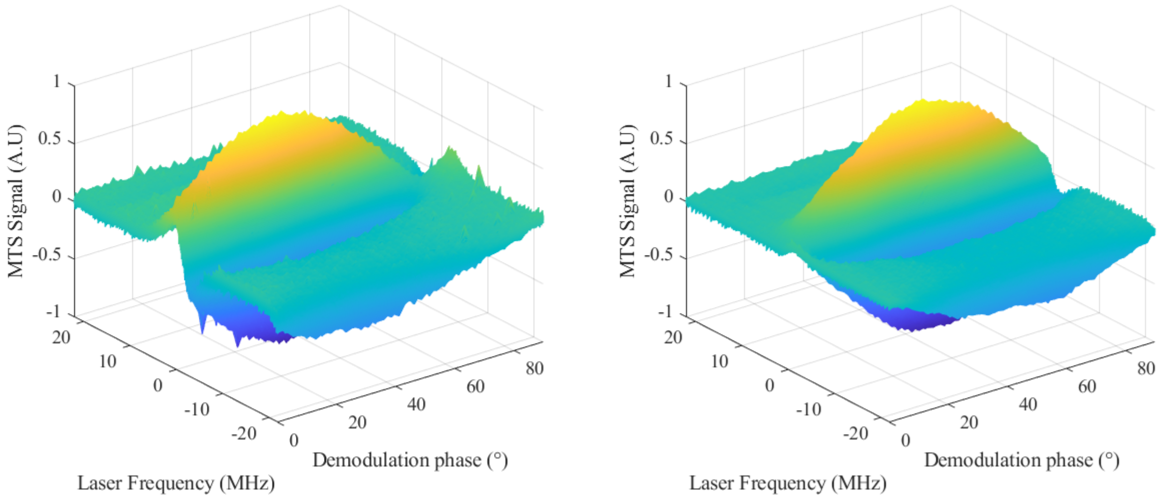

(a) $\delta = 400$ kHz (b) $\delta = 500$ kHz

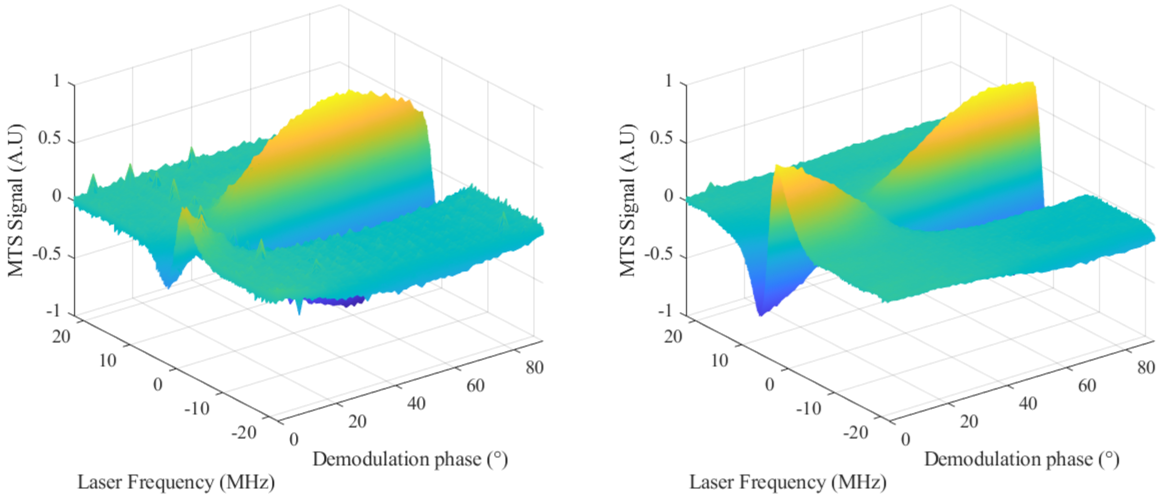

(c) $\delta = 600$ kHz (d) $\delta = 800$ kHz

Figure 2.7: Examples of the scans performed to find the optimum error signal. The laser frequency is ramped by the RedPitaya using the current modulation port. The resulting MTS signal is recorded as the modulation phase is incremented between each ramp. The scan procedure is repeated at different modulation frequencies to find the best error signal. The MTS signals presented here are filtered with a 5 kHz bandwidth after demodulation.

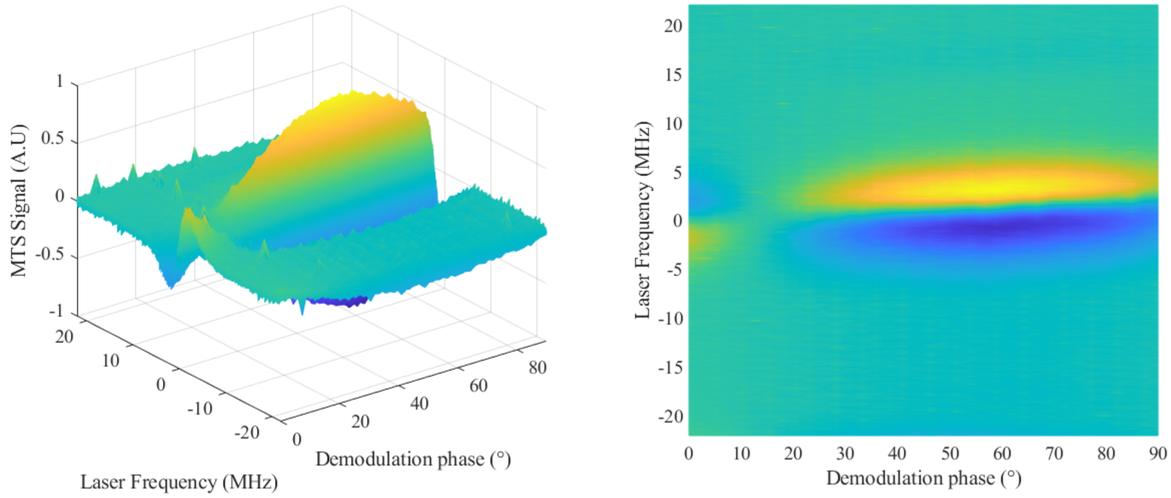

(a) $\delta = 600$ kHz (b) $\delta = 600$ kHz

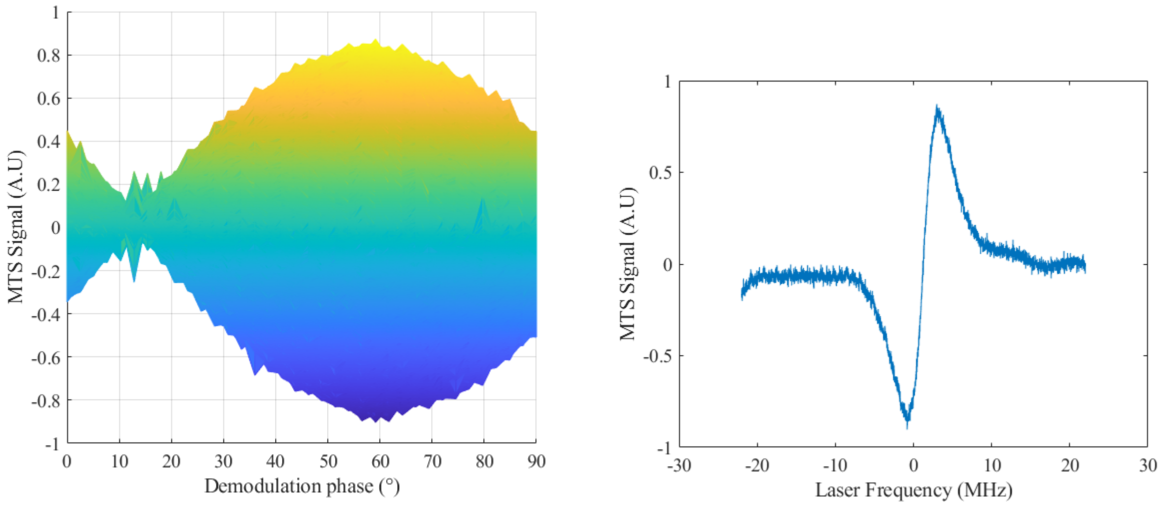

(c) $\delta = 600$ kHz (d) $\delta = 600$ kHz

Figure 2.8: Examples of the scans performed to find the optimum error signal. (a) Side view of one the scan. (b) Top view of the scan. (c) Side view of the scan. (d) Cut along the demodulation phase plane of the maximum amplitude MTS signal. The MTS signal presented here is filtered with a 5 kHz bandwidth after demodulation.

These scans allow us to determine the slope and SNR of the signal for different modulation frequencies to find the optimal set of parameters to use for laser locking.

The optimisation led us to choose a modulation amplitude of 3 MHz, the demodulation phase has been fixed by maximising the MTS signal peak to peak amplitude.

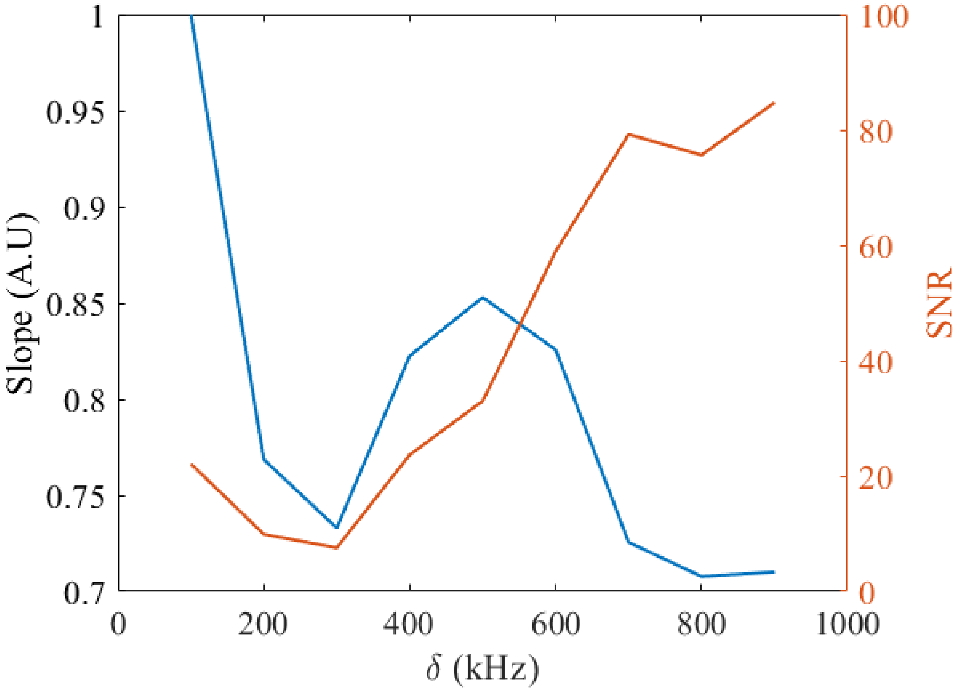

Figure 2.9: MTS signal experimental slope (left) and signal to noise ratio (SNR) vs modulation frequency. The slope is normalised with the sharpest experimental signal.

We can see on Fig 2.9 that a good compromise can be made at 600 kHz for the modulation frequency, to get the best slope and SNR possible on the error signal.

We chose after optimisation a modulation frequency of 600 kHz and a modulation amplitude of 3 MHz.

RAM on the error signal

As shown in section 1.2.3, RAM can create some asymmetry in the error signal, which will degrade the laser stability. We present here some scans that illustrate the effect of RAM. The scan presented in Fig 2.10 was performed on a different fibre (PMC 17 see annex A) with a larger linewidth of $\sim$ 30 MHz. We can observe on Fig 2.10 that the error signal is more noisy that on previous figures. In particular the signal presents oscillations which are due to partial reflections leading to some etalon effects. The presence of RAM can be observed in the asymmetry of the error signal (Fig 2.10d). In our setup, this large amount of RAM comes from the modulation bandwidth ($\sim$ 10 MHz) of the fibred AOM that were used to generate the frequency modulation at 9 MHz.

Experimentally, we could compensate for the RAM by changing the polarisation of the beams going in the fibre to reduce the signal asymmetry. As can be seen in Fig 2.10d it is possible to find a demodulation phase where the amplitude is not the highest but the signal is more symmetric.

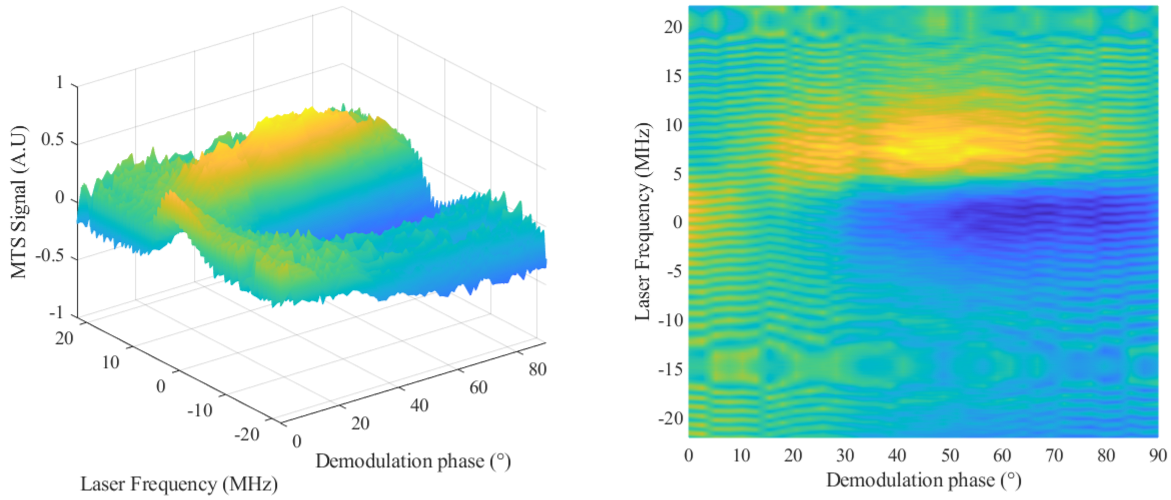

(a) $\delta = 9$ MHz (b) $\delta = 9$ MHz

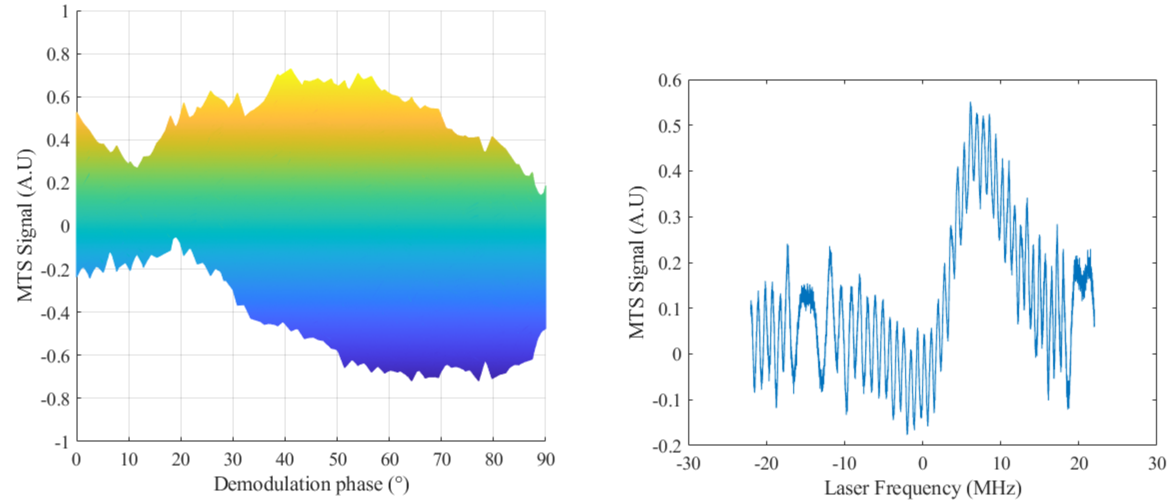

(c) $\delta = 9$ MHz (d) $\delta = 9$ MHz

Figure 2.10: Examples of the scans performed with RAM on the error signal. (a) Side view of one the scan (b) Top view of the scan. (c) Side view of the scan. (d) Cut along the demodulation phase plane of the scan. The cut is not along the maximum amplitude but is made to illustrate the asymmetry of the error signal (at $\sim 40°$). The MTS signals presented here is filtered with a 5 kHz bandwidth after demodulation.

2.3 Feedback

In the section, we present how the signal can be used to lock the laser. The lock is ensured by a closed loop. The error signal goes through a PID block inside the RedPitaya. The choice of the gains used in the PID is developed in this section. The Numerical output of the RedPitaya that is fed back to the laser is noisy, and careful consideration has to be taken to ensure the best laser stability.

2.3.1 Gain calculation

The lock of the laser is ensured by a RedPitaya for both setups. The output of the photodiode is collected and amplified as much as needed to get a 2 Vpp signal in the analog to digital converters (ADC). This allows for the best use of the 2^{14} values of the 14 bits conversion. As we are most interested in long term stability, the gain for the PID loop is not critical, and the precision achievable by the Redpitaya PID is well within the requirement and is not a limitation in the system.

More care has to be put on the digital to analog converters (DAC) output. The laser can be modulated using the two current modulation input ports which have different gains (110 MHz.V^{-1} on $HIGH$; 22 MHz.V^{-1} on $SLOW$). As the output precision of the Redpitaya has been measured to be 12 ENOB (effective number of bits) [69] on a $2Vpp$ range, we can expect a precision in frequency feedback of $\sim 5\ 10^{-11}$ in fractional frequency, which can be on the order of magnitude of the measured short term stability of our system. Thus it is needed to attenuate the output of the Redpitaya to ensure the precision of the output never limits the system stability. This has been shown to be a limitation in the reference cell performance, but not for the fibred cell setup (see Fig 2.11).

We present in Fig 2.11 the Allan variance of the reference cell measured by the comb when the analog gain between the DAC and the laser modulation input ports is changed. We can see that a factor 2 reduction in the gain lead to a factor 2 improvement in the laser stability. It should be noted that in both case the total loop gain remains the same, as the numerical (inside the RedPitaya) PID gain where increased by a factor of 2 to compensate for the attenuation.

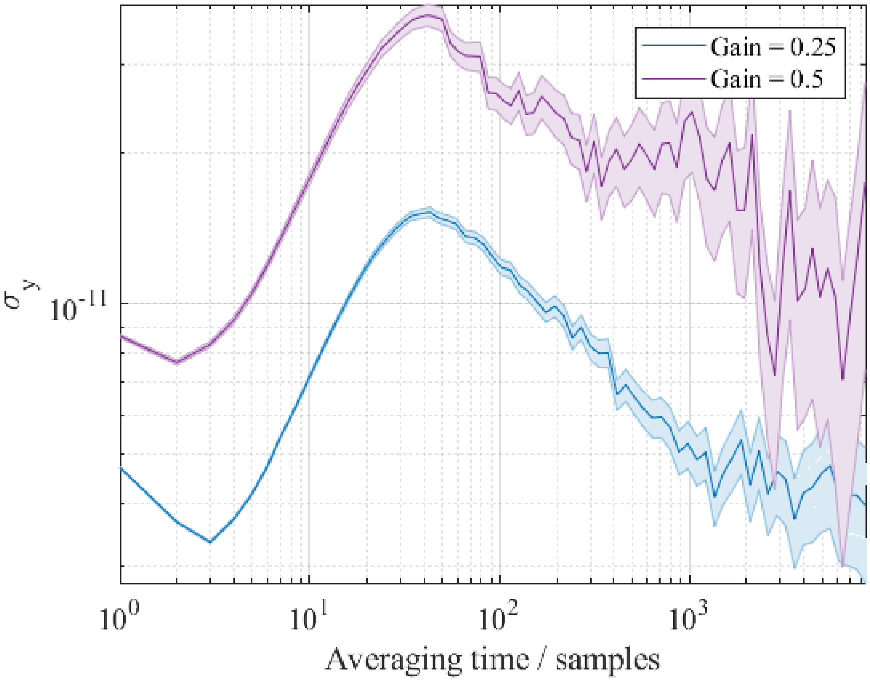

Figure 2.11: Allan deviation of the reference cell laser with different gain between the Redpitaya DAC output and the laser modulation input ports. The violet curve is given for a gain of 0.5 between the output of RedPitaya and the laser. The blue curve is given for a gain of 0.25. The numerical gain of the PID loop is doubled for the violet curve to keep the same closed loop gain.

2.3.2 PI Gain scans

The influence of the PI loop parameters on short term stability has been studied. We saw that the gain in the loop were not affecting long term stability and were only relevant for short term measurements. One can see on Fig 2.12 that the integrator gain does not change the stability of the lock after 10s (10^5 samples), as the lowest cutoff frequency chosen was 0.1 Hz.

The most notable effect of the integrator gains is seen close to the cutoff frequency for each of the Allan variances. One can see that even with a factor $\sim$ 10 increase in the integrator cutoff frequency, no change is made to the Allan variance in the long term. Therefore, the optimization of the cutoff frequency is not a critical parameter for the long term frequency stability.

The cutoff frequency used in the following is 10 Hz. This cutoff frequency allowed the laser to stay locked for many days, and does not limit the frequency stability for timescales > 1s.

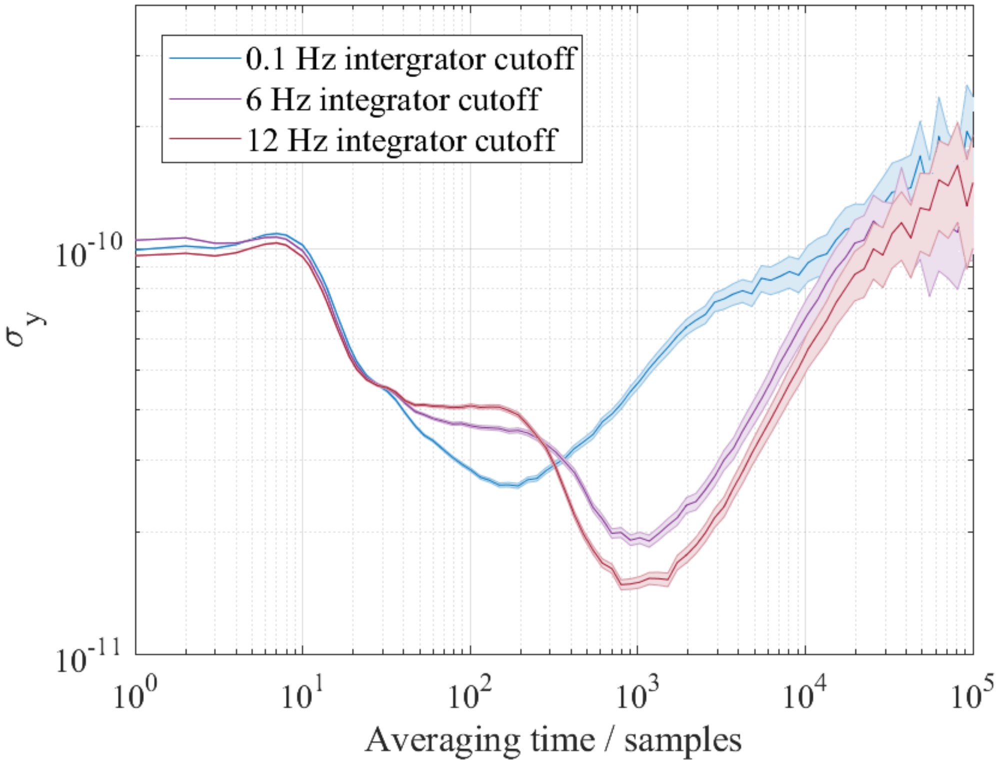

Figure 2.12: Allan variance of the laser frequency stabilised on a PMC fiber measured at 10k $samples.s^{-1}$. The short term stability of the laser is impacted by the PI gain but the stability at $10^1 s$ for all gain parameters remains the same.

2.4 Conclusion

This chapter provided a detailed account of the experimental setup and methodologies employed for acetylene spectroscopy in hollow-core fibers and characterized the frequency stability of a laser locked to these fibers. The chapter began with the description of a custom-made free space cell, crucial for the reference setup in the experiments. The optical setup to implement Modulation Transfer Spectroscopy (MTS) on this cell was detailed, and some details on residual amplitude modulation (RAM) that could impact the stability of the frequency lock were provided.

The chapter then detailed the electronic components and frequency modulation parameters necessary for optimizing the MTS signal. This included the use of FPGA for electronic functions, as part of the electronic chain of the pump's AOM, in the generation of the required RF signal for the modulation.

The next sections discussed the use of the bulk cell as a reference due to the breakdown of the frequency comb. The fiber spectroscopy was characterized in relation to this reference setup.

The chapter concluded with an examination of the methods used to optimize the MTS parameters, such as modulation frequency, amplitude, and phase demodulation. This process involved recording and analysis of error signals as the laser is scanned through the resonance to determine the optimal parameters for laser locking.

Chapter 3

Fibre sensitivity measurements

In this chapter we detail the stability measurement of a laser locked on different hollow-core fibers. We present the methods used to characterise the sensitivity of each fiber. The setup presented on the previous chapter is used here to correlate the different external parameters (temperature, power and polarization) to the frequency fluctuations of the locked laser. We also present the frequency stability of a laser locked on a hollow-core fiber in zero g conditions. We then compare the sensitivity and the stability measured for the three fibers measured.

The fibers used in this chapter were build by the GPPMM team at XLim. The first fiber used and presented in this work uses a guiding architecture built in the GPPMM team [70] which allows to have a large core with very few modes guided by the fiber. This fiber is 7.5m long with a core diameter of 30 µm and contains 7.5 Pa of acetylene. For the closing of this fiber, the ends of the hollow-core fiber are collapsed using heat to seal the gas.

After a successful observation of a SAS signal in this fiber, many attempts to built different fibers were made, targeting smaller core sizes to try to have a single mode fiber containing acetylene. It proved to be a challenging task, and it was difficult to obtain a predetermined amount of gas in the cell after the closing. Different closing techniques were developed by the GPPMM as an attempt to improve the spectroscopy, by removing the interferences at the fiber's endcap. Efforts were also made to make a splice with a single mode fiber in order to make a fully fibered system with an integrated frequency reference. Despite considerable efforts of the GPPMM team, we were able to observe SAS on only few of the fibers.

Among the successful realizations, two fibers showed MTS signal and were used to lock the laser. The first one called *PMC 16* is 3.8m in length with a core diameter of 14 µm. Using transmission measurement, the pressure in the fiber can be estimated at 60 Pa of acetylene. A second fiber was build, called here *PMC 17*, with a length of 2 m and a core diameter of 14 µm. The pressure of acetylene inside the fiber is estimated at 50 Pa. Both of these fiber were closed with the *angle rod* technique, describe in annex A and in Thomas Billotte's thesis [38].

3.1 Experimental results on stability measurements

3.1.1 Temperature Sensitivity

Temperature controlled platform

It is well known from previous works that temperature can be a factor degrading the frequency stability of a hollow-core stabilised laser [30]. To measure the influence of temperature fluctuations on our system, a heating platform has been built. We aim at controlling the temperature of the fibre and stabilizing it to improve the fibre performances.

The heating platform consists of a plateau with grooves for the fibre (see Fig 3.1) placed on top of two 39W Peltier heat exchanger (CP1.0-127-0.5L Laird Technologies) connected to a large aluminum block (see Figs 3.2). The aluminum block allows for good thermalisation of the Peltiers heat exchangers, the platform is locked in temperature using thermoresistors placed in two points of the plateau. The lock is performed by a 10 A TEC controller (PTC 10K-CH) which controls the Peltiers current. The lock-point of the TEC can be changed with a reference voltage fed to the TEC controller via a dedicated port. This allows for slow controlled variations of the fibre temperature.

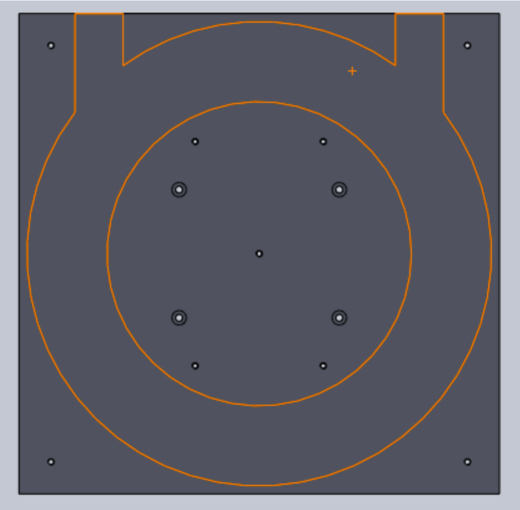

Figure 3.1: SolidWorks representation of the plateau hosting the fibre. This aluminium plate has grooves inside the orange area to allow for a placement of the fibre.

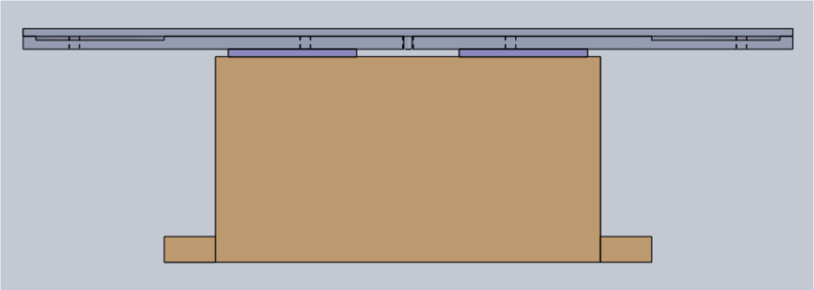

Figure 3.2: SolidWorks representation of the heat control system. The plateau nesting the fibre is mounted on top of two Peltier temperature controllers which are mounted on top of the aluminium blocks. The plateau is also screwed to the aluminium block with non thermally conductive screws.

Temperature sensitivity

For the temperature sensitivity measurement, we change the temperature in a controlled way and we measure the resulting laser frequency. On Fig 3.3 one can see that a sin wave of 1800s period is used as the set-point for the temperature controller. It is set to oscillate with a peak to peak amplitude of 2K. The beat frequency of the laser with the reference comb is monitored as the temperature is changed.

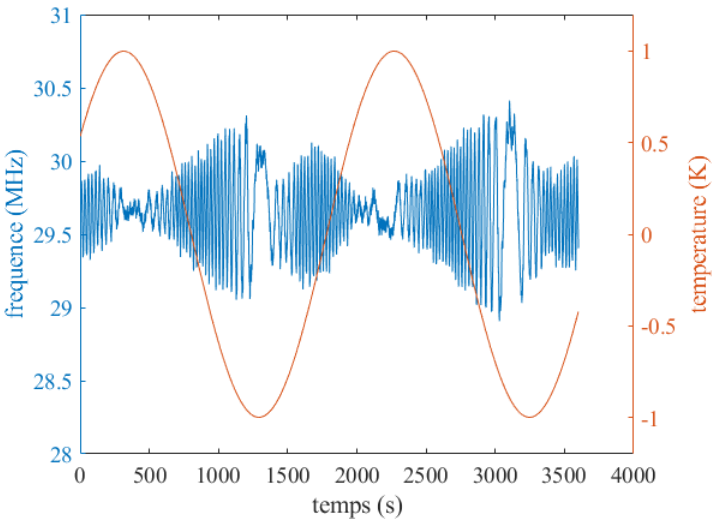

Figure 3.3: Measurement of the frequency of the laser by the comb (blue) vs temperature of the fibre (red). The temperature is modified by the Peltiers while the laser is locked on the fibre's spectroscopy.

We can see that the sensitivity to temperature is important ($\sim$ 14MHz/K) and associated to oscillations that resemble etalon effect (Fig 3.4). And that the total variation in frequency is $\sim$ 1.5 MHz. It is possible that the temperature fluctuations can modify mechanical constraints in the fibre, which can in turn change the mode content propagation in the fibre [30] [38].

The order of magnitude of the observed frequency shift could be explained by the modes inside the fibre used in this experiment. Shifts of the order of a few MHz have been

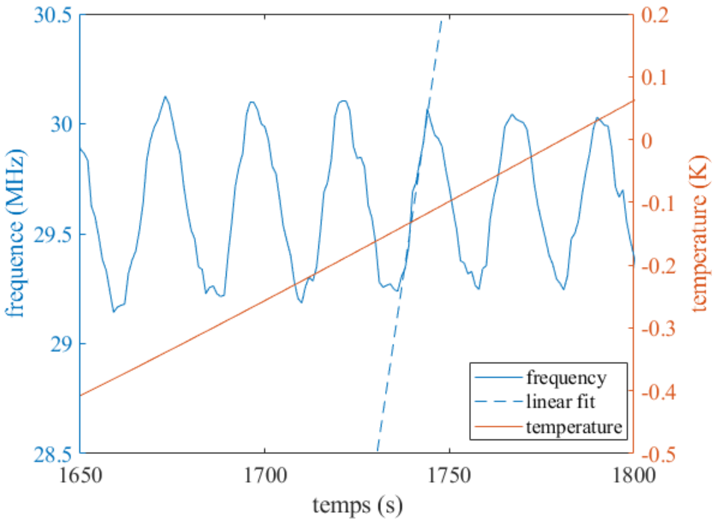

Figure 3.4: Zoom on the linear part of the temperature variations. The sensitivity can be measured as the maximum variation of the frequency in the oscillations. One can linearly fit the variation in laser frequency as well as the temperature to get an estimate of the temperature sensitivity of the fibre which is found to be 14 MHz/K.

observed in SAS spectroscopy when different modes are contributing to the spectroscopy [38]. The fibre's modal content we use is close to single mode but as the injection of the fibre is not perfect, we can expect to have higher order mode excitation than in [38], making the spectroscopy more sensitive to mode effect.

3.1.2 Polarization Sensitivity

A measurement of the sensitivity of the fibre with the incident polarization has also been performed. For the probe beam, the half-wave-plate number 4 (see Fig 2.5) is rotated to change the incident polarization angle. The error signal is shown has a function of the polarization angle in Fig 3.5.

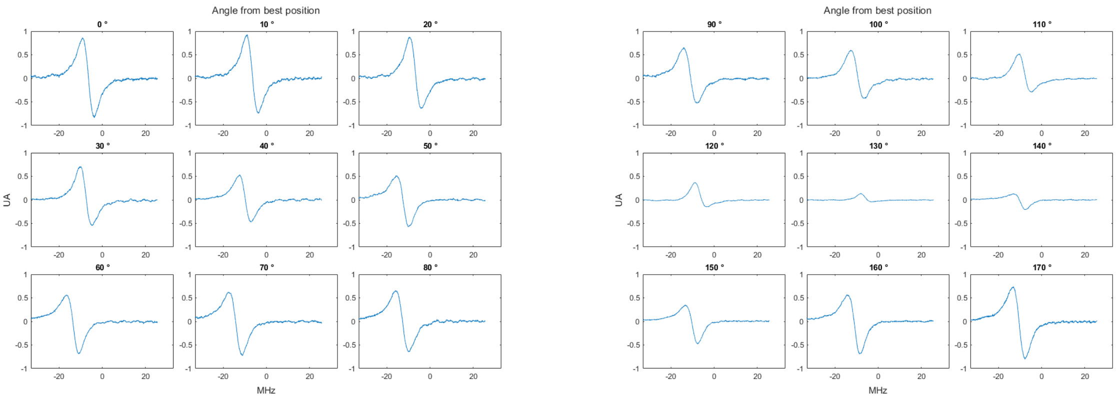

Figure 3.5: MTS signal after demodulation as the polarisation of the probe going into the fiber is changed. The polarisation is changed by turning a half-waveplate, the angle represented on top of the figures is the angle of the half waveplate from the optimized error signal position. The error signal is scanned by sweeping the laser's frequency and recorded. This measurement is repeated as the polarisation of the probe injected in the fibre is changed. The MTS signal is demodulated with a 5 kHz bandwidth.

As the laser is not locked during this measurement (which is 540s long), it is possible that the error signal drifts without any effect of the polarization. A scan of the error signal has been performed without changing any parameters to check for a drift in the free running laser that could be misinterpreted as a polarization effect.

Fig 3.6 presents this scan of the error signal evolving with time, with no variation done to the spectroscopy. We can assume that only the drift of the laser frequency is responsible for the fluctuations in frequency. We can see that at most, the laser fluctuations of > 5 MHz in about 1000 s.

Fig 3.7 shows the position of the zero crossing of the error signal. This measurement is not quantitative as the laser is not locked and therefore the frequency drift between two measurements is not known. However it is an illustration of the asymmetry of the error signal as the polarisation is changed, if we assume that the drift of the laser is smaller than the error signal (which is mostly true if we look at Fig 3.6).

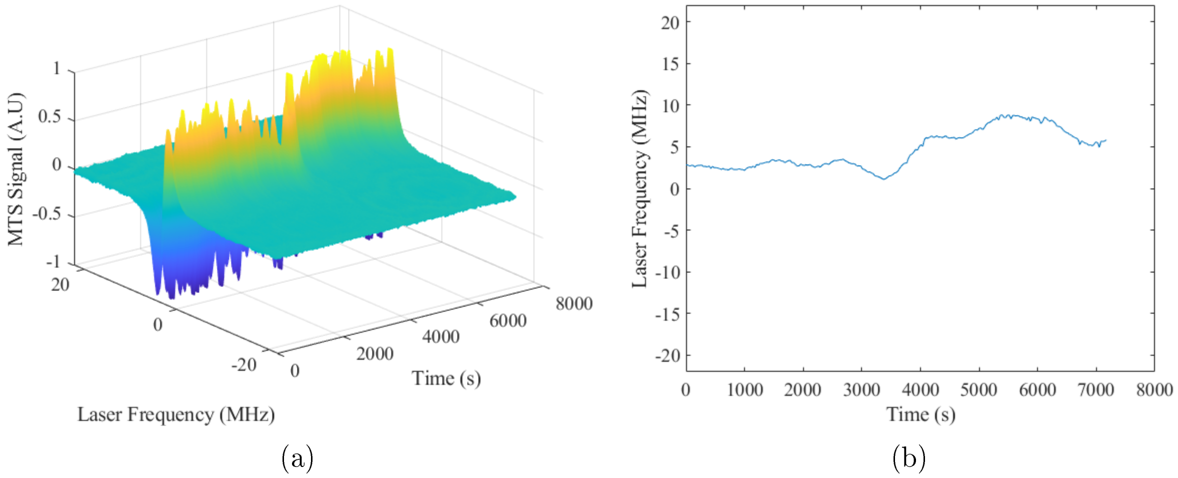

(a) (b)

Figure 3.6: (a) Scan of the error signal as the free running laser drifts. The laser frequency is swept during 1s every 30s to record an error signal. (b) The center of each error signal is represented.

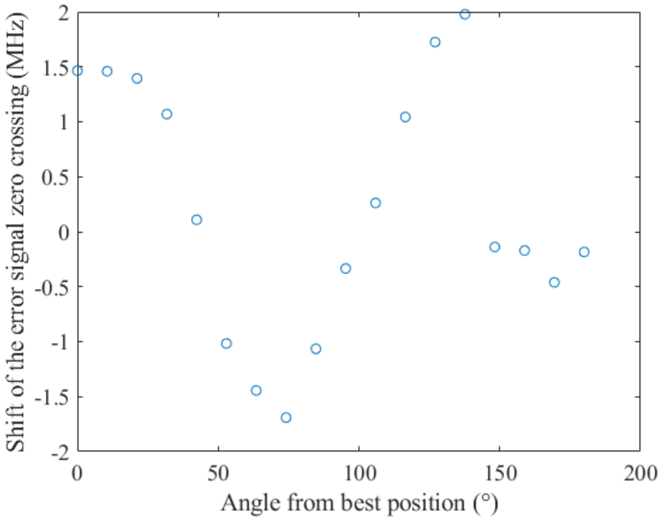

Figure 3.7: Measurement of the shift of the zero crossing of the error signal as the polarisation is changed. The laser's frequency has been centered around 0 for readability. The angle represented in the horizontal axis is the angle of the half-waveplate placed in front of the fibre, meaning that the actual polarisation of the probe beam is tuned by twice this angle.

On Fig 3.8, the amplitude of the error signal is represented while the polarisation is being changed. We expect an amplitude reduction of the error signal because the polarization crossover between the pump and the probe as seen in Fig 3.8.

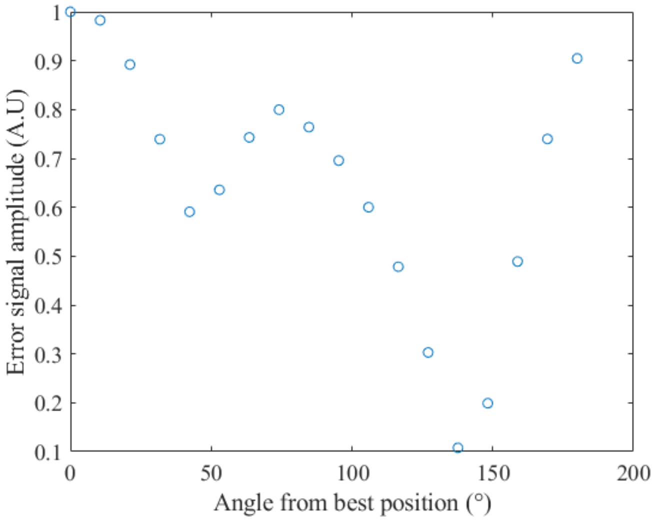

Figure 3.8: Amplitude of the error signal vs polarisation of the incident probe. The angle represented in the horizontal axis is the angle of the half-waveplate placed in front of the fibre, meaning that the actual polarisation of the probe beam is tuned by twice this angle.

Measurement protocol

To measure the fibre sensitivity, we turn the polarization injected in the fibre using the half-wave-plate number 4. The waveplate is turned by 4° every 30 seconds and the frequency of the locked laser is recorded. The photodiode 4 is replaced by a beam profiler (Thorlabs BP209-IR2) in order to see the beam displacement as the polarisation is changed. We expect the change in the output of the fibre far field to be caused by modal dispersion in the fibre, as it as been show for example by work that use multimode fibres for imaging [71], [72]. The fibre we use in our experiment only has a few modes [38], we make the hypothesis that only a few patterns will be observed in the far field [73], allowing for an analysis of the output without reconstructing the transmission matrix of the fibre.

Polarization Sensitivity

We can see the sensitivity of the fibre is 90kHz.deg^{-1} at the optimal point of lock (angle = 0°) (Fig 3.9). We can see that the beam is displaced coincidentally with the polarization angle, indicating a change in the wavefront of the fibre's output, caused by modes inside the fibre [72],[71]. The mode content is changed as the incident polarisation is changed. The total frequency displacement (∼ 10 MHz) indicates that RAM alone cannot explain the effect seen as it doesn't displace the centre of the error signal more than the error signal width (see section 1.2.3). However the ∼ 10 MHz displacement can be explained by a change in modal content of the fibre [38].

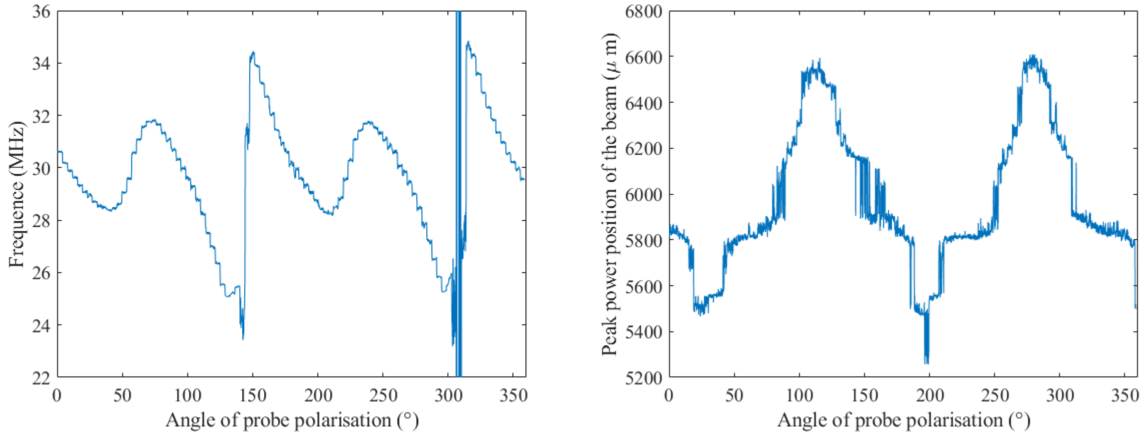

(a) (b)

Figure 3.9: (a) Measurement of the frequency of the laser by the comb as the polarisation of the incident probe is changed. The polarisation is changed by manually turning a half-waveplate. (b) Measurement of the centre of the beam reconstructed by the beam profiler as the polarisation is changed.

3.1.3 Power Sensitivity

Measurement protocol

The effect on frequency stability of the probe and pump beams power have been measured. To change the beam powers, the RF field used to drive the AOMs is modulated using the dedicated G&H Drivers (A35080-5-1/50p4k7u) for the pump, and a Variable Voltage Attenuator (VVA) (ZX73-2500+) for the probe.

For the pump beam, the VVA is driven using a sin wave of 1800s period, resulting in a power variation from 55mW to 5mW before the fibre. The laser was still locked even for the lower pump intensity.

For the probe beam, the G&H driver is modulated using a sin wave of 1800s period, resulting in a power variation of 100mW to 0mW before the fibre. The laser was locked down to $\sim$ 3mW of probe power.

For both beams, the frequency is then recorded as the power is changed. Then once the measurement is done, a calibration measurement using a power-meter is carried (ThorLabs S132C + PM100D).

Power Sensitivity

The measured sensitivity for the probe is 2.2kHz.mW^{-1}, and the measured sensitivity for the pump is 47kHz.mW^{-1}.

We can expect a discrepancy in the sensitivity of the two beams because the pump and the probe have different coupling to the fibre. $\sim$ 40% of the light injected at the entry collimator is collected at the output of the fibre for the pump beam, only $\sim$ 15% for the probe beam. This means that a reduction of the input of the probe beam means the effective reduction inside the fibre could be more important than for the pump.

However the coupling of one of the beams inside the fibre is not known (see Fig 3.10). According to section 1.2.3, both beam powers contribute equally to the amplitude of the error signal, but the effective power of each beam inside the fibre is not known.

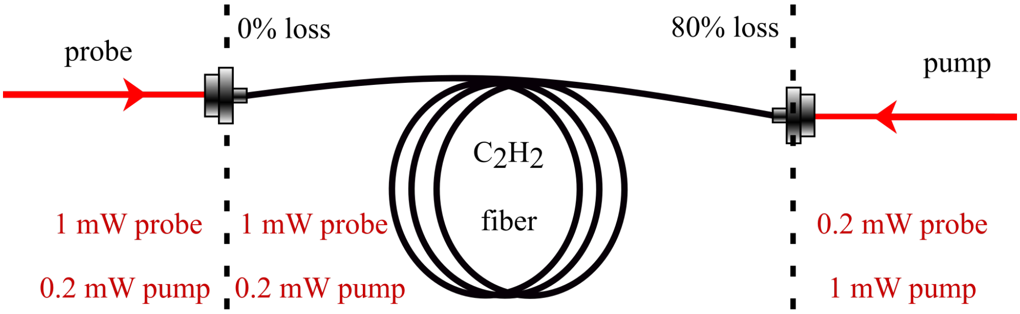

Figure 3.10: Representation of the transmission of the fibre. The losses in the fibre are not homogeneously spread across the propagation length. In our case, most of the loses are at the injection points, and both injection points may have different losses. We only have access to the total losses through the fibre, this means that the exact amout of light inside the fibre is not known.

Fig 3.11 shows the power sensitivity measurement of the pump. The pump power is changed via the VVA, the calibration measurement of the power modulation is represented on 3.11a. Then Fig 3.11b shows the frequency of the laser as the VVA's power is changed with time. The power fluctuation data are compared to the frequency fluctuations on Fig 3.11c and fitted with a linear curve. Colors have been used to indicate time for readability.

Fig 3.12 shows the power sensitivity measurement of the probe. The RF output of the AOM's driver is modulated using the dedicated input port. The calibration of the resulting probe power fluctuation is presented on Fig 3.12a. As the probe power is modulated, we measure the laser frequency shown on Fig 3.12b. The frequency fluctuations and the probe power fluctuation are then fitted on Fig 3.12c with a linear curve to get the probe power sensitivity.

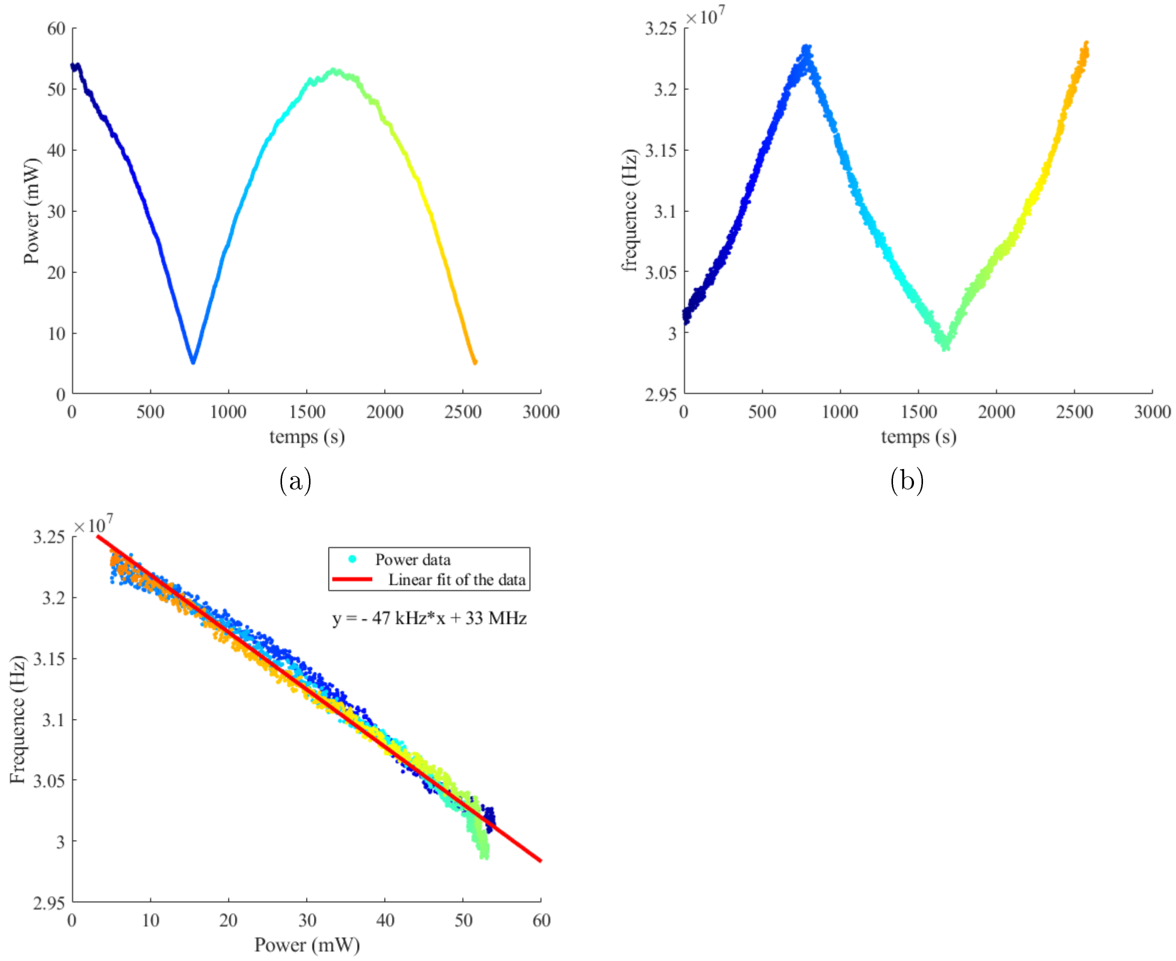

(a)

(b)

(c)

Figure 3.11: (a) Optical pump power going in the fibre vs time. The power is measured by applying the modulation to the VVA and measuring the beam power by placing a powermeter in front of the fibre. (b) Comb measurement of the frequency of the locked laser as the modulation is applied to the VVA. (c) Representation of the frequency datas as a function of the optical power fitted linearly.

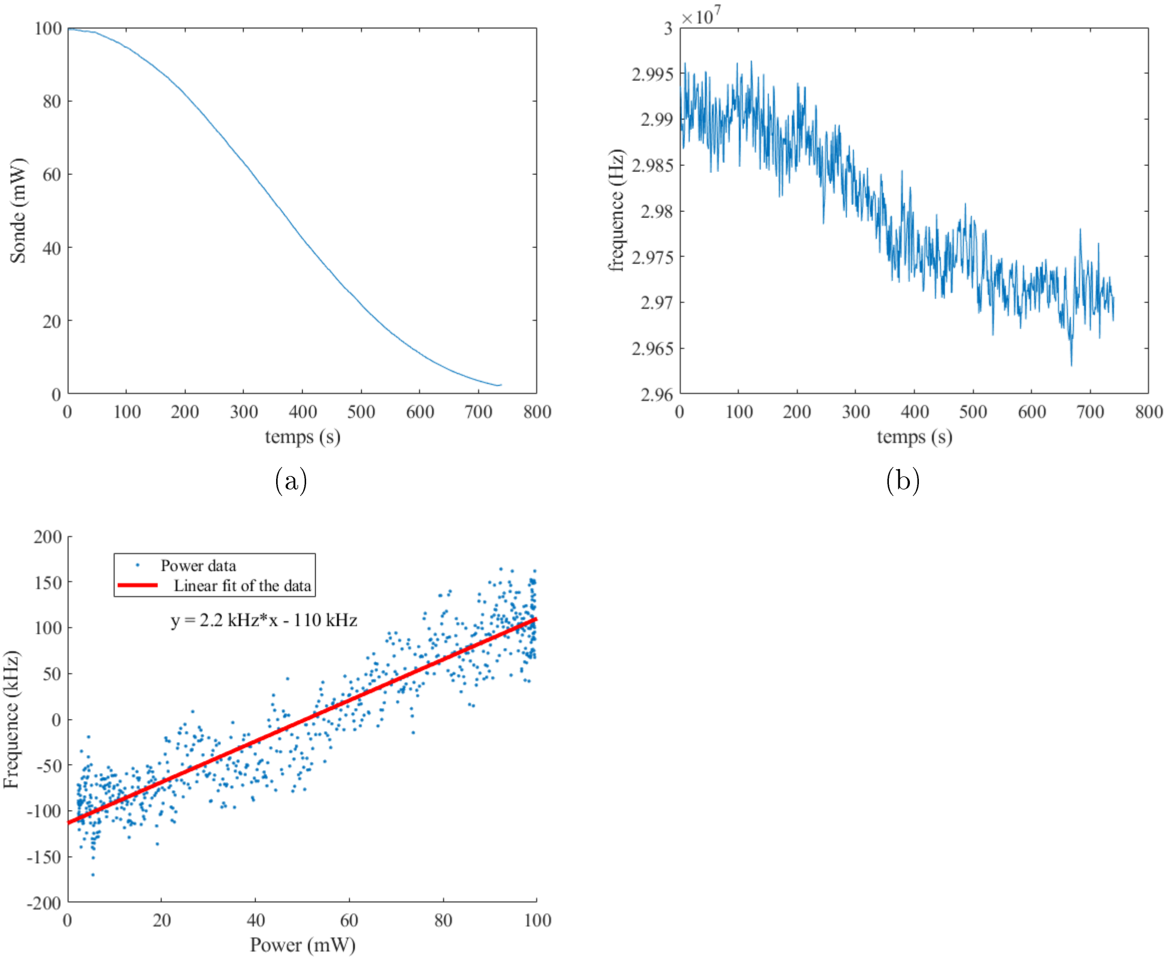

(a) (b)

(c)

Figure 3.12: (a) Optical probe power going in the fibre vs time. The power is measured by applying the modulation to the AOM's RF driver modulation port, and measuring the beam power by placing a powermeter in front of the fibre. (b) Comb measurement of the frequency of the locked laser as the modulation is applied to the RF driver. (c) Linear fit of the frequency data as a function of the optical power.

3.1.4 Injection Sensitivity

Measurement protocol

The fibre was also tested for injection sensitivity. The frequency is recorded, as the last mirror of injection is moved to create a displacement in the beam in front of the coupler. The mirrors are ThorLabs mount, (K1E3 for the pump, KM100 for the probe). On each mirror, the Y axis screw is turned by 45° resulting in a rotation of ~ 0.96 mrad of the K1E3 pump mirror, and of $\sim 1, 0$ mrad for the KM100 probe mirror. As the mirror mount are not the same, and the distance between the mirror and the coupler is not the same either, the total displacement is not the same. The total displacement is estimated with knowledge of the focal lens of the fibre collimator and the change in beam angle as the mirror is turned.

Injection sensitivity

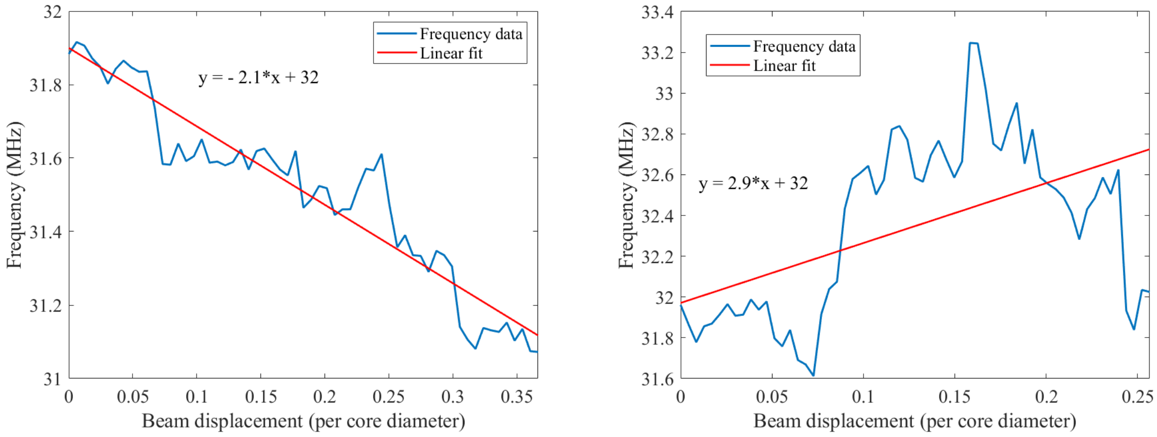

(a) (b)

Figure 3.13: (a) Frequency of the locked laser measured by the comb as the pump K1E3 mirror is turned. (b) Frequency of the locked laser measured by the comb as the probe KM100 mirror is turned. For (a) and (b) the horizontal axis and the x data for the fit is in units of the core diameter (30µm).

One can notice that the frequency stability behaves more linearly for the probe beam displacement than the pump beam. This can be caused by the fact that the total error signal also depends on the coupling between the outgoing probe beam and the fibred photodiode, as the total power on the detection photodiode can impact the MTS signal. But the outgoing probe beam is also reflected on the K1E3 pump mount, so misaligning it also impacts the probe signal output (Fig 2.5).

Beam displacement sensitivity probe : 98kHz.μm^{-1}; Beam displacement sensitivity pump : 71kHz.μm^{-1}

3.1.5 Acceleration sensitivity

A test of the robustness of the fiber lock has been made using a Zero-G platform in the lab.

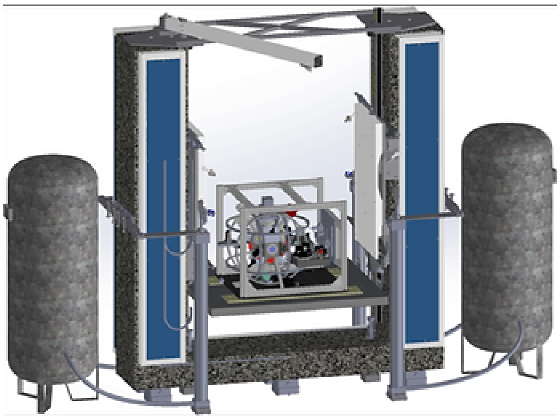

Figure 3.14: Zero G platform built by the company Symétrie.

The Zero-G platform is able to generate ∼ 0.5s of microgravity and is used for the ICE experiment in the LP2N. We were able to use it as a test platform for the robustness of the fiber lock in difficult conditions.

The fiber and the optical bench are subjected to an acceleration profile in the earth acceleration frame presented in Fig 3.15. Every ∼ 20s, a acceleration cycle is repeated. A cycle consist in a linear acceleration profile up to 1g to elevate the platform. The platform is then free falling in -1g until a recovery period were the platform goes back to its original position. After a cooling of the motors of the platform, the cycle can be repeated.

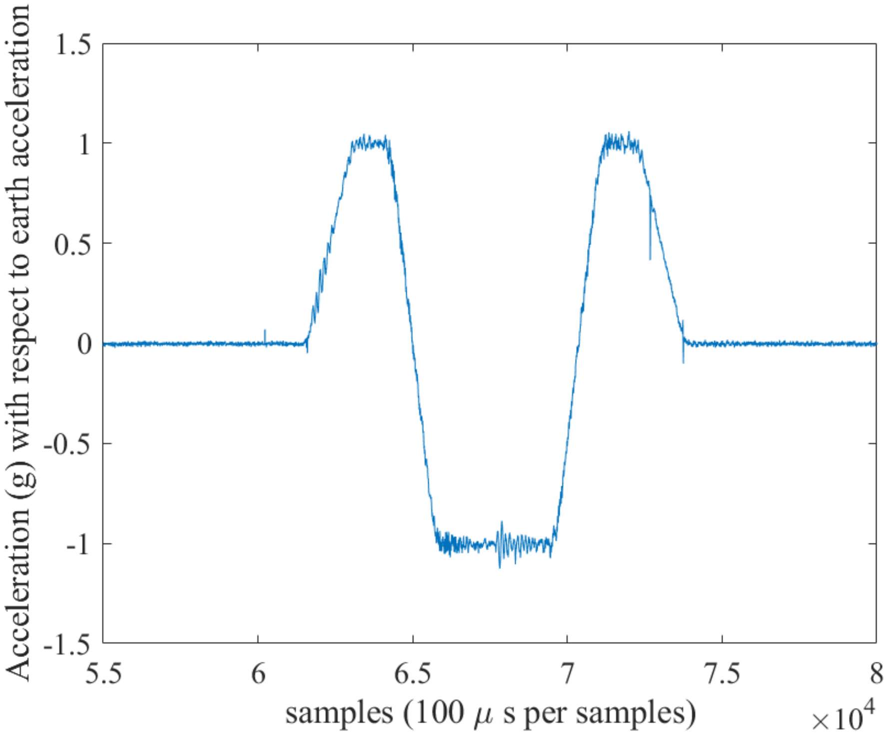

Figure 3.15: Acceleration profile of the Zero-G platform. The data is taken using an accelerometer placed on the optical bench.

Changes had to be made to the optical bench to be able to fit on the platform (see Fig

3.16). The changes were made to minimise the amount of optical component while still having one side of the fiber be free space coupled. The free space coupling is important for optimisation of the error signal and to have a strong separation of the outgoing probe beam and the input pump beam. An alternative solution using a fibered splitter did not allow to reach a sufficient amount of beam separation. Control of one of the injected beam's polarization is also important to ensure a strong enough MTS signal.

Figure 3.16: Compact free space bench for injection of the fiber. Connecting both side of the fiber using butt coupling did not yield a exploitable MTS signal. One side of the fiber had to be injected in free space.

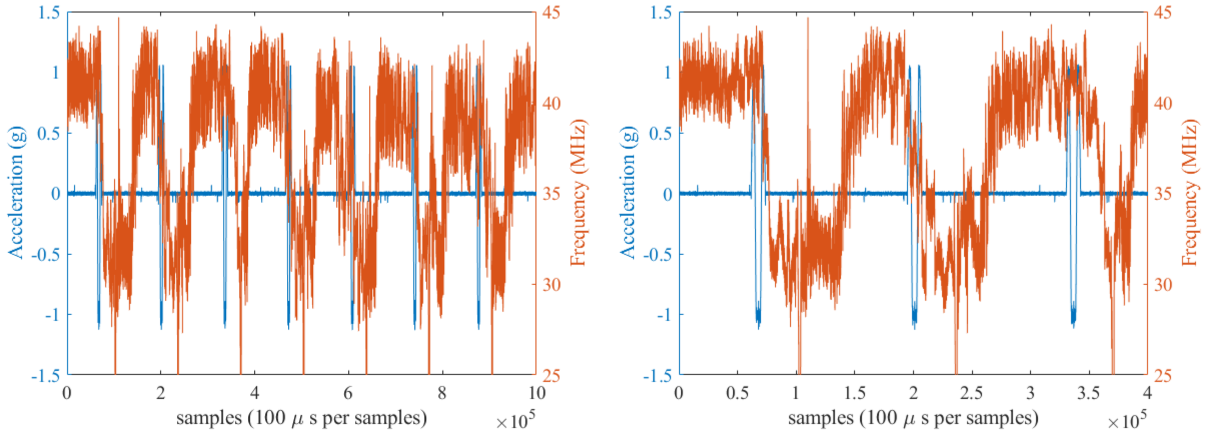

(a) (b)

Figure 3.17: Acceleration of the platform vs frequency of the locked laser

On Fig 3.17, we can see the frequency of the lock laser beating with the reference laser. While it is clear that the frequency is affected by the cycles of the platform, the frequency stability is restored after some time in the cycle. One can remark than the frequency presents an instability long after the platform stops moving. This is probably due to the fiber connecting the optical bench to the AOM, EOM, EDFA and laser which were installed separately on a stationary bench. Contrary to what we were expecting there is no very clear correlation between the acceleration and the laser frequency.

3.1.6 Correlated measurements

The sensibility of the fibre spectroscopy to different elements having been established, we will now measure the total Allan deviation of a laser locked on the fibre. During this measurement, the different parameters studied previously are recorded in order to estimate their contribution to the instability of the laser.

Probe power and polarisation correlation to the fiber temperature

As a starter, we show here the influence of the fiber temperature on the output probe beam parameters. A sinusoidal temperature modulation of 2K with period 100s is applied on the fiber, while the polarization and power of the outgoing probe beam are recorded.

On Fig 3.18 is represented the polarization angle of the probe beam after the fiber in blue, and in orange, the power of the probe beam after the fiber over time.

The probe is originally filtered in polarisation by PBS and unmodulated in power. It should therefore be constant, but it comes out of the fibre with the temperature modulation copied onto the power and polarisation of the beam. This can be explained by the thermal expansion of the fibre that changes the propagation indices of the fibre [31], [74].

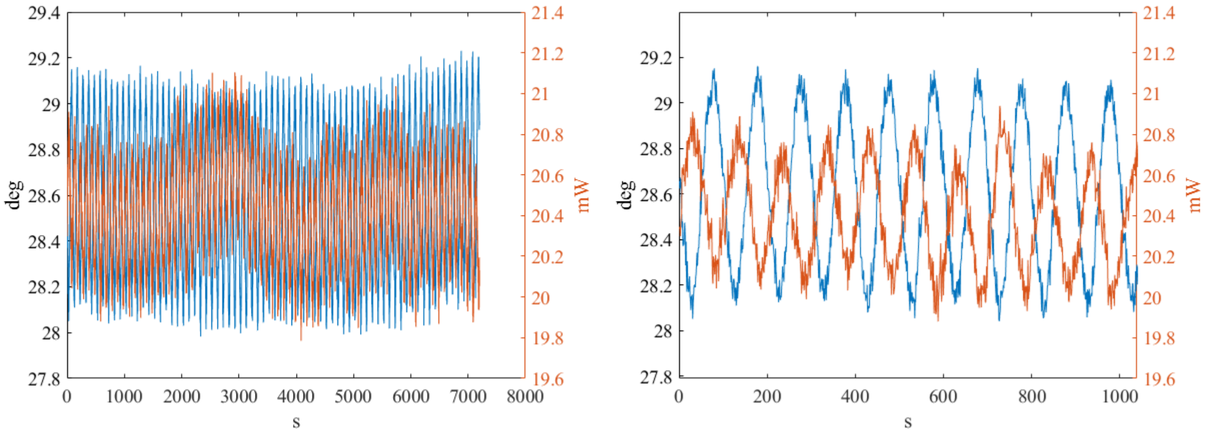

(a)

(b)

Figure 3.18: (a) Power and polarisation angle fluctuation of the probe after the fibre, with a temperature oscillation of the heating platform. The temperature oscillation is 100s in period and set at 2°C peak to peak. The resulting power and polarisation oscillation exhibit the same period as the temperature oscillation. (b) Zoom on the power and polarisation oscillation.

Multiparameter correlation measurement setup

The optical setup used for this measurement has been presented in Fig 2.5. With additionally the temperature controlled platform presented in section 3.1.1.

Redpitaya synchronization

Four RedPitaya are used for acquisition of various parameters of the fibre spectroscopy. Two RedPitaya are dedicated to the acquisition of the error signal and feedback of the fibre and the free space cell respectively. These datas were used to check for potential issues in the lock of the reference and fibre laser (i.e. to make sure the feedback loop were not saturated...). One RedPitaya is used to monitor the photodiodes that give the power and the polarisation of the probe beam before and after the fibre. Another RedPitaya is used to monitor the room temperature in the laboratory. All the RedPitaya are trigged to start a synchronous acquisition of the data.

Allan deviation of the laser locked on the fibre

Here we present the Allan deviation of the laser locked on the fibre.

It should be noted that we see a strong correlation between the ambient temperature in the room and the power stability of the probe and pump. Even though we have not measured the sensitivity of the beams to the ambient temperature, the strong correlation between Figs can indicate that the fluctuation in the beams couples the temperature fluctuation in the room to the final laser stability. Obviously this would be quite a limitation for using such fiber spectroscopy in a non controlled environment.

On Fig 3.19 we can see the short term stability at $\sim 1.2 \times 10^{-10}$ at 1s or $\sim$ 24 kHz indicates that the temperature is limiting the stability. At longer timescales, the Allan deviation is dominated by the power fluctuation of the pump, as it exhibits the same fluctuations, at the level expected by the power sensitivity measured in 3.1.3. The temperature fluctuation is shown with a slope of $\tau^{-0.35}$ that fit closer to the data.

The Allan deviation of the laser shows that the frequency stability is dominated at 1s by the temperature. The stability achievable by the TEC controller is specified at 0.0012°C which correspond to a frequency stability of 16.8kHz or $\sim 8.6 \times 10^{-11}$ in fractional frequency. (see section 3.1.1). The Allan deviation is limited by the power stability of the beams at longer time scales ($\sim 2.5 \times 10^{-11}$ at 2×10^{2}s), as the power stability of the pump at $\sim 2 \times 10^{2}$ s reach > 0.11 mW corresponding to $\sim$ 4.8 kHz (see section 3.1.3), or $\sim 2.5 \times 10^{-11}$ in term of fractional frequency stability.

A special case of a white noise PSD low passed at 100 samples has been simulated and is presented in Fig 3.20. This simulation is performed to give a plausible explanation to the $\tau^{-0.35}$ slope seen on the Allan deviation of the laser lock on the hybrid fiber (see Fig 3.19) that we assume is caused by temperature fluctuation.

We also show on Fig 3.21a the pump power measured before the fiber, this measurement is shown to be correlated to the frequency instability of the fiber. Fig 3.21b represent the fluctuations of temperature in the experiment and seems also correlated to the pump fluctuations. However we can't quantify a correspondence between these room temperature fluctuation and the power fluctuations of the laser.

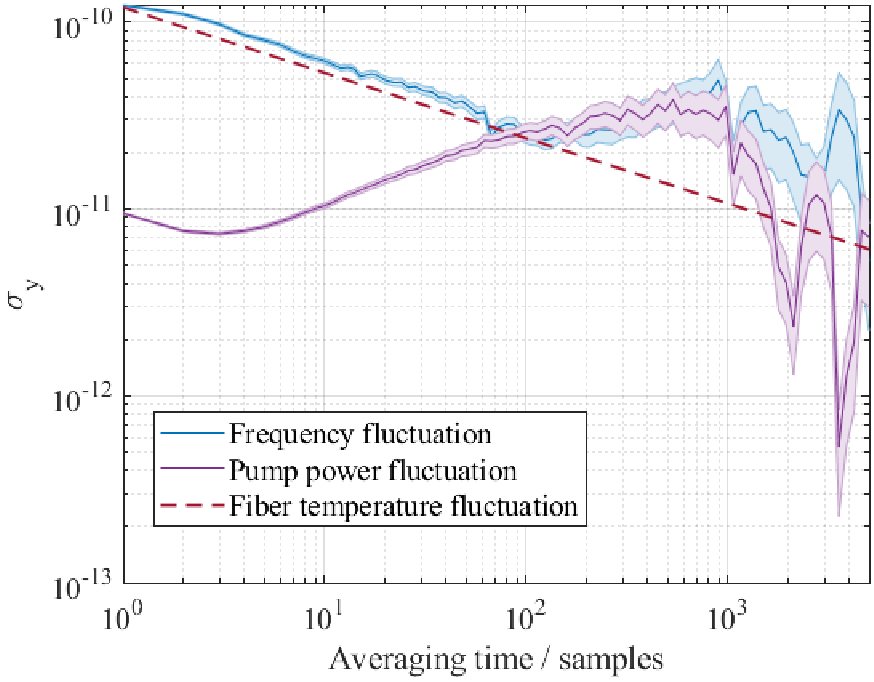

Figure 3.19: Allan deviation of the laser fractional frequency. In blue, the Allan deviation of the laser. In violet, we represent the Allan deviation of the pump power fluctuations before the fiber, converted to a frequency fluctuation using the pump power sensitivity measurement in section 3.1.3. In red, we represent the frequency fluctuation we can expect to see with the temperature controller fluctuations of the fiber, scaled using the temperature sensitivity measurement in section 3.1.1.

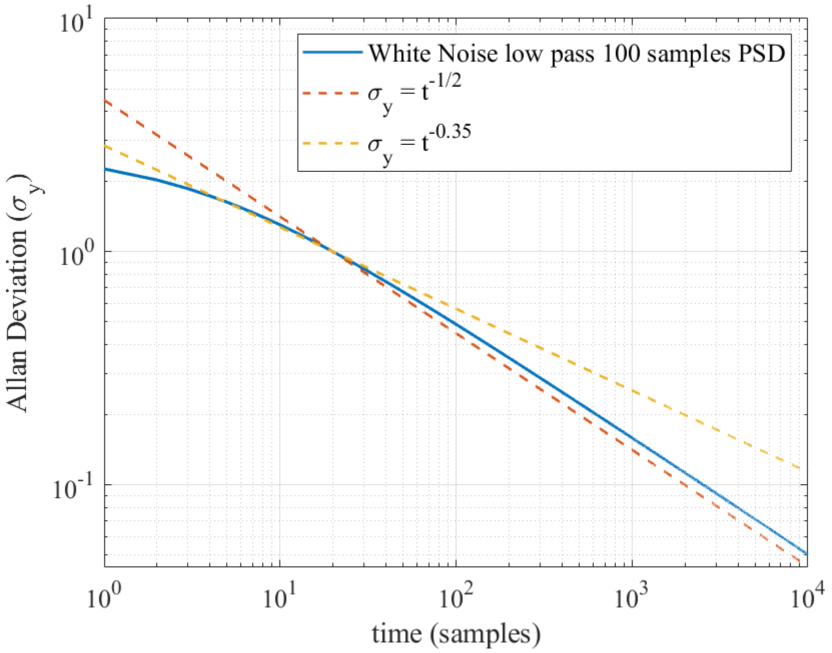

Figure 3.20: Numerical simulation of the Allan Deviation of a white noise filtered at 100 samples (blue). We also represent the $\tau^{-1/2}$ and $\tau^{-0.35}$ slopes.

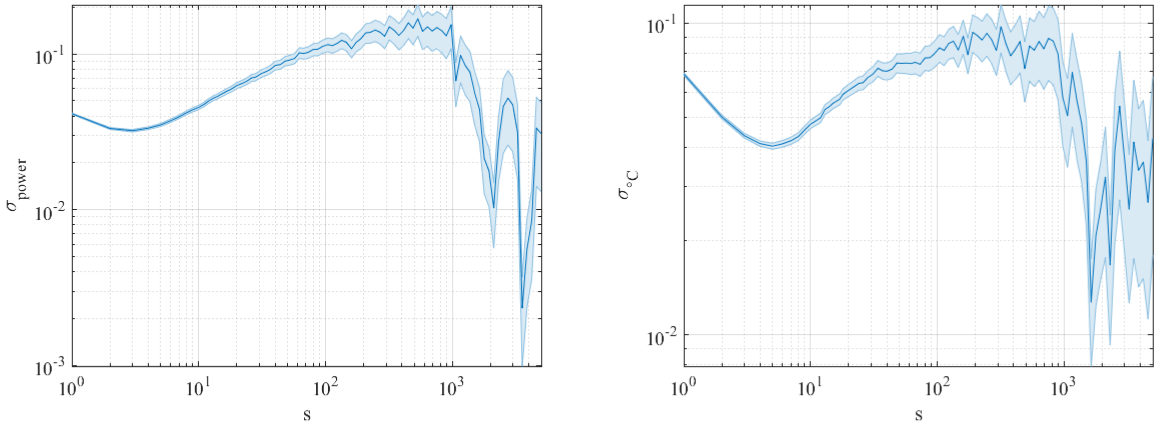

(a) (b)

Figure 3.21: (a) Allan deviation of the pump power fluctuation measured before the fibre. The vertical axis represents the deviation in mW, not normalised by the average power (∼ 60 mW). (b) Allan deviation of the ambient temperature in the experiment room. The vertical axis represents the deviation in °C. We can see similar variation for the temperature in the room than the pump beam power stability (Fig 3.21a). We can assume that the power fluctuations are caused by temperature fluctuations in the room (AC).

3.1.7 Sensitivity measurements of 3 fibers

During this project, different fibers were tested with different internal geometry and encapsulating techniques to find a good candidate for spectroscopy. A MTS signal usable for laser locking was observed in 3 fibers in total. The first fiber presented in this work is the *hybrid PMC* fiber whose design is presented in [75]. The measurement presented in the previous sections were performed on this hybrid fiber. Two other fibers were measured as well called *PMC 16* and *PMC 17*, those fibers are presented in annex A. These fibers are based on a photonic band gap technology which can reach smaller core diameter but should have a better mode content (singlemode). The measurements were performed in the same way than for the hybrid fiber, and are presented in annex B. The measurements are summed up in table 3.1.

Sensitivity	Hybrid fiber	PMC 16	PMC 17
Temperature	14 MHz.K^{-1}	13 MHz.K^{-1}	15 MHz.K^{-1}
Probe Polarization	90 kHz.deg^{-1}	10 kHz.deg^{-1}	100 kHz.deg^{-1}
Probe Power	3 kHz.mW^{-1}	/	10 kHz.mW^{-1}
Pump Power	44 kHz.mW^{-1}	80 kHz.mW^{-1}	20 kHz.mW^{-1}

Table 3.1: Sensitivities of the different fibers tested to lock the laser. Details of the measurements for PMC 16 and 17 are in Annex B.

Error signal and frequency stability

The different fibers tested in this project do not show a significant discrepancy in the sensitivity to environmental and optical fluctuations. However, the error signal and transmission of the fibers vary greatly (see annex A). The variations of transmission are mostly due to the difficulty encountered in the encapsulation which appeared to be hardly reproducible.

The PMC 16 has an error signal width of $\sim$ 50 MHz with a transmission of 10% for the probe and 8% for the pump. The PMC 17 a width of $\sim$ 25 MHz, with a transmission of 17% on the probe and 36% on the pump. And the hybrid fiber has an error signal of $\sim$ 14 MHz width with a transmission of 38% for the probe and 15% on the pump.

On Fig 3.22 the Allan deviation of the 3 different fibers are represented. The blue curve is the PMC 16, which has the highest instability and the widest error signal. We can expect this wide error signal to be a limitation in the short term stability of the fiber, as the slope of the error signal is not as sharp.

The violet curve is the PMC 17, which lays between the PMC 16 and the hybrid fiber. The MTS signal obtained with this fiber is wider than the hybrid but sharper than the PMC 16. We were expecting that the single-mode behavior of the PMC17 would have helped to reach a better stability but this was not the case.

Finally we have the hybrid fiber Allan deviation in red. As discused in section 3.1.6, we can explain most of the instability by environmental factors.

The error signal and transmission seem to not have been a limiting factor in the hybrid fiber lock, but no significant correlation with external fluctuation were observed with PMC 16 and PMC 17.

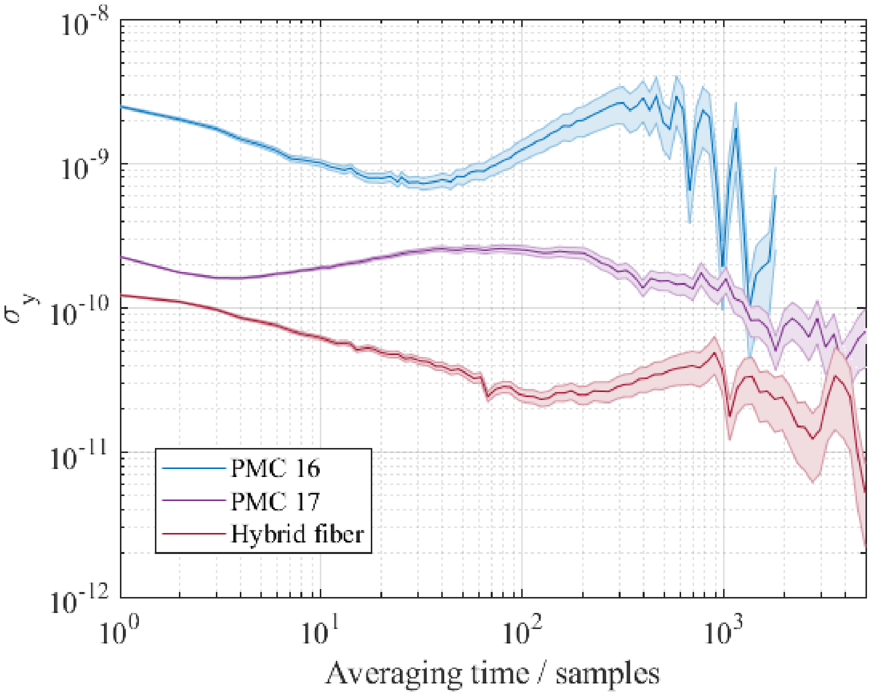

Figure 3.22: Allan deviation of the laser fractional frequency locked on different fibers.

3.2 Conclusion

In this chapter we have investigated the stability measurement of a laser locked on various hollow-core fibers, detailing the characterization of the fiber's sensitivity to external parameters such as temperature, power, and polarization. The chapter began with an overview of the experimental setup utilized for these measurements, using the same setup presented in chapter 2 to correlate external parameters with the frequency fluctuations of the locked laser.

The chapter described the fibers used in these experiments. These fibers have been built by the GPPMM team at XLim. A focus was placed on the measurement of temperature sensitivity, acknowledging its impact on frequency stability. A specialized heating platform was developed to control the fiber's temperature. This section also presented findings that showed a relationship between temperature changes and laser frequency, emphasizing the importance of precise temperature control for these fibers.

The chapter further examined the fiber's sensitivity to the incident polarization of the probe. The effects of probe and pump beam power on frequency stability were also assessed, showing that variations in beam power could significantly influence the stability of the locked laser.

Additionally, the chapter presented the sensitivity of fiber injection, measuring frequency changes as a function of injection misalignment. The fiber lock's robustness was also tested using a Zero-G platform, providing insights into the fiber lock's performance under acceleration.

The chapter concluded by integrating these sensitivity measurements into the overall stability analysis of the laser. This analysis revealed that temperature fluctuations were a significant factor in short-term stability, while power fluctuations played a more dominant role in long-term stability. The chapter's investigation into various fibers, each with different internal geometries and encapsulating techniques, offered insights into the optimization of these systems for enhanced stability and performance. It allowed to show the importance of the fibers closing to make them suitable frequency reference.

Part II

Raman Lock

Chapter 4

FPGA phase lock

FPGA is a versatile platform that allows to shape almost at will the electronic transfer function. This features was already permitted by microcontrollers and CPU platforms, but with a trade-off between reprogramability (CPUs) or possibility of integration in an embedded system (microcontrollers). FPGA offers the ability to have both, and add the possibility of a massively parallel electronic transfer function. The work carried in the team to develop acetylene based optical reference made us improve our understanding and capabilities related to rapid information processing. Thus we realised that such rapid processing and versatility could be used to lock not only the frequency but also the relative phase of two lasers.

For this purpose, we have developed and characterised a phase detection scheme based on ADC sampling and a rapid multi-integrator feedback loop.

In this chapter we present this digital phase locking FPGA-based architecture. We first remind the needs for phase coherent lasers, specifically in the context of AMO experiments and rapidly list the different feedback mechanisms used to tune the frequency and phase of a laser. We then present some techniques used to create an error signal for the phasor of a digital signal and we discuss the measurements of phase noise. In particular, we present the specifications of our experimental architecture. It uses the digital to analog conversion sampling as a phase detection principle that minimises the delay in the feedback chain, and we characterise the phase noise of our measurement and feedback method. The following chapter is dedicated to an in-depth study of the achieved performance and specifically to the comparaison of two FPGA platforms and two types of lasers.

4.1 Phase lock overview

In AMO experiment, Raman transitions are used for many applications, such as adiabatic state transfer (STIRAP [76]) [77], cooling [78] [77] or atom interferometry [79] [14] [80] where Raman transitions are used as mirrors and splitters. This type of transition requires that the two lasers are detuned in frequency but stay phase coherent over the entire length of the interferometer.

In this section we present the general principle for Raman transitions, the different methods to lock a laser, in frequency and in phase. We detail the principles of external-cavity diode lasers (ECDL), and how the laser architecture constrain the feedback loop of a phase locked loop (PLL).

4.1.1 Raman transition in AMO physics

Raman transitions are two-photon transitions used to facilitate the coherent transfer of population between energy levels of a quantum system. These transitions are of particular interest in systems where direct transitions are restricted by selection rules or when a control of the momentum state of the wavefunction is required. Other variations of Raman transition allow for adiabatic passage [76] of a cloud or part of a cloud in a desired state, often in the case of hyperfine states.

To illustrate, we present the example of the Λ-system utilizing the $5^2S_{1/2}$ and $5^2P_{3/2}$ states of Rubidium-87 (^{87}Rb), an alkali atom use to perform ultracold atom experiment in our group. We note the two lower levels $|a\rangle$ and $|c\rangle$, that we consider as ground states, while an excited state is noted by $|b\rangle$.

In this example, direct transitions between the ground states $|a\rangle$ and $|c\rangle$ are prohibited by electric dipole selection rules. Nevertheless, we can still make this transition through a two-photon process where states $|a\rangle$ and $|c\rangle$ are coupled via the third level $|b\rangle$, serving as a virtual or intermediate state. This virtual level is close enough to an atomic eigenstate to permit coupling, but sufficiently detuned to prevent one photon transfer of population.

Each laser beam is detuned by δ from either the $|a\rangle \rightarrow |b\rangle$ or the $|c\rangle \rightarrow |b\rangle$ transition. The frequency difference between the two lasers, $\Delta\omega$, is therefore equal to the energy split between the ground states $|a\rangle$ and $|c\rangle$. We consider that the ground states separation is greater than the linewidth of both laser, so each laser is interacting with only one of each ground states.

A prerequisite for Raman transitions is the establishment of coherence between the two laser beams as it is the interference of the two excitations to the intermediate state that allows transfer through the two-photon transition. The Hamiltonian of the three level system can be simplified as an effective two level system, but the relative phases of the two dipole transitions need to be constant otherwise the effective two level system cannot undergo Rabi oscillation.

As an example, using the notation given in [81] for an effective two level system representing a three level system driven by a Raman transition

$$C_f(t) = \cos\left(\frac{|\Omega_{eff}|t}{2}\right), \tag{4.1}$$

$$C_e(t) = -ie^{-i(\Delta\phi)}\sin\left(\frac{|\Omega_{eff}|t}{2}\right)e^{-i\omega_{eff}t}, \tag{4.2}$$

with Ω_{eff} the effective Rabi frequency of the system, $\hbar\omega_{eff}$ the energy splitting between the two levels and $\Delta\phi$ the phase difference between the two lasers. We can see that the phase between the two lasers need to be constant for the system to behave as an effective TLS.

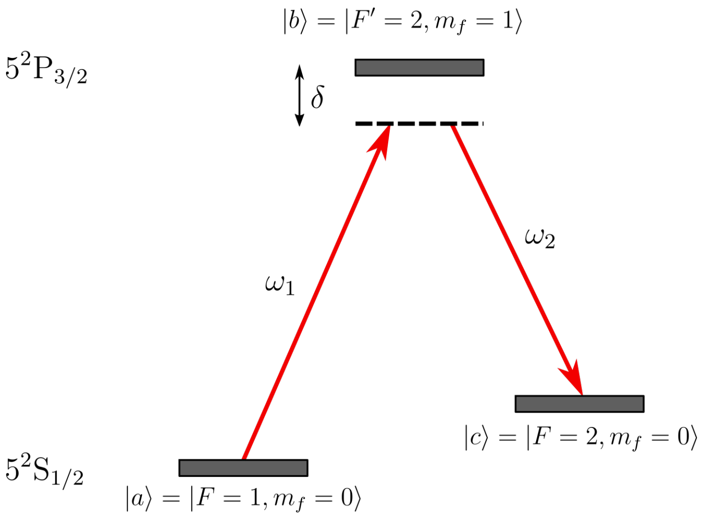

Figure 4.1: Λ-level scheme used for two-photon Raman transitions in ^{87}Rb.

4.1.2 External-cavity diode laser

In this section, we focus on describing the frequency response of external cavity diode laser (ECDL). In the case of AMO experiments the laser should be as monochromatic as possible and locked at a given frequency, that is close to an atomic transition. This is characterized by a spectrum of the laser radiation that is both narrow and stabilized on a given frequency.

Laser diodes are very accessible laser system. Their gain medium exhibits a broad emission spectrum. To narrow the output of such diode, an external cavity can be used. The general principle of the ECDL is to re-inject part of the beam in the diode, using optical elements such as mirrors or gratings [82]. Some laser diodes such as the RIO PLANNEX diode used in this work include the grating on a silicon chip guiding the light [83]. The RIO PLANNEX are fibered lasers in the telecom band with a linewidth around 10 kHz. In this work, we have also used custom-made ECDL that we describe below. It uses a partially reflective mirror instead of the grating.

Piezoelectric change of the physical length

The first possibility for tuning the frequency of such ECDL is to change the physical length of the cavity. This shifts the frequency. This is usually done in a controllable way using piezoelectric components mounted on a reflective component of the cavity. When a voltage is applied to the piezoelectric component, it contracts or expands resulting in a variation in the cavity length (see Fig 4.2).

This allows for a stabilization of the frequency that is limited in bandwidth by the speed at which the piezoelectric component can mechanically respond to the applied voltage. Depending on the size of the piezoelectric component the final bandwidth can vary, but it is usually less than a tens of kHz for typical applications. Stabilization of the frequency using piezoelectric component is therefore reserved to the compensation of long term drifts of the frequency. Using a piezoelectric component on the cavity allows tuning of the laser over one free spectral range of the cavity without mode jump [81]. For cavity of a few cm in length this corresponds to a free spectral range of a few GHz, which allow

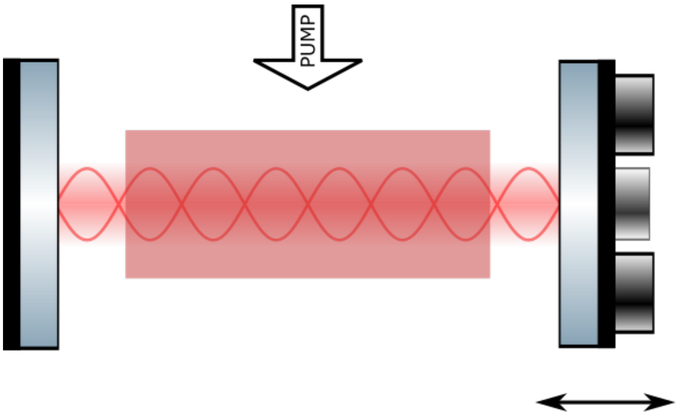

Figure 4.2: Representation of a cavity controlled by a piezoelectric component. By applying a voltage to the piezo, it is possible to control the total length of the cavity. This results in a voltage controlled tuning of the laser's frequency.

for compensation of most long term drifts.

Current control of the optical length

As piezoelectric stabilization is often too slow or impossible to install as in the case of RIO PLANNEX lasers. We use other ways to tune the laser's frequency.

In the particular case of semiconductor laser, two effects of the pump current can be used to tune the laser's frequency. Semiconductor lasers are pumped using a current to create electron-hole pairs (called exciton) in the semiconductor junction. This pair undergoes a photo-transition (through photoelectric effect) that is used as an amplification mechanism in the laser. If more current is applied in the junction, more electron-hole pairs are created. This can change the effective index of the medium seen by the light in the amplification part of the cavity, which changes the effective index of the whole cavity. As a result, the optical length of the cavity is changed, thus changing the resonating frequency. This effect is referred to as the *Carrier Density Modulation Effect* [84]. It is relevant for high frequencies (typically above a few tens of MHz) and results in modulation of hundreds of MHz per mA [85].

A second effect of the pump current is an increase in temperature of the laser diode. This causes a change in the physical length of the cavity through thermal expansion and also a change in the optical length trough a change in the thermal refractive-index coefficient [86]. This results in a shift of the resonating frequency. This effect is referred to as the *Temperature Modulation Effect* and is dominant for low frequencies (up to a few MHz) [85].

These two effects oppose each other [84], [85] which leads to a π phase shift in the feedback chain. If no special care is taken to circumvent this issue (such as a different feedback filter for high frequencies), the crossover between the temperature modulation effect and the carrier density modulation effect defines the limit of the feedback bandwidth using the current controller of the diode.

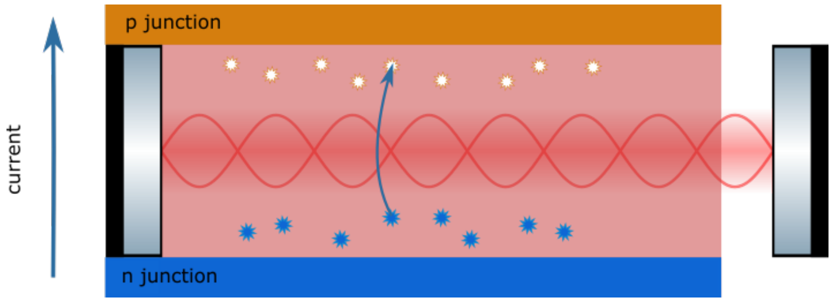

Figure 4.3: Representation of the current control of the semiconductor laser diode. By increasing the intensity of the pump, more excitons are created in the amplification medium resulting in a higher optical index. This changes the optical length of the cavity, changing the resonating frequency selected by the laser. At lower frequencies, the dominant effect is the diode's temperature change cause by the passing current.

4.1.3 EOMs in cavities, optical length

To achieve even higher bandwidth for the stabilization of frequency in a laser, an Electrooptic modulator (EOM) can be used inside the laser cavity [15].

EOM are composed of non linear crystals with an optical susceptibility tunable under application an electromagnetic field. This also can be thought of as a two-wave mixing in a non-linear media [87]. This is usually done by applying a voltage between electrodes placed around the crystal. This results in an optical component with an optical index that can be controlled by a voltage.

The usual limit of EOM components come from the electrodes that have limited bandwidth for acceptable voltage. Commercial products display bandwidth of hundreds of GHz. However, this requires the possibility to mount such EOM inside the cavities. This has not been done in the lasers used in this work, neither in the custom lasers nor in the PLANNEX ECDLs.

We emphasize that only the frequency of a laser can be tuned. Because of the memory effect of the cavity, the phase and the frequency are continuous functions. The phase control is therefore achieved via a frequency control via the derivative relation $f = \frac{1}{2\pi}\frac{d\phi}{dt}$ that introduce an extra $\frac{\pi}{2}$ phase delay in the control of the phase.

4.2 Digital PLL

Now that we have described the means to control the phase and frequency of a laser, we need to generate the error signal that will be used to lock these two parameters. In this work, we have developed a frequency counter on FPGA that is presented in the annex C.1. We will develop in this section the different techniques existing for the detection of a signal's phase.

4.2.1 Analog phase detector and DAC

The most straightforward phase detection technique for an electric signal is through the use of an analog phase detector. A fully analog phase lock is possible, however it can lack the versatility offered by the use of a digital feedback loop that can be tuned numerically, and can offer the ability to use a frequency lock then switch quickly to a phase lock to increase the capture range of the phase lock.

The analog phase detector's output can be converted numerically using a DAC. There are different designs for analog phase detectors using different principles, mixers [88], Harmonic sampling, Sample-and-hold [89]...

All these techniques require an additional component in the feedback chain, meaning a potential addition of noise, delay and cost. Another approach for digital detection is to sample the entire signal and use digital signal processing (DSP) techniques to extract the phase.

4.2.2 Signal digitization and phase reconstruction

A common DSP technique used for phase reconstruction of a signal is to compute the arctangent of the ratio of the signal's two quadratures, using for example the CORDIC algorithm or a look up table.

This technique allows for a direct reconstruction of the phase, but as this requires some amount of calculation, additional delay is added to the feedback chain, reducing the system's potential bandwidth. Furthermore, as the two quadratures are measured against one another, the bandwidth of the system is limited by the signal frequency.

4.2.3 XOR gate phase detection

Amongst other digital techniques used in digital phase detectors [90], we present here the example of the XOR phase detector (see Fig 4.4). The phase difference of two signals can be monitored by integrating the output of a XOR gate whose inputs are the two signals. While the result is straightforward for square output signals, other waveform may result in a detector output being non linear with the input phase [90].

These detectors have also an important limitation for high frequency signals, as the sampling frequency has to be significantly higher than the signal frequencies for the output to be precise.

The frequency sampling of the XOR gate detector determines the smallest detectable phase difference. When the signals are out of phase by 1°, the output will be high for 1/180th of a cycle therefore, if the signal is not sampled once during 1/180th of a cycle, the phase difference will not be picked up by the detector.

This design also as a limitation in the bandwidth of the PLL, as the output of the XOR gate needs to be filtered with a cutoff frequency lower than the signal's frequency in order to have a non oscillating output, as the output of the XOR gate as the same period as the signal for a constant phase difference.

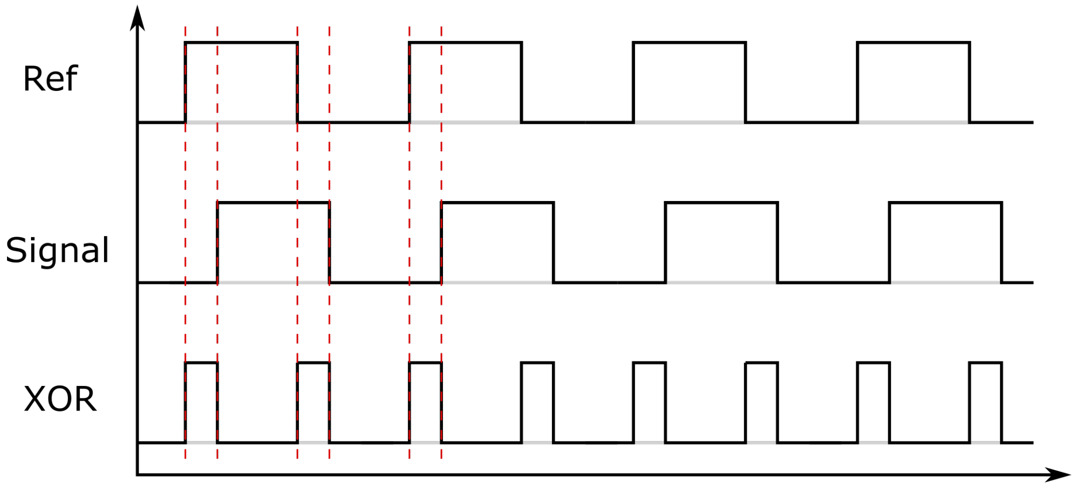

Figure 4.4: The signal is compared to a reference with a XOR gate. The resulting signal can be integrated as the output of the gate is at the high state for a proportionate duration on a full cycle. The output is constant in the high state for out of phase signals, and in the low state for in phase signal. The integrated signal can be used as an error signal on the phase difference of the two inputs of the XOR gate.

4.2.4 Under-sampling phase detection

Another method for phase measurement uses one of the sampling's limit to measure only the phase of the signal. This technique called *undersampling* or *bandpass sampling* [91] uses the ambiguity created by the sampling. When sampling a signal at a frequency $f_{sampling}$, two signals at frequencies f_{signal} and $f_{signal} \pm N * f_{sampling}$, $N \in \mathbb{N}$ yield the same results. This ambiguity in the sampled signal is called *aliasing* [92] (see Fig. 4.5).

Aliasing is often seen as an effect to be avoided in sampling. But for signals that are contained in a certain frequency band, this can be used to reconstruct the information in a signal sampled at a much lower frequency than the actual signal's frequency [91], [93] (see Fig. 4.6).

We want to overcome the sampling frequency limitation of most digital gates [90], and have the minimal amount of calculation to produce an error signal on the phase, to limit the delay in the feedback system. To achieve both of these requirements, we propose the use of a detection technique based on the synchronous downsampling of the signal [94].

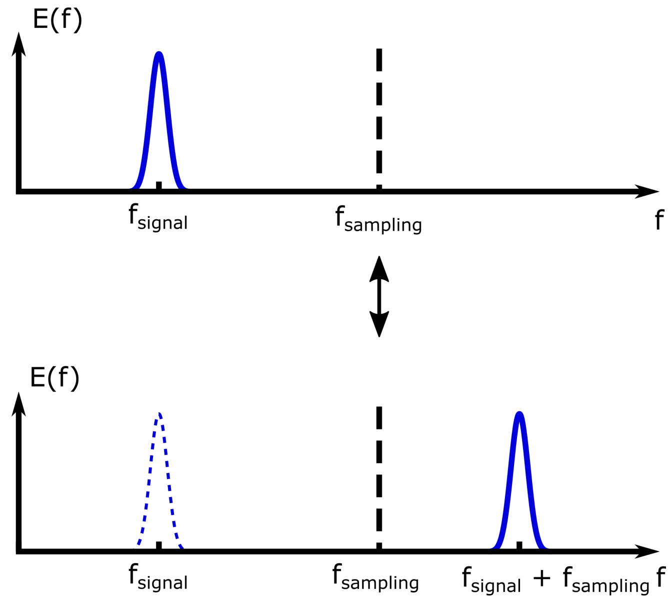

Figure 4.5: Representation of aliasing, the two spectrum represented would yield the same sampled signal when sampled at the frequency $f_{sampling}$. When reconstructing a sampled signal, the whole signal is brought down in the $0 - f_{sampling}$ region, this is called *spectral folding*.

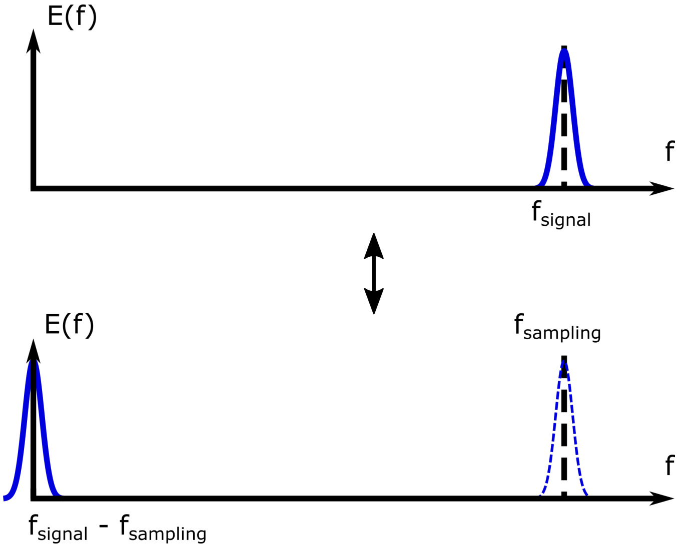

Figure 4.6: By sampling the signal exactly at the carrier frequency, we can bring down the spectrum to DC, allowing for a direct measurement of the phase of the laser's beat signal.

Taking the sampling frequency $f_{sampling}$ equal to the signal frequency f_{signal} results in a signal that is the one of the quadrature of the signal. If the signal is perfectly in phase with the sampling, the sample signal is zero. If there is a phase difference ϕ between the signal and the sampling, the sampled signal is equal to $\sin(\phi)$.

By taking a sampling frequency $f_{sampling} = 2f_{signal}$, the resulting signal is a succession of $\sin(\phi)$ and $-\sin(\phi)$. If we take the difference of two successive points, we still have a signal that is equal to $sin(\phi)$ but with any offset in the signal removed (Fig 4.7) and with a data rate doubled.

Additionally, a sampling frequency of $f_{sampling} = 4f_{signal}$ would allow a reconstruction of the amplitude of the signal with the $\cos(\phi)$ and $-\cos(\phi)$. This is the version implemented in our system, but it should be noted that the signal's frequency could be quadrupled if a need for sampling a higher frequency arises.

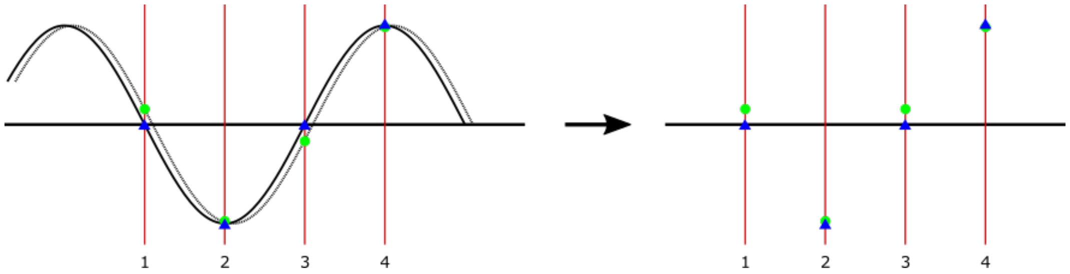

Figure 4.7: Phase detection by sampling the quadratures of the signal. We show here that by changing the sign of the data at the 3rd clock cycle, we can double the data acquisition rate.

This gives a phase detection which is dependent on the ADC clock reference, which is therefore the phase reference for the laser beatnote. We will use this undersampling base detection system for the feedback loop, as this allows for a phase detection at the highest rate possible, with the least delay generated as no data treatment is necessary after the ADC. We develop in the next section the tools used to record and characterise the phase stability of the beatnote. While the FPGA allows us to record directly the data generated as an error signal as presented in this section, we also show and compare other techniques for measuring the phase noise power density.

4.3 Phase stability measurement

In this section we present the performances of our phase detection method, developed with a FPGA architecture. We first explain the decimation technique used to make to sample the data at a lower frequencies and access the PSD of the signal at those frequencies. Then we present the different experimental setups allowing us to lock and measure the phase of the lasers.

4.3.1 Sampling frequency conversion, decimation

The PSD used to characterise the phase stability of our system has a range and frequency resolution defined respectively by the time serie resolution and length that we can acquire. The lowest frequency measured in the PSD is determined by the signal sample's total duration, and the highest frequency is determined by the Nyquist frequency of the signal sample that is half of the sampling frequency.

The DAC frequency of the RedPitaya is 125 MHz and 250 MHz for the Alpha250. The sample they produce are 14 bits in length, this result in a data rate of ~ 2 or ~ 4 Gbits per sec respectively. This means that sampling the data for long periods of time will result in massive amount of data that can't be stored in the FPGA board. To sample and store the data at a fast rate (250 MSPS), we need tu use the RAM connected to the FPGA using a technique called Direct Memory Access (DMA), where the data is prepared by the Logic part of FPGA, which also sends the right signal to the RAM, allowing it to write data in the memory directly, bypassing the CPU part (see Zynq documentation [95], or Koheron SDK [96]).

This means that the total size of the RAM will limit the duration of the sampled signal (in our case 0.01s.). This results in a limitation in lowest frequency measurable by the FPGA. To increase this total duration we can reduce the effective sampling frequency. This can be done with a technique called *decimation* or *downsampling*.

The decimation consists in not recording every point in the data, but rather only recording 1 point every N points of data. This effectively reduces the sampling frequency, allowing for longer samples to be recorded on the FPGA.

However, this reduction of the sampling frequency has a consequence on the noise measured by this detection method. The total noise power that goes in the ADC is still the same with or without decimation, so the integrated power of the PSD is still the same, but is distributed over a reduced frequency range when the decimation is used. This can be seen as the spectral folding of the noise, which results in noise above the lower sampling frequency (f_s/N) to be added up in the lower band (see Fig 4.8) [67] [97].

We emphasize that the 3 dB increase shown in Fig 4.8 is only valid for a white noise. In other words, if the noise components are at frequencies lower than (f_s/N), they should not be modified nor displaced by the decimation that still allows to resolve them well. This is for example the case of the $1/f$ noise presented in Fig 4.8

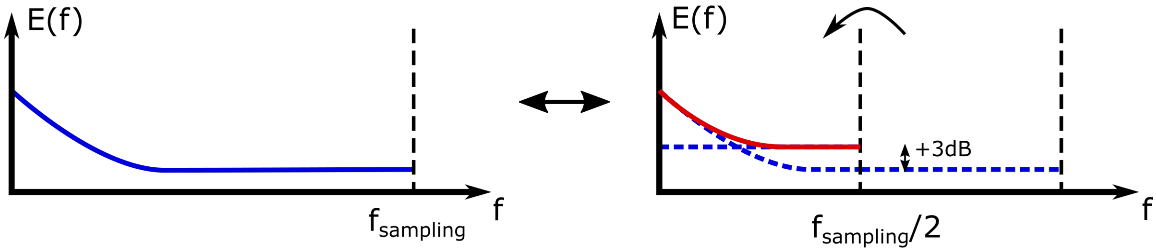

Figure 4.8: Representation of the spectral folding when the sampling frequency is decimated. As the signal at higher frequency is still detected by the ADC, it still contributes to the data. It is seen as adding to the signal in the frequency band corresponding to the new sampling frequency.

4.3.2 PSD calculations

The data in the FPGA is acquired in the form of a time series of data sampled at frequency f_s. We present here the treatment of the data to access the PSD corresponding to the time series of the laser's phase fluctuations.

First the time series values are normalised to a voltage in Volts. As the data is stored and read as a number between -2^{15} and 2^{15} corresponding to the 1 V_{pp} ADC input mapped on 16 bits of the ALPHA250 (it would be 2 V_{pp} for the Red Pitaya). So we divide the signal by 2^{16} to convert the data to Volts. We take the Fast Fourier Transform of the data using the FFT Matlab function. The normalisation of this function to get the PSD is detailed in the Matlab documentation [98]. The result is not a power spectral density but the Fourier transform of the voltage before the ADC. To get to the PSD, the voltage has to be converted in V_{RMS}, squared and converted to power by dividing by the impedance of the ADC, here 50 Ohms. We write here the detail of our treatment of the ADC data,

$$PSD_W = \frac{1}{f_s N(2 * 50\Omega)} * \left|\text{fft}(adc/2^{16})\right|^2, \tag{4.3}$$

with f_s the sampling frequency of the signal and N the number of points in the sample. The sampling frequency here is the sampling frequency of the ADC without taking the decimation into account, as the noise power contained in 1 data point is decided by the ADC sampling time and is the same regardless of the decimation.

We convert the PSD to dBm as it is the usual representation

$$PSD_{dBm} = 10\log_{10}(PSD_W). \tag{4.4}$$

The PSD is then converted to dBc by removing the carrier frequency power to the PSD. In order to do so, we separately measure the amplitude of the signal going in the ADC. We use the signal after the power splitter as in 4.12 when applicable or we can simply take the $-90°$ and $+90°$ out of phase component of the ADC data to determine the signal's amplitude.

$$PSD_{dBc} = PSD_{dBm} - PSD_{dBm}(f_c), \tag{4.5}$$

with f_c the carrier frequency.

4.3.3 PSD calculation from the time series

Once the time series are acquired in the FPGA, a treatment of the data is needed to plot the data as a PSD. The simplest estimator of the PSD is obtained by taking the Fourier transform of the autocorrelation function of the signal (also known as periodogram [99]). However, when doing so, the resulting PSD presents a lot a fluctuations for high frequencies.

This is due to the finite size of the sample, that causes a convolution with a sinc in the Fourier transform representation of the data (see [100]). This phenomenon is accentuated by the representation of the data in logarithmic scale in Fig. 4.9. In order to reduce this phenomenon and improve the readability of the PSD, different techniques can be used. The averaging of repeated measurements is a straight forward technique, however here due to the size of the data for each measurement ($>$ 200 Mo), this could not be implemented. Other techniques to smooth a periodogram have been developed (Bartlett's method [101], Welsh's method [102]) based on a windowing of the data before the Fourier transform. We have chose to implement a straightforward method proposed in [100]. We simply average the data of the periodogram using a moving average filter. This can distort the data especially at lower frequencies, but for higher frequencies, this gives a more accurate reading of the PSD. That should stay valid if the PSD stays constant over the length of the moving average filter. To avoid too much distortion at low frequencies, the moving average filter uses 20 points. As the PSD is presented in logarithmic scale, we emphasize than the logarithm of the averaged PSD is represented, so as to put more weight is on larger values than on small values who are most susceptible to perturbations [100].

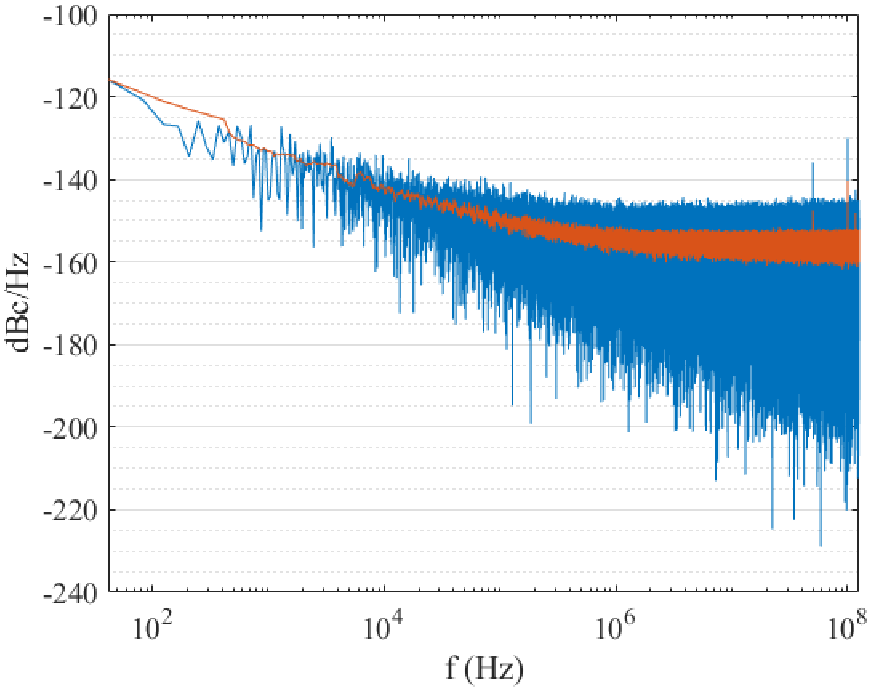

Figure 4.9: Filtering of the PSD of the ADC data with a 50 Ohm input. In blue we show the periodogram of the timeserie and in orange we show the periodogram smoothed with a 20 points moving average filter.

In the following, all the experimentally measured PSD will be represented using the treatment described above and shown in Fig 4.9.

4.4 Phase lock experimental setup

To perform two-photon Raman transitions, it is necessary to control both the frequency and phase of the two laser beams that address the atomic transitions. A frequency lock is possible using the beatnote of the laser leading to a precision of around 100 kHz, which is the linewidth of the lasers. However, we aim for even better precision to coherently transfer atoms to another state. To achieve better performance and ensure the phase coherence of the laser, the laser beatnote phase needs to be measured and locked. In order to do so, one of the laser will be considered the master laser, and the phase fluctuation of this laser will be copied on the second laser called the slave laser. This phase lock lowers the beat-note width below the Hz level and makes the frequency lock unnecessary once the phase of the laser is locked.

The Raman transition of Rubidium 87 atoms is 6.8 GHz which therefore corresponds to the frequency difference of the laser radiations we have to target for. In the experiment detailed below we have implemented two different strategies to lock the ECDL with such frequency offset. We have either down-mixed the beatnote directly from 6.8 GHz to $f_{clock}/4$ using a microwave synthesiser or divide the frequency by 8 to reach 850 MHz and then down-mix this signal to $f_{clock}/4$ using a high frequency Direct digital synthesizer (DDS) (AD9914).

The first solution is expected to reach the best performance while the second is a trade-off between performance and versatility. Indeed, the frequency division will lead to a degradation of the phase noise's PSD by $10\log(8) = 9$dB. On the other hand, using a high frequency DDS, clocked at 3.5 GHz, we take out the need for further frequency division down to $f_{clock}/4$ and can also easily control the phase and exact frequency difference which is useful to perform atom interferometry.

To realise our experiment, we have two pairs of lasers and two different boards. The first pair are custom made ECDL at 780 nm. These lasers will be the one used for Raman transition on Rubidium in the future. Their linewidths is around 100 kHz and feedback bandwidth is about 1 MHz. The second pair of laser is a pair of 1533 nm commercial RIO laser, with a smaller linewidth ($>$ 10 kHz [83]). Those lasers will be used for testing the feedback loop performances both in term of phase noise and bandwidth, as we expect them to be comparably more performant than the 780 nm ECDLs.

The two FPGA boards that have been tested for the feedback loop are the RedPitaya (STEMLabs) and the ALPHA250 (Koheron). The RedPitaya has been our initial choice motivated by its affordability and our initial knowledge of its working principle (see section 2.3). Our developpement led us to identify that the RedPitaya's high delay is a limitation for the bandwidth of the lasers. Among other commercially available platforms we decide to work with the ALPHA250 that is able to achieve higher bandwidth for the lock.

4.4.1 Experimental setup

For the 780 nm lasers, the setup is meant to be used in the future as a Raman beams generation on a AMO experiment. Therefore the setup is an independent bench that we will connect to the experimental setup through optical fibers. The architecture of the optical bench is presented in Fig 4.10. We only focus on the *Relative Lock* part, that will be used to lock the phase of the slave laser to the master laser.

For the 1533 nm lasers (the same than presented in section 2.1), a different approach is used. The goal with these laser is to get the best performances of the phase lock with no intent to use them as Raman lasers. The optical setup is minimal, with only isolators to protect the lasers and a beam combiner to generate the beatnote on a fibered photodiode (PD100B Koheron). The architecture of the lock system is kept as minimal as possible, while exploiting at its most the FPGA board performances (see Fig 4.12).

We chose the beat-note to be at a quarter of the ADC sampling frequency (see section 4.2.4). This allows us to limit the electronic components required to lock those laser,

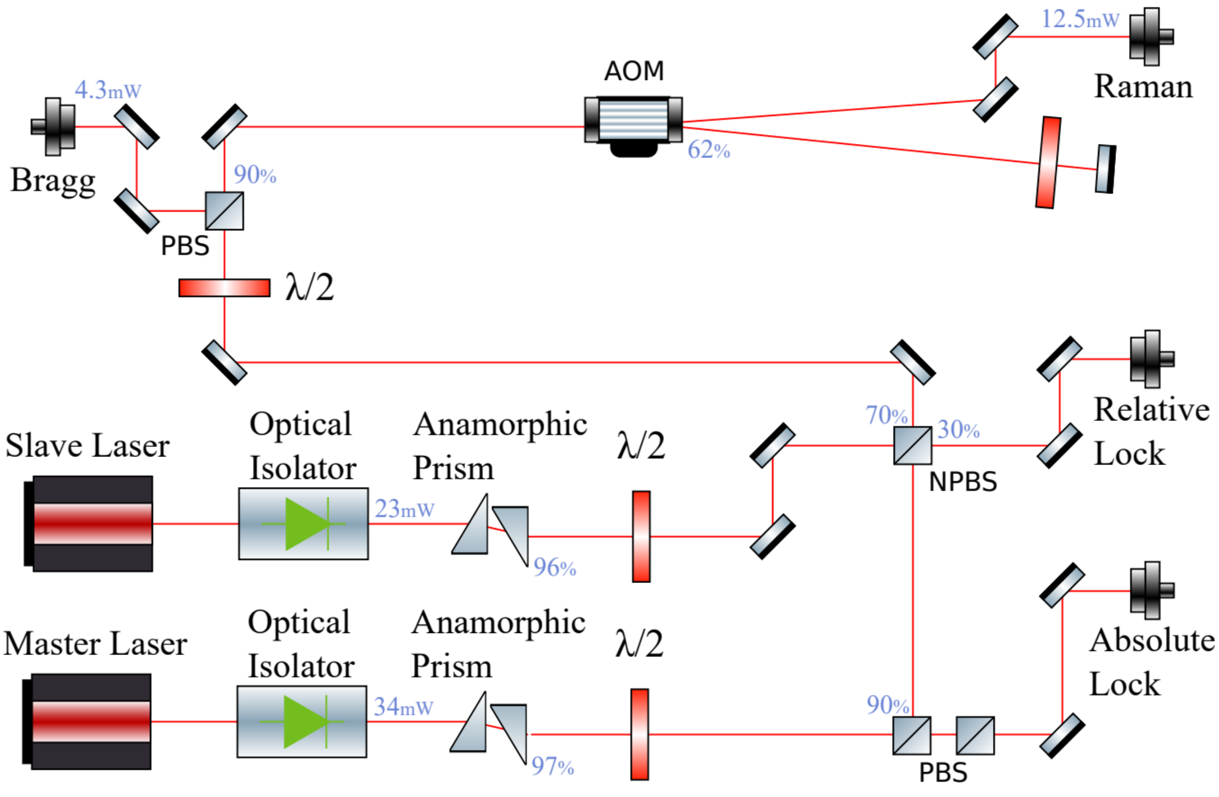

Figure 4.10: Optical bench for the 780 nm Raman lasers.

both to limit potential sources of noise and to reduce the total delay in the feedback loop. We thus expect the best performances in this setup, allowing us to test the limit of the detection and locking technique.

The power is then split (ZMSC-2-1W+) between a monitoring / measurement chain, with either a spectrum analyser for precise measurements or an oscilloscope to check if the signal is locked. The other half of the power is recorded by the ADC of the FPGA. Attenuation of the optical power in front of the photodiode ensures that the ADC is used in the maximum range without any saturation.

To characterize the phase noise PSD, we also used another half of the signal and down shift it to DC using an analog mixer before sampling it on a different ADC of the FPGA board. To generate the frequency of the local oscillator used in the downmixing, we used a signal generated by a DAC of the FPGA board. This ensures the phase coherence of the downmixing process. It additionnaly allows to suppress the FPGA clock noise that becomes common noise on the two ports of the mixer. For the measurement we also tested a signal generator (Rigol 4162) clocked to the frequency reference of the FPGA.

The FPGA board and the spectrum analyser are both clocked by an external frequency reference, which is the OXCO presented in section 2.1.2. Clocking the FPGA board to the reference is important as it is the FPGA's clock that sets the ADC clock which in turns is used as a reference for the phase lock. This is because we are using the undersampling technique presented in section 4.2.4. The FPGA board's ADC's clock is the frequency reference and phase for the phase lock.

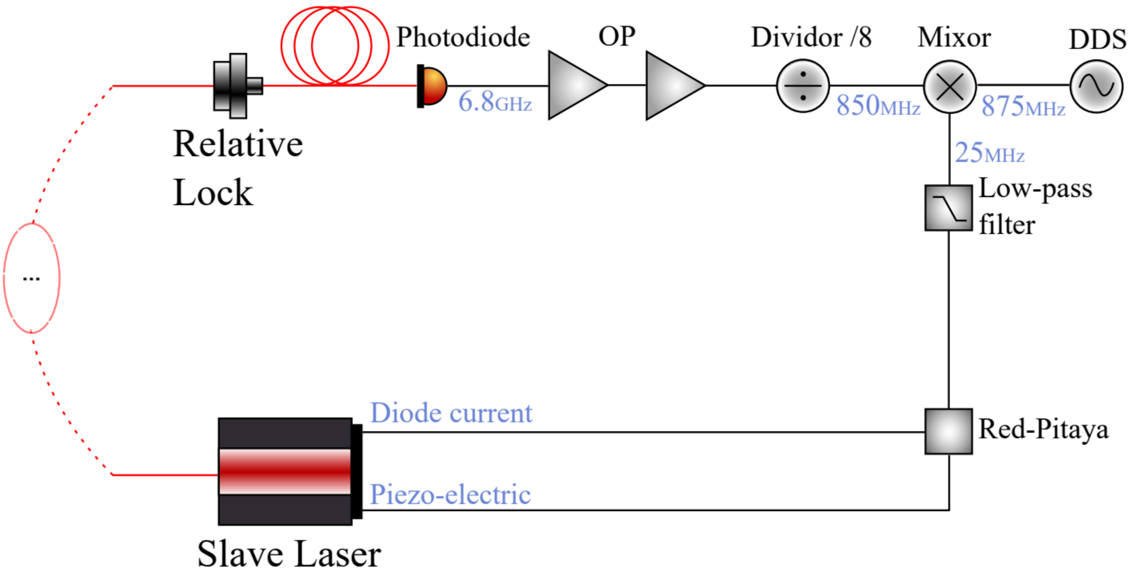

Figure 4.11: Phase lock setup for 780 nm Raman lasers. As the beatnote is at a frequency too high for the FPGA's ADC, a microwave divider is used to bring the beat-note at 850 MHz. This signal is then downmixed with a DDS locked in phase with the reference. It is also possible to generate a frequency near 6.8 GHz and downmix the beat-note directly with a microwave synthesiser to a frequency fitted for the FPGA's ADC, suppressing the need for a divider. Note that the downmixed frequency of 25 MHz represented here is adapted for the Red Pitaya, but a downmixing to 62.5 MHz would be required for the ALPHA250.

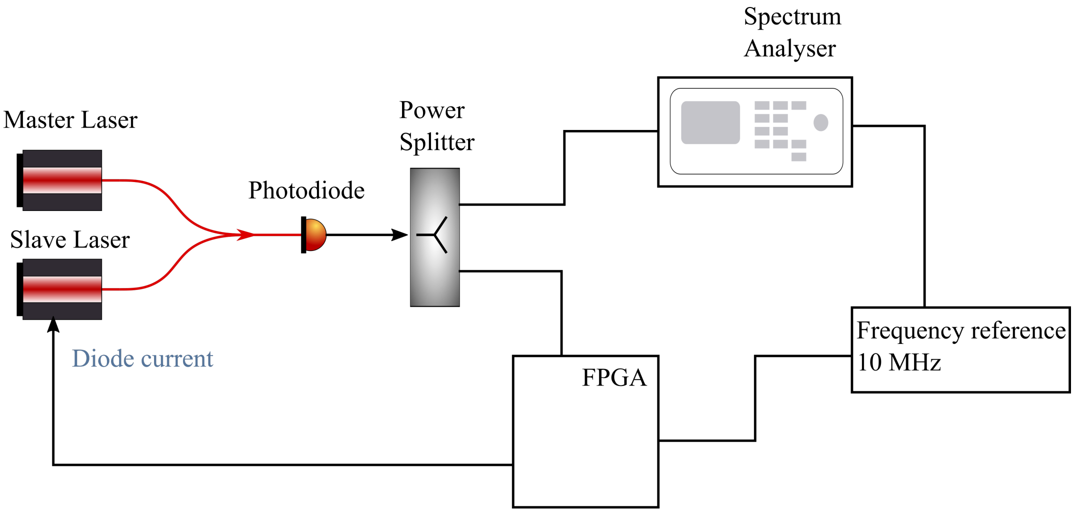

Figure 4.12: Phase lock setup for the RIO diodes. The laser are balanced in power and combined on a photodiode. The phase detection and the PID is done entirely in the FPGA, and the second half of the power can be analysed with a spectrum analyser.

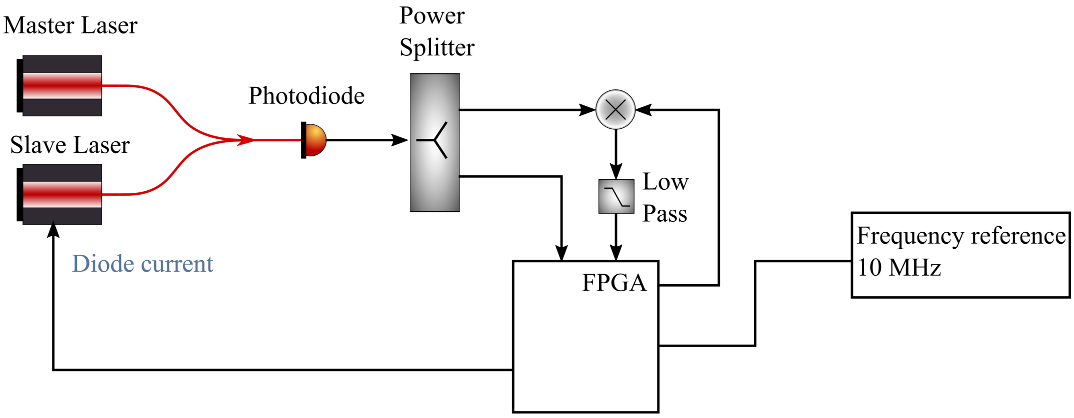

Figure 4.13: Phase lock setup for the RIO diodes. The spectrum analyser can be replaced by the FPGA board, using a second ADC. Two configurations are possible: either generating a signal at the beat frequency with a DAC to down-mix it and recording it on a second ADC, either it is also possible to record the beat signal directly from the error signal in the FPGA.

4.4.2 Mixer and DAC vs direct error signal

To characterise the phase stability of the lasers, we need to measure the phase noise of their beat-note. We have detailed in section 4.4.1 two different configurations for each measurement. As shown in Fig 4.13, we can either record the error signal which we can access in the FPGA, or mix the beat-signal with an out-of-phase reference signal at the same frequency. In Fig 4.14 we compare the PSD of the signal measured with the mixer (blue) and the error signal technique (orange). This lock and measurements where carried using the ALPHA250 and the 1533 nm lasers.

We first notice that the two curves are quite similar even though the error signal unexpectedly gives a PSD that is a few dB higher. The normalisation of the error signal PSD is done using the 2nd and 4th digitalized points that give access to the amplitude of the beatnote while the 1st and 3rd points give access to the phase.

The result shown differs at higher frequencies as a low-pass filter is used for the mixer technique, and at very low frequencies as the error signal is convergent to zero by design, as opposed to the mixer technique which can present some low frequency noise [65].

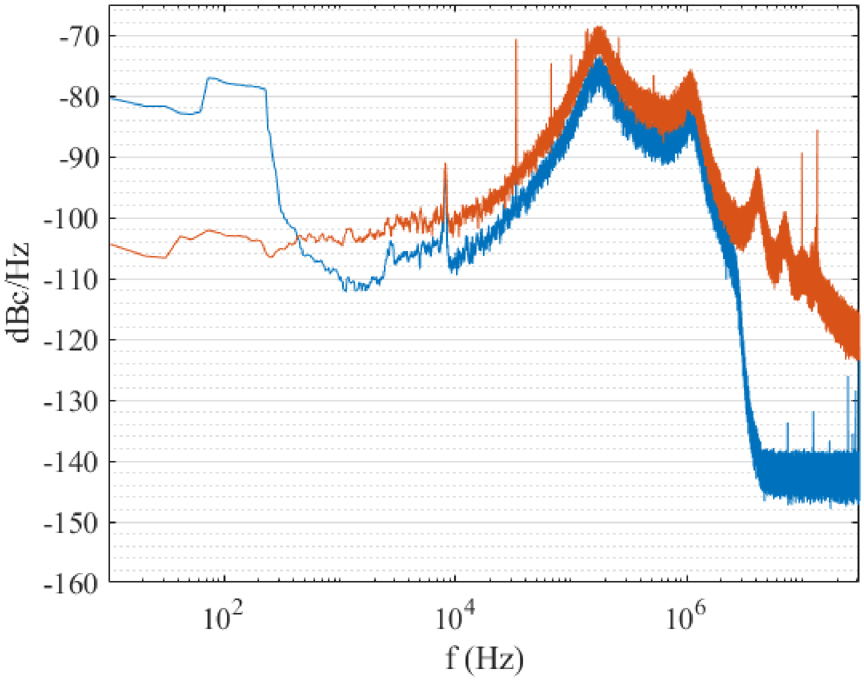

Figure 4.14: Difference between the mixer technique and the error signal recording. In blue, the PSD of the laser beatnote measured with a mixer as in Fig 4.13. In orange the PSD obtained by using the data on the ADC of the feedback loop chain as in Fig 4.12.

In the mixer technique, we can see that for low frequency the noise is considerably higher the measurement, this is due to the fact that the signal generated by the Rigol DG4102 is not perfectly in phase with the clock of the FPGA. We can also see on the measurement a drop in power at 1.9 MHz, which is expected as a low pass filter at this frequency is used to remove the overtone component after the mixer.

The mixer technique is normalized by changing the phase of the reference signal by 90°. This also allows to access the amplitude of the carrier which is then used to normalize the PSD.

On the signal recorded directly inside the ALPHA250, the error signal is convergent to zero by design of the PID so the power does not diverge for low frequencies. It should even be convergent towards zero for a perfect system but additional noise is present which limits the phase stability at long timescales. We could not determine the origin of this additional noise. For both measurement, a decimation of 4 has been used so the effective sampling frequency is 31.25 MHz.

Another difference we can see is the floor level of the noise at ~ 1 kHz of ~ 10 dB. This can be explained by the presence of the filter, as with the filter, no noise enters the ADC in the frequency band 2 - 250 MHz which is the total bandwidth of the ADCs [96].

So in the case without a filter, we sample a noise, at around ~ 125 dBc/Hz at 31.25 MHz while the noise is in fact present in the whole 250 MHz band. This causes some aliasing of the noise [97], meaning that the 125 dBc/Hz noise over 250 MHz is folded back on the 0 - 31.25 MHz band. This result in a noise floor expected at ~ -115 dBc/Hz $(= 10\log_{10}(\frac{250}{31.25}10^{-12.5}))$. This can explain the resulting discrepancy between the two measurement techniques.

4.4.3 Floor level of the ADC detection

Whatever the measurement technique chosen, the ADC's noise will limit the phase stability that can be measured using the FPGA. We show here the lower limit of our detection scheme. We see that this is enough to characterise the noise of our lasers, and we also confirm that our measurement is consistent with the expected ADC performances.

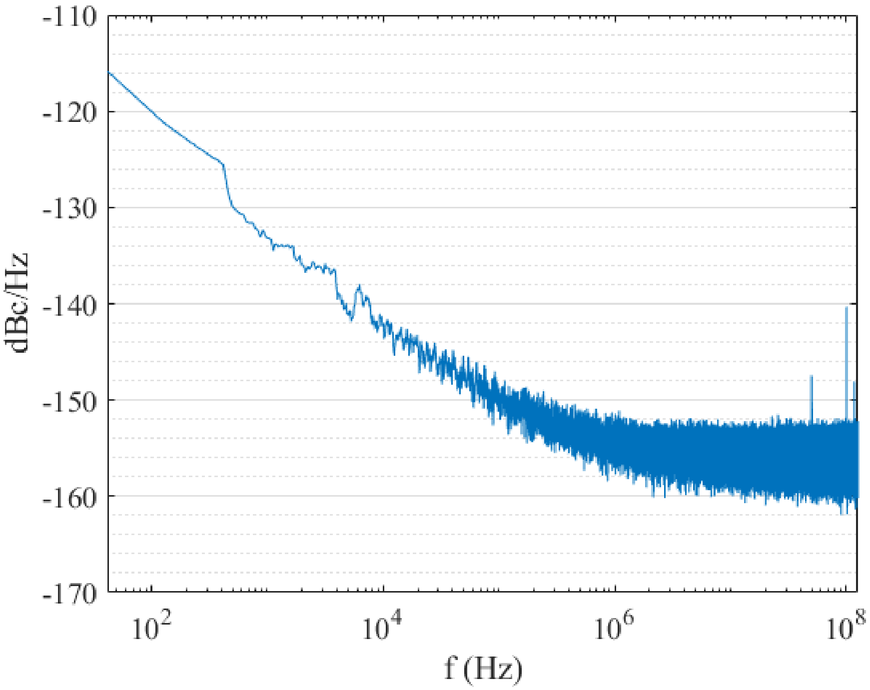

Figure 4.15: Measurement of the phase detection noise floor. This places a minimum on the measurable PSD by the board.

The measured PSD of the ADC is given with a floor at ~ -157 dBc/Hz by the constructor of the Alpha250 FPGA board [96]. It should be noted that the carrier considered here is a pure sinusoid of $1V_{pp}$ corresponding to the full scale of the ADC. We measure the same through our system when the laser beatnote is replaced with a 50 Ω connector (see Fig 4.15). It also should be noted that this floor PSD is consistent with an effective number of bits (ENOB) of ~ 11.8. This ENOB was also measured for a RedPitaya with an improved clock in [67]. This similarity is unsurprising as the ADC of the Redpitaya (LTC2145-14) and of the ALPHA250 (LTC2157-14) are presented with the same noise levels by the constructor.

This measurement floor for the PSD is enough to measure the stability of our phase locked loop in all the frequency range we are interested in [10 Hz - 10 MHz]. This allows for a very compact system that can lock and measure the performance of Raman laser using only a FPGA. We will show in the next chapter datas acquired using this system to compare different lasers once locked.

4.5 Conclusion

This chapter explored the various methods and techniques for controlling the optical length and phase stability of semiconductor lasers. We presented the details of semiconductor laser tuning, highlighting how the pump current influences the laser's frequency through the Carrier Density Modulation Effect and the Temperature Modulation Effect, and their respective impacts on high and low-frequency regimes. The integration of EOMs within laser cavities was discussed, offering perspectives into the pursuit of higher bandwidth for stabilization. The chapter further detailed digital phase-locked loops systems, including different phase detection methods like signal digitization, XOR gate phase detection, and undersampling phase detection, each with its implications on system performance.

We then discussed phase stability measurement, where the role of sampling frequency conversion and decimation in characterizing phase stability was highlighted. Our experimental setups for phase lock were presented. The chapter presented our experimental findings, comparing various phase noise measurement techniques and analyzing the limitations imposed by the ADC's noise floor on phase stability.

Chapter 5

Digital feedback and phase noise measurement

In the previous chapter, we introduced the implementation of an OPLL with our FPGA based architecture. This chapter details this integration, focusing on the feedback loop, and the performances we can obtain with such architecture.

We will first describe the loop's structure used to lock both the frequency and the phase of the lasers. We then detail the gains implemented within the FPGA, and how they are related to the FPGA's clock frequency.

We will also detail how the phase delay induced by the FPGA detection and feedback affects the locked signal. We show a measurement of the phase delay for both FPGA boards, explaining its link to the bandwidth of the OPLL.

An experimental scan of the loop gain within the FPGA is then presented, providing information on the loop behaviour and on the different effects of each component of the PID. This scan allows us to find a set of parameters suitable for the best performances in phase stability.

Finally, we will present the results achieved in terms of phase stability close to the carrier frequency.

5.1 Transfer function of DPLL

We have seen in previous section how to generate an error signal on the phase difference for the two lasers and detailed the overall electronic architecture. To get the best performance for locking the lasers, we now need to optimize the feedback loop on the lasers. We detail in this section the FPGA based feedback architecture and the different gains used to minimize the lock's phase noise, and get the best possible bandwidth.

5.1.1 Description of the feedback loop

We describe here the feedback loop used to stabilise the laser's beatnote. The block diagram of the system is presented in Fig 5.1.

The 1533 laser drivers (+ ECDLs) are described in section 2.1, we remind here the gain of the modulation ports used to control the laser's frequency (2.2 MHz.V^{-1} and 11 MHz.V^{-1} on the two ports). The laser are combined and attenuated to yield a 1Vpp beatsignal on a photodiode (PB100 Koheron).

The signal is then digitalised by the ADC. The data in the FPGA is used in two ways. The first way uses the entire signal, and feeds to a frequency counter module (see section C.1), that gives an output proportional to the input frequency. The output is fed to a PI module that gives a frequency feedback signal.

On the second path, the data is sampled using the undersampling technique (see section 4.2.4) and fed to a PII^{2}D module allowing to lock the phase of the lasers.

The frequency and phase feedback signals are summed and fed to a DAC embedded on the FPGA board. This allows to first lock the frequency of the laser and once the frequency is locked, to switch to the phaselock, that is much faster but with a narrower capture range. The output of the DAC is then fed to the laser drivers. We emphasize that the feedback is on the frequency of the lasers and not directly on the phase. In the loop, we have an extra ideal integrator, the effective transfer function for the phase is therefore $I\ I^2\ I^3\ P$.

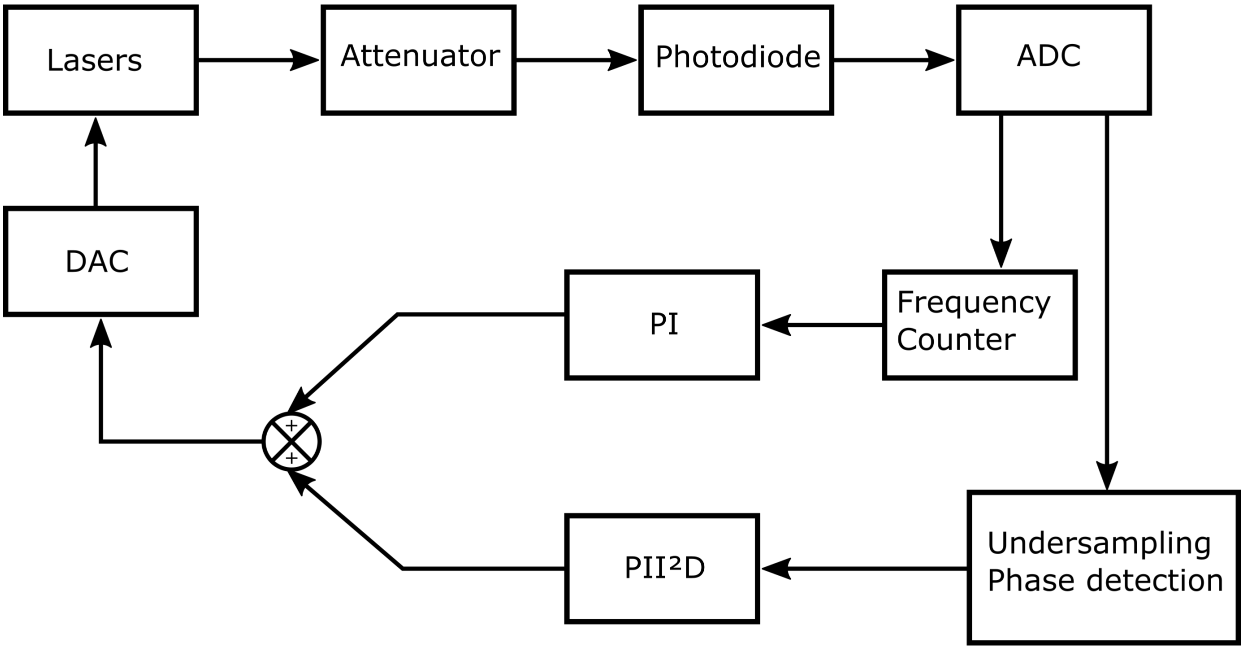

Figure 5.1: Block Diagram of the transfer function of the loop, the PID gains are set numerically in the FPGA, allowing to turn on or off the phase and/or frequency lock.

5.1.2 Calculation of the gain inside FPGA

As presented in the previous subsection, the feedback is done in the FPGA with numerical PID modules. The gain of those modules can be changed numerically, allowing to tune the PID easily, and turn on and off the phase or frequency lock as needed.

A particularity of the numerical gain is that it is dependent on the clock frequency of the FPGA. We remind here the transfer function of a PID in time domain

$$u(t) = K\big(e(t) + f_i \int_0^t e(\tau)d\tau + \frac{1}{f_d}\frac{de(t)}{dt}\big). \tag{5.1}$$

With e the error signal, u the PID output, K the general gain and f_i, f_d the unity gain frequency of the integrator and the derivator respectively.

For a sampled signal, we have then

$$u(n) = K_p e(n) + K_i \sum_{k=0}^{n} e(k) + K_d(e(n) - e(n-1)), \tag{5.2}$$

with $K_p = K$, $K_i = KTf_i$ and $K_d = \frac{K}{f_d T}$. The time is discretised with $t = nT$, and the discretisation time $T = \frac{1}{f_{clk}}$ is defined by the clock frequency of the PID module. The integrator and derivator gains are therefore defined relatively to the sampling frequency as

$$K_i = \frac{Kf_i}{f_{clk}}, \text{and } K_d = \frac{Kf_{clk}}{f_d}. \tag{5.3}$$

The clock frequency of the FPGA (f_{clk}) has an influence on the feedback loop gains. In our case, this frequency is fixed and defined by the sampling frequency of the signal ($4f_{sampling} = f_{clk}$).

To lock the phase of the laser, one starts with the frequency lock, in order to get signal in the capture range of the phase lock. Once this is done, the phase lock will naturally stabilise the frequency.

It should be noted that we have described the feedback loop with the frequency as the signal and not the phase. Indeed we control the injection current of the diode which sets the laser frequency. The feedback voltage out of the PID drives the frequency and not the phase. The phase lock feedback is achieved by an ideal integration of the PII^{2}D module described in Fig 5.1. This ideal integrator of unity gain frequency of 1 Hz when looking at the phase as a variable.

5.2 Phase delay calculation

We have described in the previous section the gain part of the loop which makes use of the gain margin available in the system. Another important parameter in the feedback loop is the phase margin. We develop in this section the link between the phase margin, the delay and the final bandwidth of the laser lock. We show that by reducing the delay of the feedback loop, we were able to achieve a bandwidth of $\sim$ 2 MHz for the Raman lock.

5.2.1 Impact of phase delay

Phase delay and bandwidth

The total phase of the feedback loop is key in determining the bandwidth of the system. The phase margin is defined as π plus the total amount of phase the error signal can accumulate in the feedback chain. When the phase margin is positive, this means that the feedback will improve stability whatever the gain, however, when the phase margin is negative, increasing the feedback gain leads to instability in the system [103].

For a system with phase delay (i.e non instantaneous feedback), the phase margin is decreasing with frequency. There, a system with lag between the error signal and the feedback point will necessarily be limited in *bandwidth* as the feedback becomes negative (or out-of-phase) for high frequencies. We can note that for even higher frequencies, the feedback becomes positive again, and then negative etc. This can be observed for example in Fig 5.2 where we observe an increase in the phase noise at approximately 1 MHz, 4 MHz and 7 MHz. The 1 MHz bump includes all phase margin contributions among which the delay. Every 3 MHz corresponds to approximately 330 ns $= \frac{1}{3\ \text{MHz}}$. This delay is partially explained by the delay 90 ns latency of the ALPHA250 $+ 14 * \frac{1}{250\ \text{MHz}} = 56$ ns required for the 14 clock cycles from detection to the PID output. This ~ 150 ns delay covers only half the phase margin of the system, and the rest of the system, from the laser driver to the photodiode induces some additional delay which likely results in a total 330 ns delay in the entire loop.

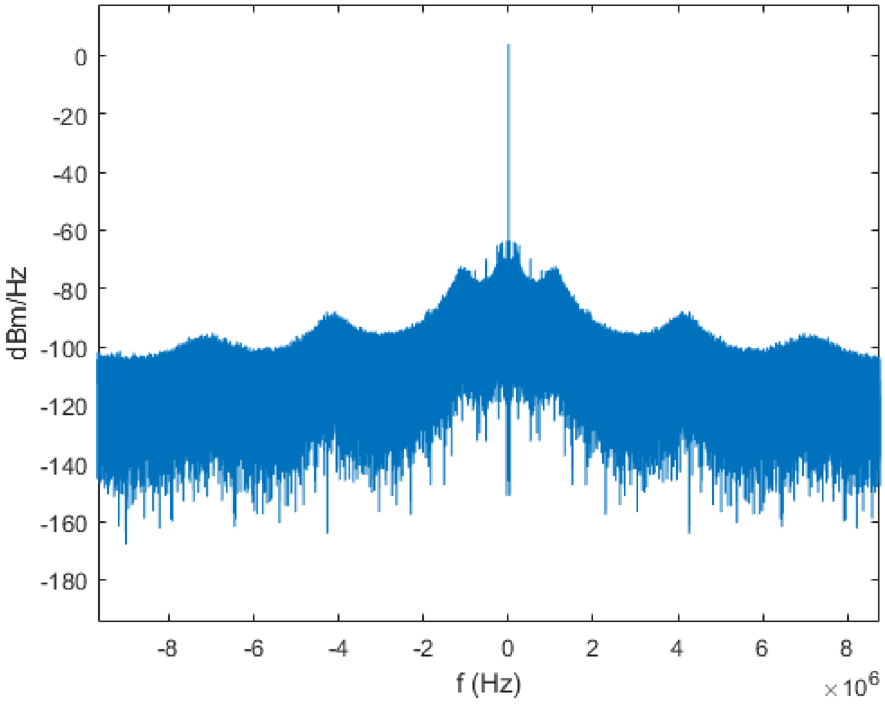

Figure 5.2: Example of the double sided spectrum of the beat note of two lasers at 1533 nm measured with the ALPHA250. We can see that at higher frequencies, out of the locking range, the region where the feedback changes sign are visible as bumps when the feedback is negative, and holes when the feedback is positive.

Phase and amplitude noise

When measuring the PSD of the laser using down-mixing with the FPGA, one has to carefully adjust the phase of the local oscillator to account for all phase delays of the beat signal. As discussed in Fig 4.7 we can access the phase noise of a signal by recording the ADC data every two points.

If the acquisition is synchronised and the phase well optimized with respect to the beat signal, the measured signal is pure phase noise, as the amplitude of the signal is zero on average. However, if there is a phase shift between the measurement chain and the lock chain, the measured signal can contain some amplitude noise which can degrade the estimated PSD. One can see this effect in Fig 5.3 where we observe an excess of 10 dB added amplitude noise in the range 10 Hz to 10 kHz which was obtained for a phase offset of 15°. This corresponds to $\sin^2(15°) = 6.7\%$ of the total amplitude noise. The amplitude noise is therefore 11.7 dB higher, corresponding to ~ -100 dBc/Hz. This amount of amplitude noise is higher than the intrinsic amplitude noise of the laser [83]. It actually comes from the feedback loop that is optimized to reduce the phase PSD and therefore increase the amplitude PSD that are conjugate variables.

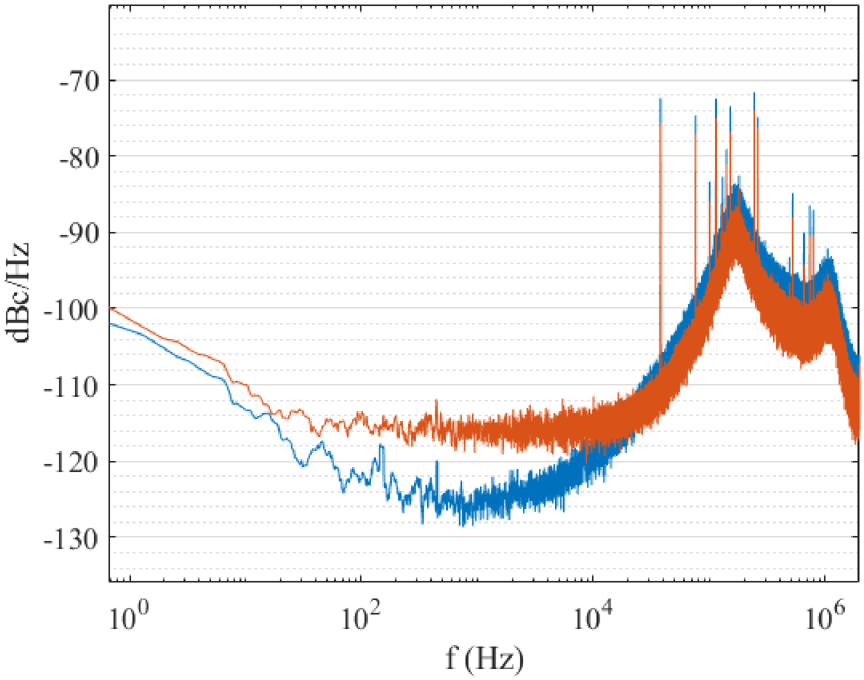

Figure 5.3: PSD of the beat signal obtained by the mixer technique. (blue) PSD with an optimisation of the down-mixing signal phase. (orange) PSD of the signal down-mixed with a 15° out of phase signal. We can see that some additional noise is visible on the spectrum as amplitude noise is mixed with the measured phase signal.

5.2.2 Redpitaya vs Alpha250 latency

We saw in the previous section that the delay in a system is responsible for instability at high frequencies. We therefore need to limit the total amount of delay in the feedback chain. The main source of delay for us is the FPGA board. From sampling of the signal to generation of feedback signal through the DACs, the board induce some latency. We measure and present in this section the latency of the two boards used in this experiment.

To measure, the latency, a frequency is fed to the ADC, and the FPGA is programmed to copy the input to the DAC output. No calculation is performed by the FPGA so the delay shown here is the minimum delay of the board.

We see that the RedPitaya as a delay of $\sim$ 220 ns and the Alpha250 delay is $\sim$ 90 ns as measured on Fig 5.4 and 5.5. This is congruent with the improvement in locking bandwidth we saw using the Alpha250.

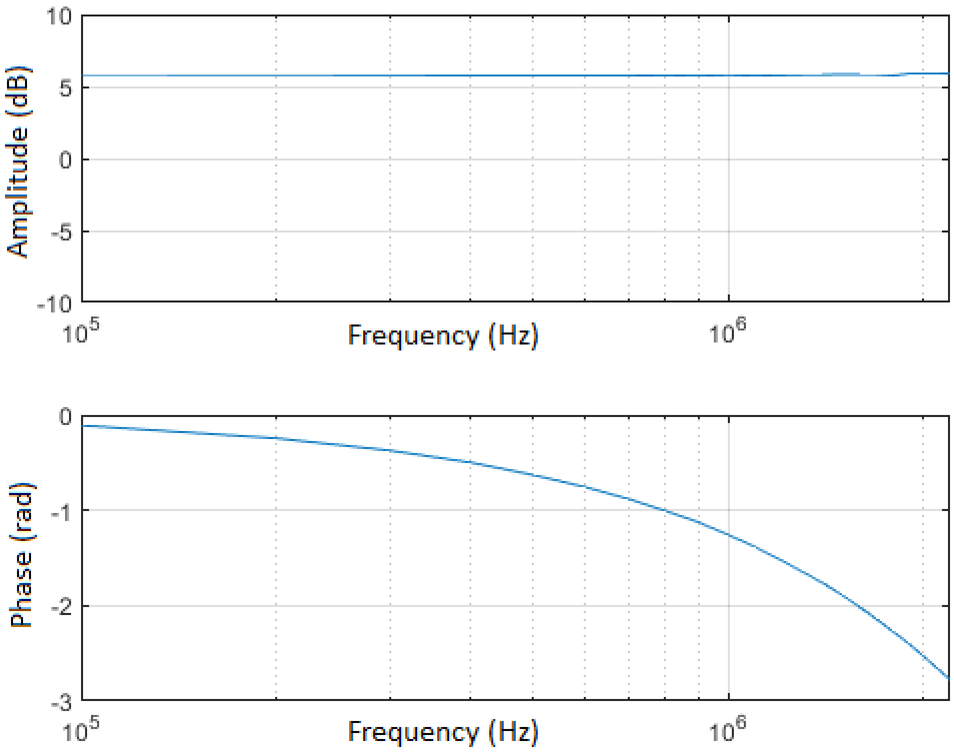

Figure 5.4: Bode Diagram of the RedPitaya. The FPGA is configured to copy the ADC data to the DAC, so we only see a pure delay behaviour, with a constant gain and a phase delay linear with the frequency.

We show a comparison of the lock of the ECDL laser with the RedPitaya and the Alpha250 in Fig 5.6. We can see an increase in the bandwidth of the phaselock, by changing the FPGA board to a faster one. The bandwidth is indeed around 700 kHz for the Red Pitaya while it is increased up to 1.2 MHz with the ALPHA250.

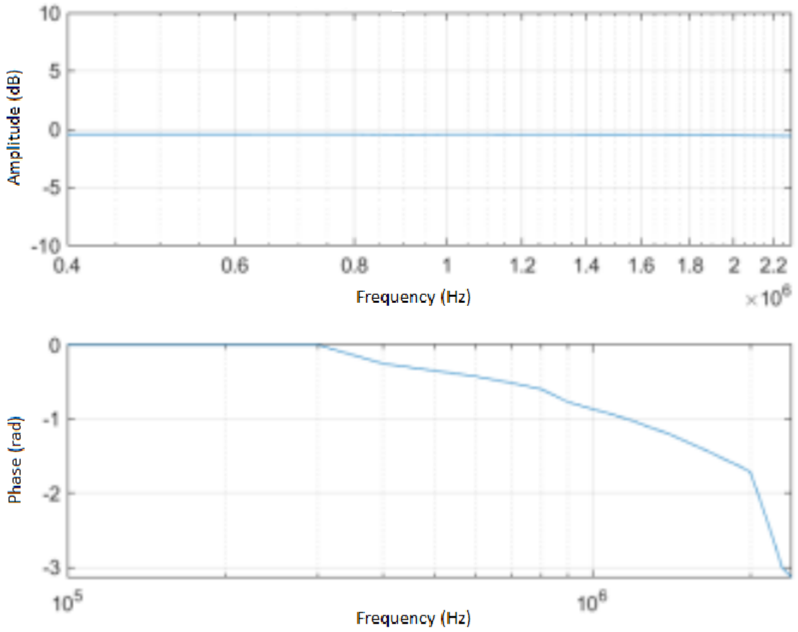

Figure 5.5: Bode Diagram of the Alpha250. The FPGA is configured in the same way than the RedPitaya, the jagged aspect of the diagram is due to the lower amount of points taken.

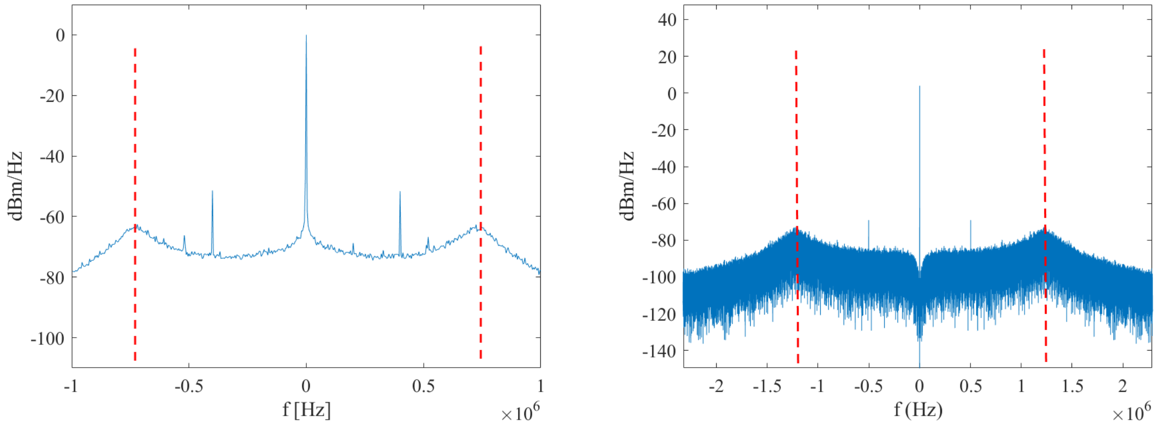

(a) (b)

Figure 5.6: Comparison of the phaselocked 780 nm ECDL spectra. (a) is the spectrum locked with the RedPitaya, measured with a spectrum analyser. (b) is locked with the Alpha250 and measured by recording the data in the FPGA. One can see the increase in bandwidth of the lock when using the Alpha250 that has a lower delay.

5.2.3 Phaselock using a feedback on the frequency

As stated in previous sections, the phase margin dictates the bandwidth of the lock and we saw that delay in the loop is detrimental to the phase margin. In our experiment, we are also at a disadvantage regarding the bandwidth as we are using a feedback on the frequency to lock the phase.

As the frequency is the derivative of the phase, it is as if the feedback signal passes through a pure integrator before being fed to the laser. The transfer function of a pure integrator exhibits a phase shift of $\pi/2$ at every frequencies, as the integral of a cosine is a sin, and $\cos(x + \pi/2) = \sin(x)$.

The phase margin will therefore be critical in our system as we don't use a feedback technique on the phase (i.e EOM in cavity).

5.3 PID scan

We measure in this section the influence of the PID gain on the lock spectra. The different PID gains were optimized to minimize the PSD noise in the band [100 Hz - 10 kHz].

On Fig 5.7, we represent the PSD of the beatnote for different parameters of the lock. The lasers used are the 1533 nm lasers and the lock is done using the ALPHA250. The gains are represented as the unit gain frequency for the integrator and the derivative.

One can see that increasing the proportional gain (Fig 5.7b) leads to an important gain in stability in the 10^2 - 10^5 Hz region. One can see that the proportional gain is predominant in this region and lead to a noise plateau if it is not high enough. One can see that the first peak (at $\sim$ 150 kHz) is reduced as the proportional is increased, this is an indication that the proportional gain channel still act within the phase margin of the lock. One can see also that on the second peak around 1 MHz, the increase of the proportional leads to an increase in the peak intensity so the proportional must be outside the phase margin in this region of the spectrum.

Increasing the integrator gain (Fig 5.7c) is important for increasing the bandwidth and the stability in the lowers region of the PSD ($\sim$ 1 kHz). As the unit gain frequency is higher, the stability is overall improved. One can nevertheless see that increasing this gain leads to an increase in the noise peak at the limit of the bandwidth ($\sim$ 150 kHz). This is an indication that the first peak is due to the phase of the integrator being responsible for the crossing of the phase margin.

For the derivative (Fig 5.7d) gain, we could not vary it much without breaking the system stability. Nevertheless, one can see an increase in the derivative gain as an effect on the first peak maximum height.

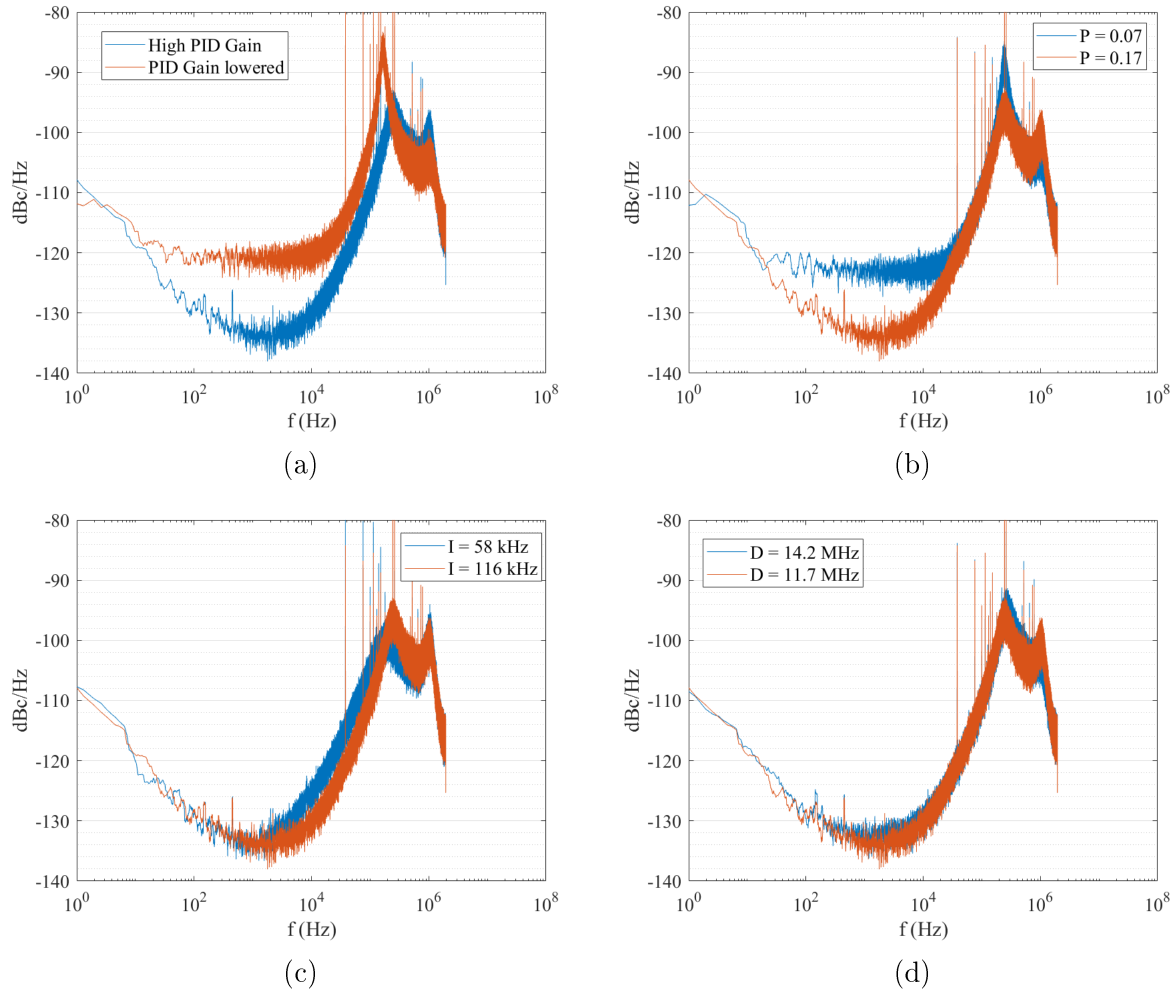

(a) (b) (c) (d)

Figure 5.7: (a) Spectra of the phaselock with different parameters. In blue, the highest gain are used before the lock oscillates (P = 0.17, I = 116 kHz, D = 11.7 MHz). In orange, the gain has been reduced (P = 0.07, I = 58 kHz, D = 14.2 MHz). For figures (b), (c) and (d) the gains used are the maximum gain unless specified otherwise. (b) In blue P = 0.07, in orange P = 0.17. (c) In blue I = 58 kHz, in orange I = 116 kHz. (d) In blue D = 14.2 MHz, in orange D = 11.7 MHz. Here I and D are the unit gain frequencies for the integrator and the derivative.

5.4 Characterisation of the performance

5.4.1 Results

Effect of the latency and of the frequency divider on the PSD

Using the above mentioned methods, we can apply them and analyse the locking performance achieved for two sets of lasers and two different FPGA boards.

We first present on Fig 5.8 the comparison of the locking FPGA board. Using the 780nm lasers, we lock the lasers using the RedPitaya and compare the lock to the Alpha250 using comparable gain parameters. The lock on the Redpitaya is performed using a /8 frequency division and a 875 MHz downmixing, while the lock with the Alpha250 is performed by locking the 2 lasers at a frequency difference of 62.5 MHz. We expect this to cause the PSD of the Redpitaya locked laser to be 9 dB higher ($10\log_{10}(8)$) due to the loss of precision in the error signal compared to the locked beatnote. We also expect an increase in lock bandwidth as the Alpha250 exhibits a lower latency than the RedPitaya (see section 5.2.2). The result is presented in Fig 5.8. These data were not taken for optimal gain parameters, as when we were using the Red Pitaya we could only optimize the lock using a spectrum analyser. The instrument allowing to record long series of data was only developed for the ALPHA250. Unfortunately these data are the only one we have that are trustfully comparable but they clearly show the increase of the phase noise when using a frequency division.

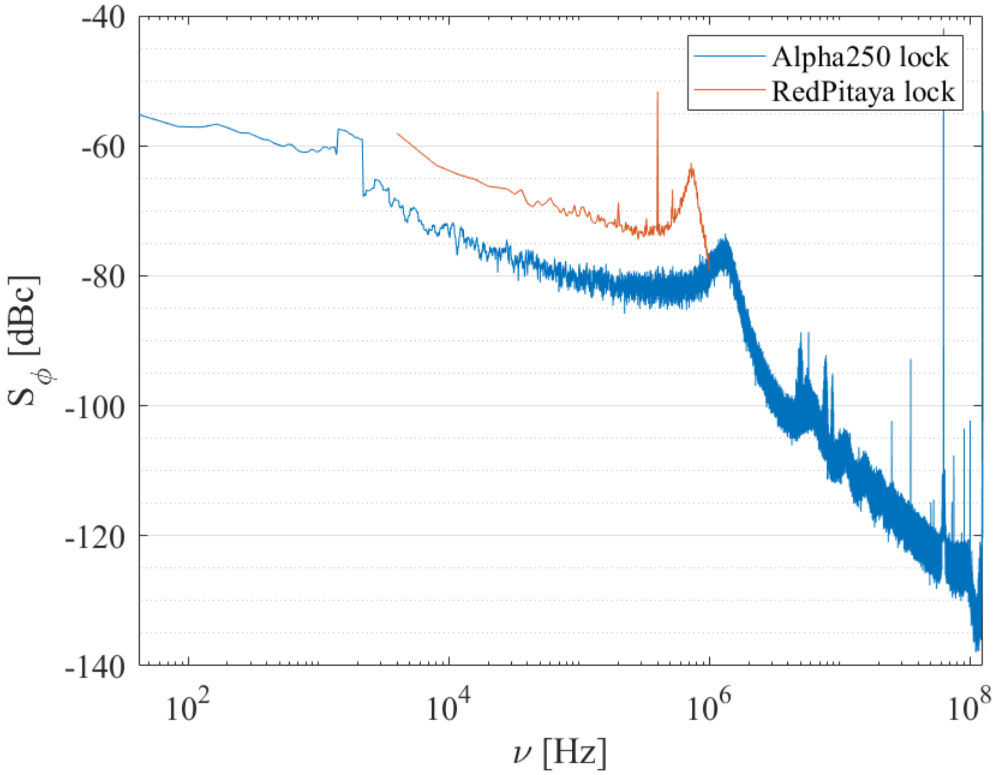

Figure 5.8: PSD of the locked 780 nm lasers. In blue the lock is realised with the ALPHA250, in orange with the RedPitaya with similar PID gains. The RedPitaya lock has a 8 times frequency divider which the ALPHA250 lock does not have. The lock parameters are $\{K_p = 0.15,\ f_I =\sim 4$ kHz, $f_D =\sim 12$ MHz$\}$ for the RedPitaya lock and $\{K_p = 0.29,\ f_I =\sim 2$ kHz, $f_D =\sim 3.5$ MHz$\}$ for the Alpha250 lock. We can see that the that the bandwidth of the laser lock is increased by using the Alpha250 as expected by the reduced delay.

The measure range for the RedPitaya is shorter than the Alpha250, as the spectrum was measured with a spectrum analyzer.

Best spectrum for noise reduction in low frequency region

We have looked at the higher frequency region and their evolution with the lock system. We will look now at the low frequency region of the PSD to find the lowest noise achievable with our system.

We are using the 1533 nm laser with a beatnote at 62.5 MHz. We are using the Alpha250 FPGA board. The PSD is obtained by downmixing the lasers' beatnote with a 62.5 MHz signal generated with a DAC on the board.

We present in Fig 5.9 the spectrum obtain after optimization of the lock.

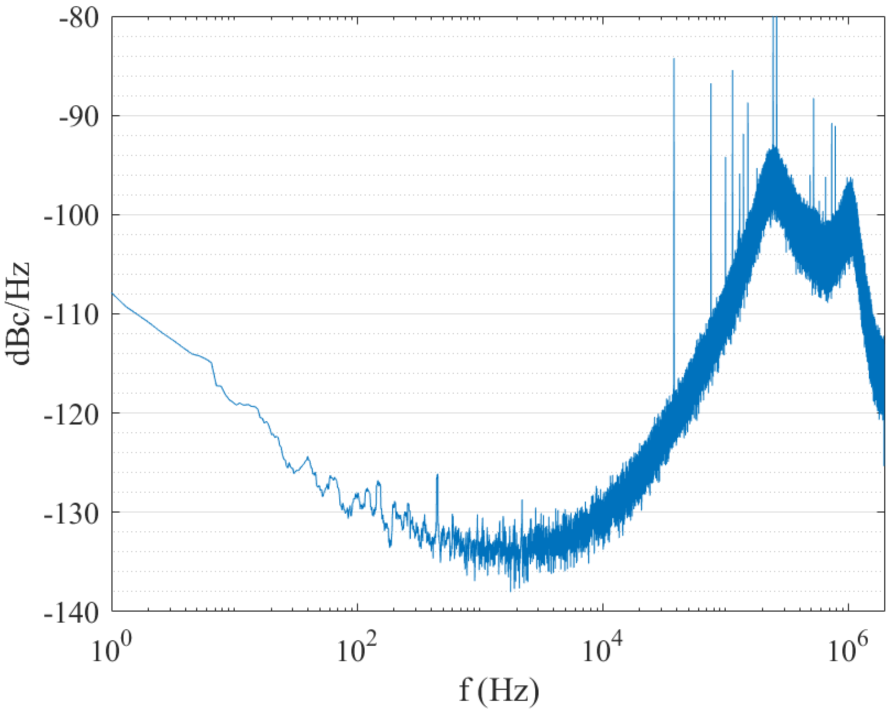

Figure 5.9: PSD of the 1533 nm laser locked with the Alpha250. The parameters used are chosen to get the minimum noise level in the kHz region.

We can see that a low noise phase lock can be achieved with this FPGA based architecture. However, here we used a beatnote between the laser at only 62.5 MHz. Raman laser used for Rb experiments are typically at 6.8 GHz. This means that the use of either a microwave source for downmixing or a frequency divider is necessary to bring the beatnote down to 62.5 MHz. As we have shown, depending on the technique used, this can lead to an increase in the phase noise spectrum.

Nevertheless we see that the OPLL implemented within a FPGA architecture displays lightweight and straightforward approach to create Raman beams using a pair of lasers that can be controlled by a voltage. In the most minimal approach where phase noise performance is not the most critical, the design can be kept simple and inexpensive. By using a digital PID, it is possible to tune the PLL with the experiments needs, whether it is a high lock bandwidth to allow for fast chirps in the Raman detuning, or whether a very low phase noise is needed over a long period of time.

5.5 Conclusion

In this chapter we have proposed a PLL design that leverages the flexibility of FPGA control to implement a dual lock system, allowing to lock both frequency and phase. The utilization of these locks in sequential operation provides a broader capture range, thus improving robustness of the system and making the locking of the laser easier. The initial frequency locking allows to bring the laser's beatnote in the phase lock range even with a frequency difference of a few tens of MHz, while the phase locking allows for a synchronisation to a more precise level. This sequential locking procedure underscores the potential for greater system stability facilitated by the FPGA-based OPLL design. It should be noted that using a FPGA board with many outputs connected to different input ports of the laser controller (such as a piezo control and a current control) can allow to haves a wide capture range without any trade-off on the precision of the phase lock.

Furthermore, the reconfigurability of the FPGA can allow for complex locking sequences and transfer function that would be beneficial for AMO experiment, such as feed-forward loops for fast phase leaps [104], or complex modulation patterns of the laser's phase superimposed on the phase lock like single sideband modulation [105].

In terms of hardware considerations, the FPGA-centric design offers compactness and power efficiency to the system. This is of particular interest for embedded applications.

Reduced latency is another advantage of this design. By using a reduced amount of components and using a fast phase detection technique, the phase delay of the overall loop has been minimised to allow for the widest lock bandwidth possible. Using an intra-cavity EOM would be an important improvement for the bandwidth of the system, as it would allow for a direct control of the laser's phase. However, implementing this solution is expensive and complex. It should be reserved to application where the phase noise and bandwidth of the Raman beams is critical.

To conclude, the FPGA-based OPLL design presents a versatile and tunable solution for phase noise reduction in paired lasers used for Raman beam generation. The implementation of this design is easily replicable as it is very straightforward to replicate an FPGA design on commercially available FPGA boards, allowing for a reduced complexity in coherent control of AMO experiments.

General Conclusion

Conclusion

This manuscript presents a study of the spectroscopy of a molecular gas, acetylene, and the method used to obtain and use the spectroscopic data. The goal was to stabilise the frequency of a laser to levels allowing atomic cooling using a fibered frequency reference.

In this work we first studied the modulation transfer spectroscopy (MTS) technique as a tool for obtaining an error signal from spectroscopy. Analytical and numerical analyses were conducted, to provide a comprehensive study of this technique. And observe the effect of the modulation parameters on the error signal one can expect with this technique.

We also covered the different mechanisms that can broaden the transition of acetylene trapped in fibered cells such as hollow core photonic crystal fibers (HC-PCF), and how the parameters of these cells contribute to those broadening mechanisms. Moreover, this work illustrates how these fiber parameters can influence the frequency stability that is linked to the error signal width, providing insights for future developments aimed at enhancing these frequency references.

Notably, we have introduced and discussed our methodologies for characterising the frequency stability of the laser locked with the error signal obtained with MTS. The Allan deviation was presented and insight for the interpretation of these figures was given. The frequency comb was presented as a significant instrument for transmitting a microwave frequency reference in the optical domain, and a reference free space cell was also developed to replace the damaged comb.

This work is centered around the development and optimisation of an experimental setup to lock a laser on the acetylene spectroscopy. The experimental setup was adjusted to measure the impact of environmental fluctuations on the frequency fluctuations. In this study, we have performed an experimental optimization of the MTS error signal to achieve the best spectroscopy possible with our HC-PCF fibers

Our results display the frequency stability of a laser locked on three different HC-PCF fibers. We were able to use the hybrid fiber to lock the frequency of a laser down to $\sim 1\ 10^{-10}$at 1s which is about 20 kHz, far below our targeted $\sim$ 200 kHz required for atom manipulation.

A second fiber, the *PMC 17*, was successfully used too as a frequency reference to lock the laser with a stability of $\sim 2.2\ 10^{-10}$at 1s which is about 40 kHz. Again, this is within our target for AMO experiments.

The third fiber in this study the *PMC 16* showed more instabilities, with a lock reaching $\sim 2.5\ 10^{-9}$at 1s. This corresponds to a $\sim$ 480 kHz frequency stability, which is close to the target we set. While the performances for this fiber are not as good as the two other fibers, it could potentially be used for atomic manipulation.

This work serves as part of the studies in the development of fibered frequency standards and shows encouraging result for atomic cooling with a fully fibered laser system. We have been able to achieve, with two different fibers, a frequency stability on part with laser systems that are uses for state of the art AMO experiment.

However, we have also shown that the sensitivity to environmental conditions, specifically temperature, can be detrimental to the performance of these fibers. This means that additional care would need to be taken when integrating these fibers in an embedded system. Furthermore, the fabrication of these fibers is a critical process. It is difficult to close and connect these fibers to regular single mode fibers. This causes some loss of transmission which means that more optical power is required for the spectroscopy, and this can be a critical point for embedded systems. The closing process also makes the fabrication of these fibers difficult to reproduce and tailor to ones needs. Nevertheless, we showed that it was possible to lock a laser on one of the fiber's spectroscopy in 0g to 2g acceleration cycles. This is promising for potential embedded application, in particular in the context of space applications.

In the subsequent part of this thesis, a development was made of an optical phase locked loop (OPLL) based on a FPGA architecture. This architecture offers a lightweight and straightforward approach to generate Raman beams using a pair of lasers. The design employs a digital PID that can be tuned to adapt to various experimental needs. It enables a high lock bandwidth for fast chirps in the Raman detuning and ensures very low phase noise over long experimental times.

We presented the context for Raman transitions used in AMO experiment in the case of Rubidium atoms, and we detailed the different ways to control the frequency of a laser's output, with a focus on the ECDL design.

Then the different digital phase detection programs one can implement in a FPGA were detailed, and we focused on the undersampling phase detection, a technique that allows us to reference the phase of our laser to the clock of the ADC used to detect the beatnote. We showed how this simple detection scheme allows for a reduced amount of internal calculation by the FPGA. This reveals useful to minimize the latency of the PLL and maximize the bandwidth of our system.

We have then detailed the method that we can use to characterise the phase stability of the locked lasers. We showed how to deduce the power spectral density (PSD) from our measurements of time series of phase points. We also displayed the minimal phase noise measurable by our system which is based on the ADC of the FPGA board, $-156\text{dBc.Hz}^{-}1$. This limitation is due to the ADC precision of the FPGA board.

The different experimental benches and setups used to measure and lock the phase of our two pair of lasers were detailed and compared in order to optimize the PSD that we could achieve.

We further detailed the transfer function of the PLL inside the FPGA, with a focus on the latency of the different FPGA boards we used, as it is critical for the total bandwidth of the system. We also detail why some care must be taken when measuring the phase noise of a laser beat-note so as to not imprint the amplitude noise on the phase noise reading.

Lastly, an experimental scan of the loop gain inside the FPGA was conducted to find the best parameters and achieve the lowest phase noise. A noise floor of -135 dBc/Hz could be reach after optimization of the gains. While this result is a noise peak at ~ 150 kHz, this can be very useful for applications requiring long coherence time of the laser.

It was also possible to show experimental confirmation that the latency of the FPGA board used can impact the bandwidth of the lock. With a lock on the 780 nm ECDL starting from 700 kHz with the RedPitaya, to a ~ 1.2 MHz bandwidth using the ALPHA250 board. This wide bandwidth can be used for applications where fast shift of the Raman beams frequency are needed.

Perspectives

The development of fibered frequency reference is a key enabling technology for embedded metrology applications, ranging from telecommunication, navigation, measurement of the earth or remote sensing. While we have been able to display frequency stability that allows for atomic manipulation, we did require some free space elements to get the best out of the hollow-core fibers. In the future, technological developments could massively improve the fiber performances for spectroscopy and metrology. Hollow core fibers offer a strong confinement of light that can be beneficial to irradiate samples with high light intensities with little optical power, and it could be a platform of interest for embedded applications or AMO experiments in space conditions.

The FPGA's reconfigurability opens possibilities for intricate locking sequences and transfer functions that could benefit AMO experiments. This versatility allows for feed-forward loops for quick phase leaps or complex modulation patterns superimposed on the phase lock, such as single sideband modulation [105]. The implementation of such FPGA design could allows fine manipulation of cold atoms with the Raman beams created by the locked lasers.

Part III

ANNEXES

Appendix A

PMC 16 and PMC 17

We present here the structural details of PMC 16 and PMC 17. Both fibers are photonic microcells produced by the XLim. They consist in a standard 7-cells photonic band gap fiber (PBG), with one side spliced to a single mode fiber (SMF). The PBG is then filled with acetylene gas via the other end placed in a vaccum chamber. A endcap is prepared consisting of a SMF spliced to a borosilicate capilary (A). After the filling of the PBG with acetylene, a few P_{atm} of helium is added to the PBG, to allow for manipulation of the open fiber without contamination. The open end of the PBG is placed in the capillary and is sealed with UV glue (B). The helium then escapes the fiber through porosity of the glass after a few hours.

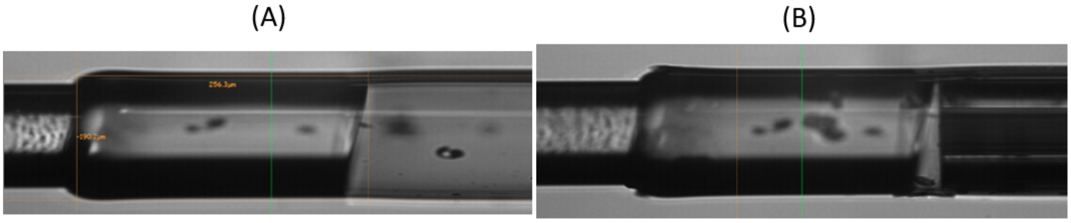

Figure A.1: Presentation of the endcap of the PMC fibers.

A.1 PMC 16

Length	~ 3.8 m
Total transmission	12 %
SAS FWHM	~ 35 MHz ±5 MHz
SAS contrast	5%

Table A.1: Parameters of the PMC 16 measured by XLim.

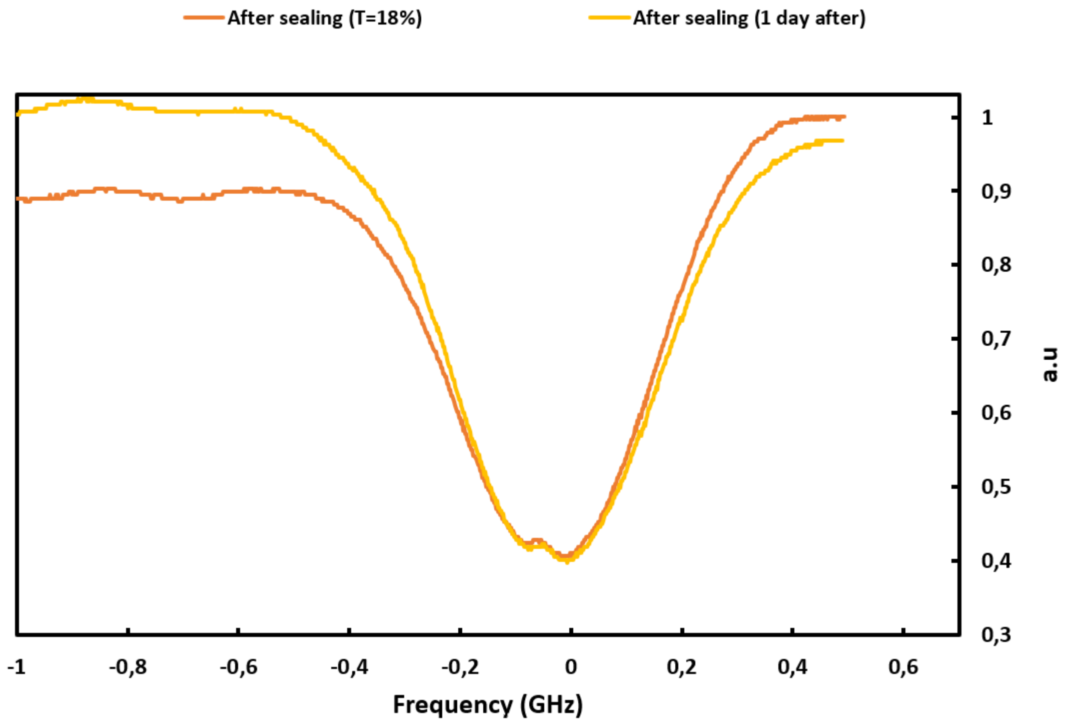

Figure A.2: Saturated absorption in the PMC16 performed at XLim.

On the PMC 16, the MTS signal is much broader than with the hybrid fiber, and we could not use the RedPitaya to scan the entire error signal as the output is limited to ±1 V. An external voltage source was used and the MTS signal was observed has seen on Fig A.3. Using the gain conversion on the *µquans* driver of $\sim$ 22 MHz/V, the MTS is $\sim$ 50 MHz.

CH1 Mean 1.162V
CH1 Pk-to-Pk 1.688V
CH2 Mean -140.2mV

CH1 200mV CH2 500mV 1.00ms 1.25MS/s CH2 ∕ -80.0mV 00:31:23
-768.000µs 20k points 60.0000Hz 30 Mar 2022

Figure A.3: MTS signal after optimisation on the PMC 16. The error signal presents some oscillations probably due to reflection at the splices of the fiber. The MTS signal presented here is filtered with a 1 kHz bandwidth after demodulation.

A.2 PMC 17

Length	2 m
Total transmission	30 %
SAS FWHM	$\sim$ 27 MHz
SAS contrast	7%

Table A.2: Parameters of the PMC 17 measured by XLim.

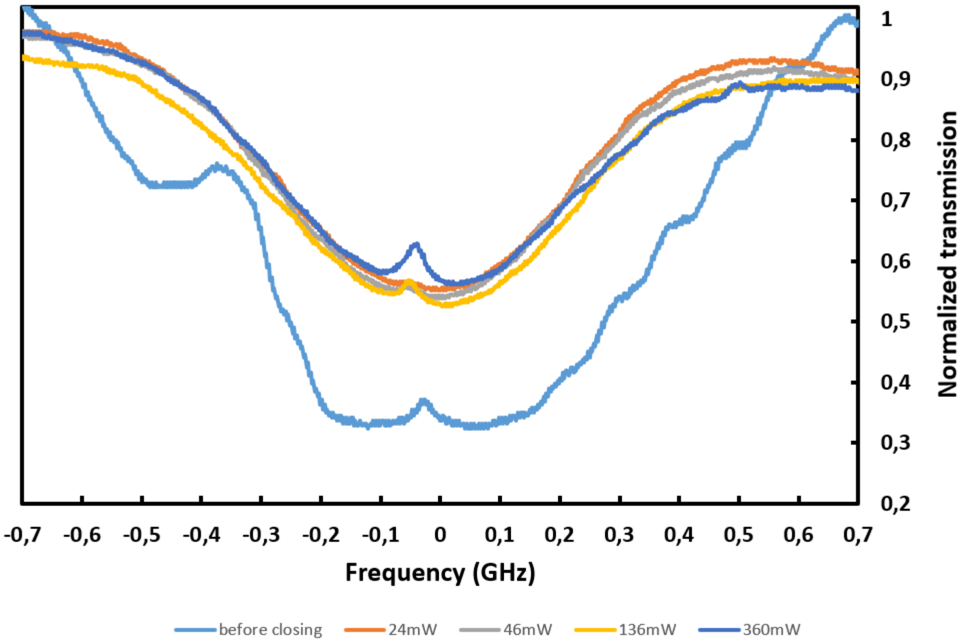

Figure A.4: Saturated absorption in the PMC16 performed at XLim.

On the PMC 17, we observed a broader error signal $\sim$ 25 MHz than with the hybrid fiber (see Fig A.5). This result was also measured by the XLim during the fabrication of the fiber (see table A.2).

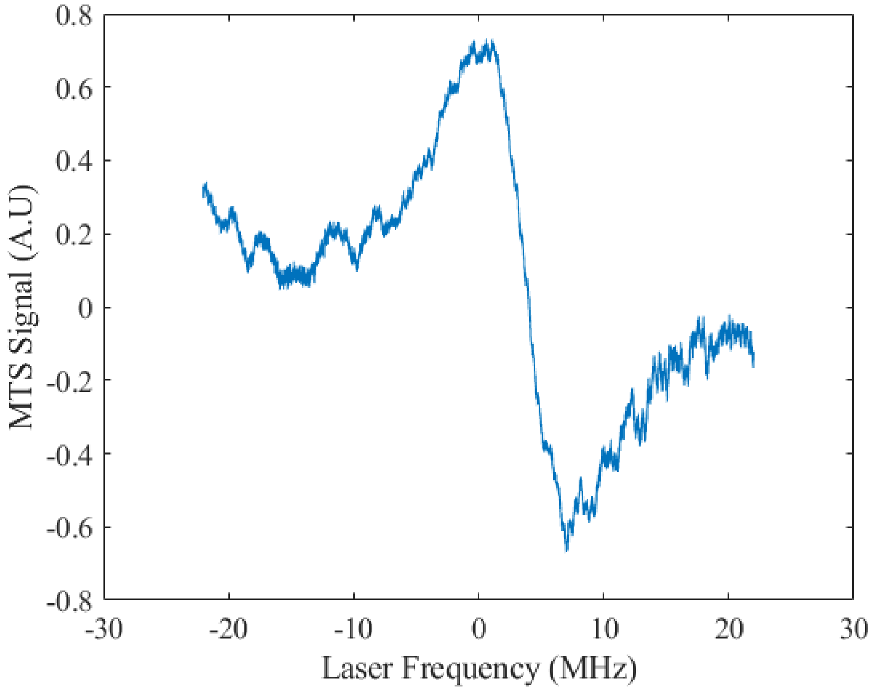

Figure A.5: MTS signal after optimisation on the PMC 17. We can see a degradation of the SNR in the MTS signal compared to the hybrid fiber error signal as well as a broader error signal (∼ 25 MHz). The MTS signal presented here is filtered with a 5 kHz bandwidth after demodulation.

Appendix B

Fiber sensitivity measurements

B.1 Temperature Sensitivity

The detail of the temperature measurements for the two PBG fibers (*PMC 16* and *PMC 17*) are presented here. We detail the measurements protocols that had to be adapted for each fiber.

The temperature measurement is done using the same optical bench and heating platform than for the hybrid fiber. The measurement protocol is the same for all the fiber, only the temperature ramp is changed. We use a linear ramp of 1 K to modulate the temperature of the heating platform.

B.1.1 PMC17

For the PMC17, the frequency has been recorded using the reference cell and a RedPitaya based frequency counter. The beatnote of the lasers is centered around 1 MHz.

On Fig B.1a, we can see that the total fluctuations are $\sim$ 2 MHz over the span of 1 K. The fluctuations present less regularity that the hybrid fiber's fluctuations, but the fluctuation presents a lower frequency profile. This could be the signature of the different modal content of the fiber [38].

To estimate the temperature frequency sensitivity we look at the fast fluctuations of the frequency close to the 0K modulation region, where the laser is locked when we perform the long term measurements. On Fig B.1b, we can see that the sensitivity can be estimated at $\sim$ 15 MHz.K^{-1} for small temperature fluctuations. This is close to the value measured for the hybrid fiber.

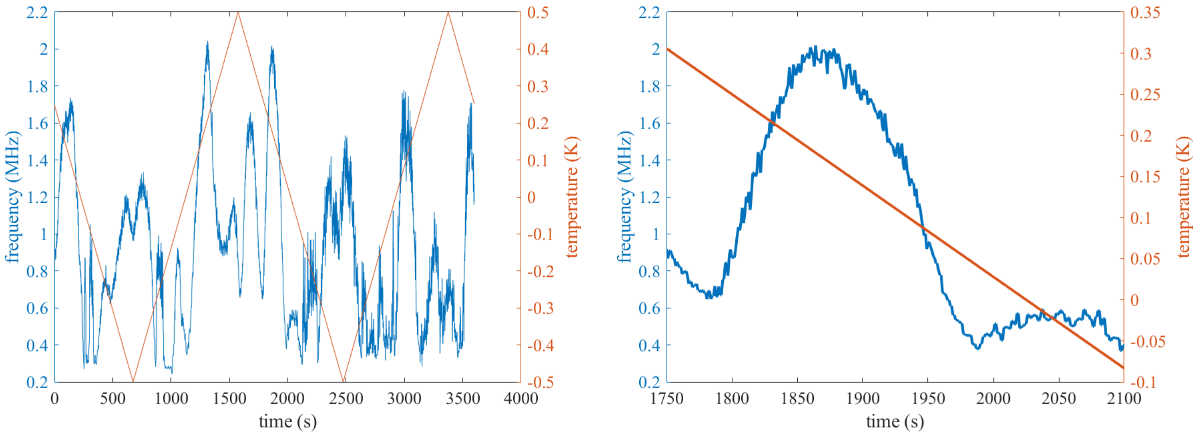

(a) (b)

Figure B.1: (a) Measurement of the frequency of the laser by the comb (blue) vs temperature of the fiber (red). The temperature is modified by the Peltiers while the laser is locked on the fiber's spectroscopy. Measured on the PMC17. (b) Zoom on the linear part of the temperature variations. The sensitivity can be measured as the maximum variation of the frequency in the oscillations. One can linearly fit the variation in laser frequency as well as the temperature to get an estimate of the temperature sensitivity of the fiber.

B.1.2 PMC16

The PMC16's temperature sensitivity has been measured using the frequency comb.

On Fig B.2a, we can see that the total fluctuations are ~ 2 MHz over the span of 1 K. The fluctuation present also less regularity that the hybrid fiber's fluctuations. This could also be the signature of the different modal content of the fiber [38].

To estimate the temperature frequency sensitivity we look at the fluctuations of the frequency close to the 0K modulation region, were the laser is locked when we perform long term measurements. On Fig B.2b, we can see that the sensitivity can be estimated at ~ 13 MHz.K^{-1} for small temperature fluctuations. This is close to the value measured for the hybrid fiber and the PMC17 fiber.

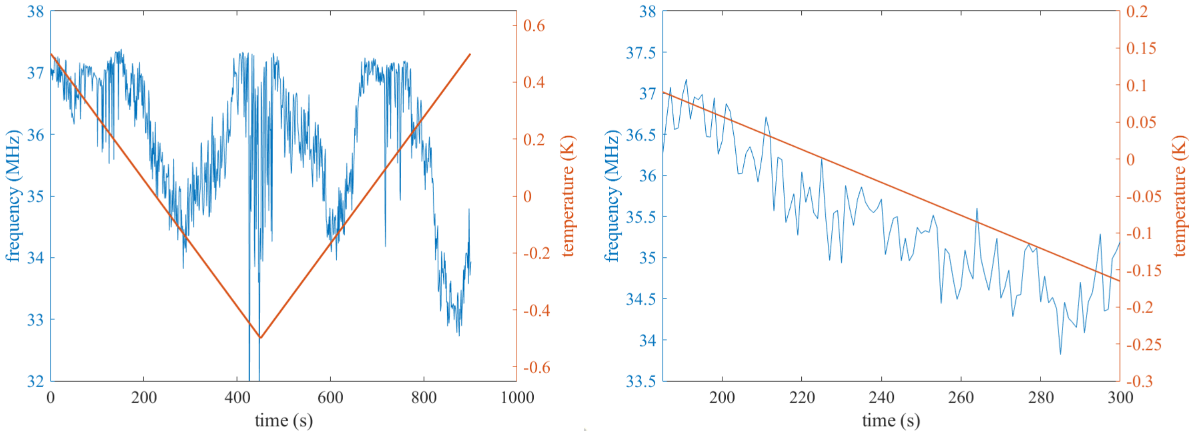

(a) (b)

Figure B.2: (a) Measurement of the frequency of the laser by the comb (blue) vs temperature of the fiber (red). The temperature is modified by the Peltiers while the laser is locked on the fiber's spectroscopy. Measured on the PMC16. (b) Zoom on the linear part of the temperature variations. The sensitivity can be measured as the maximum variation of the frequency in the oscillations. One can linearly fit the variation in laser frequency as well as the temperature to get an estimate of the temperature sensitivity of the fiber.

B.2 Polarization Sensitivity

We present in this section the measurements of polarization sensitivity for the PMC17 and PMC16. To measure the fibre sensitivity, we turn the polarization injected in the fibre using a half-wave-plate. The waveplate is turned by 4° every 30 seconds and the frequency of the locked laser is recorded. For the measurements of PMC17 and PMC16, the beam profiler was not installed on the bench. We could not correlate the mode position to the waveplate angle that could be a signature of the multimode excitation.

B.2.1 PMC17

We change the incident polarization of the probe at the injection of the fiber by turning the waveplate. The frequency is recorded using the RedPitaya and the frequency counter, therefore the frequency is centred around ~ 1 MHz.

Fig B.3 shows that no monotonous variation in frequency arises white changing the polarization. However we can see that the variation is no more than ~ 1.5 MHz, and that close to the lock-point (0°), for small polarization variation, the frequency varies less than ~ 100 kHz.

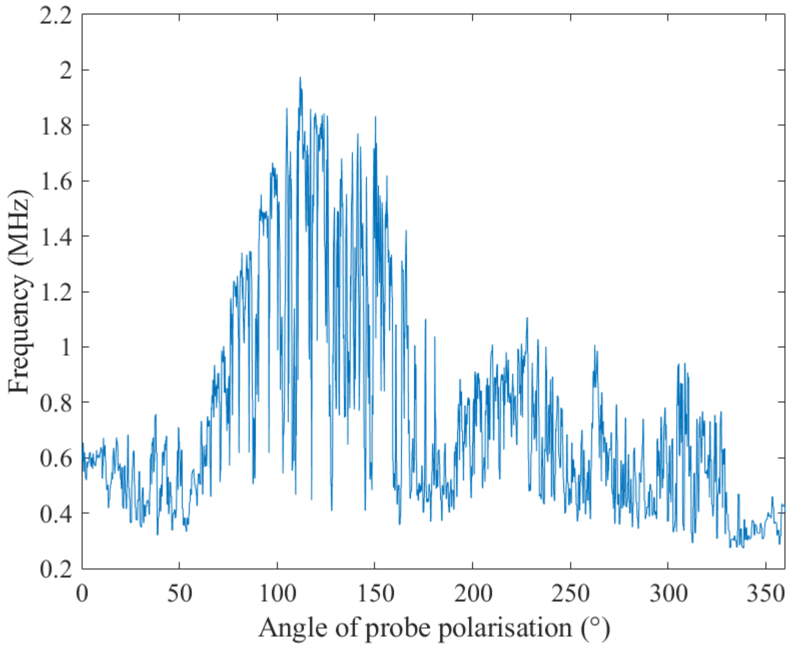

Figure B.3: Measurement of the frequency of the laser by the comb as the polarization of the incident probe is changed. The polarization is changed by manually turning a half-wave-plate.

B.2.2 PMC16

We change the incident polarization of the probe at the injection of the fiber by turning the waveplate. The measurement of the frequency is done with the frequency comb.

On Fig B.4 we see that the frequency sensitivity can be estimated by fitting the data with a linear relation. The fit gives a polarization sensitivity of $\sim$ 10 kHz.deg^{-1}. Close to the lock-point, we can see that the frequency varies less than 500 kHz over a span of $\sim$ 100° so the sensitivity may be less near the lock-point. We see than the overall variation of the frequency is $\sim$ 2.5 MHz, close to what has been observed with other fibers.

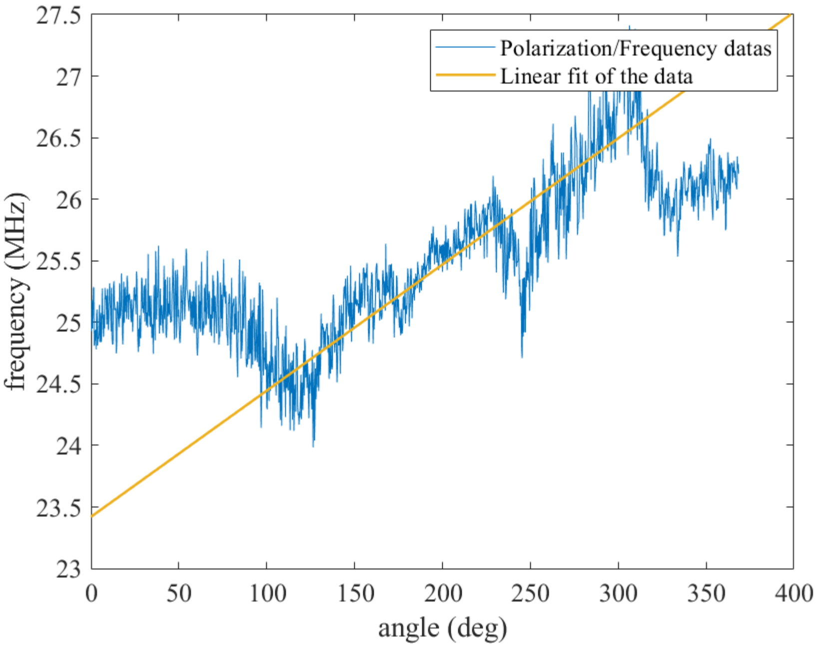

Figure B.4: Measurement of the frequency of the laser by the comb as the polarization of the incident probe is changed. The polarization is changed by manually turning a half-wave-plate.

B.3 Power Sensitivity

The power sensitivity of the fiber has been measured for both the pump and probe beams. We use the same protocol as for the hybrid fiber, the power of the incident beam is changed while the laser is locked and the frequency is measured.

B.3.1 PMC17

Pump power sensitivity

For the PMC17, the frequency is measured using the reference cell and the frequency counter. The pump power is changed by turning the half waveplate in front of the first cube in the setup. As the pump beam goes through a second PBS, we can use the reflected part of this second beam splitter to measure a signal proportional to the incident power in the fiber while still being able to lock the laser. We use this signal measured by a powermeter (ThorLabs S132C) to deduce the pump power sensitivity.

On Fig B.5, we can see the power sensitivity measurement. We start at the full power of the pump, used in normal locking situations, and we reduce it progressively. We can see on B.5b a fit of the data on the 125 first seconds corresponding to the highest pump intensities. The linear fit gives a sensitivity to the pump power of 20 kHz.mW^{-1}.

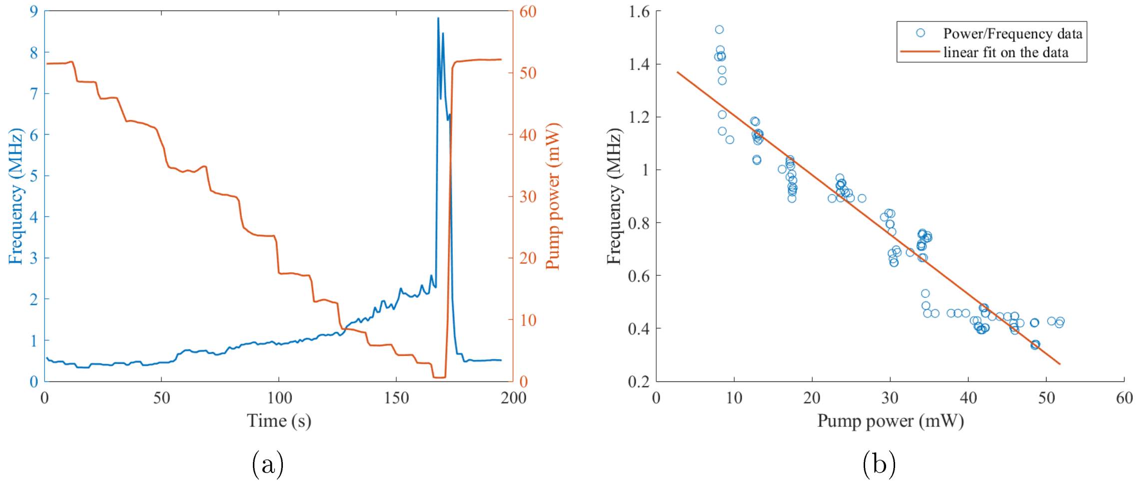

Figure B.5: Measurement of the pump power sensitivity of the PMC17 (a) Representation of the frequency and the optical power along time. The optical power is varied using the first half wave-plate in front of the polarization filtering cube. (b) Representation of the frequency versus optical power and the linear fit used to determine the power sensitivity.

Probe power sensitivity

The probe power sensitivity is measured in the same way as the hybrid sensitivity has been measure. We apply a modulation to the AOM driver on the dedicated amplitude modulation port and measure the corresponding laser lock frequency. We then measure the beam power in front of the fiber using a powermeter when the same modulation is applied.

On Fig B.6 we can see that the probe power has an unusual shape. This is due to the fact that a linear ramp is applied to the modulation port of the G&H AOM driver, but the amplitude of the modulation was too high, leading to a saturation of the driver. At higher probe intensities, the linear tension ramp leads to a non linear variation of the probe intensity. However this is not a problem as the probe power and the frequency are recorded synchronously. The power of the probe beam is recorded using the same technique as for the pump.

We can see a fit using all the data on Fig B.6b, which gives a probe power sensitivity of 10 kHz.mW^{-1} and a total fluctuation of 1 MHz.

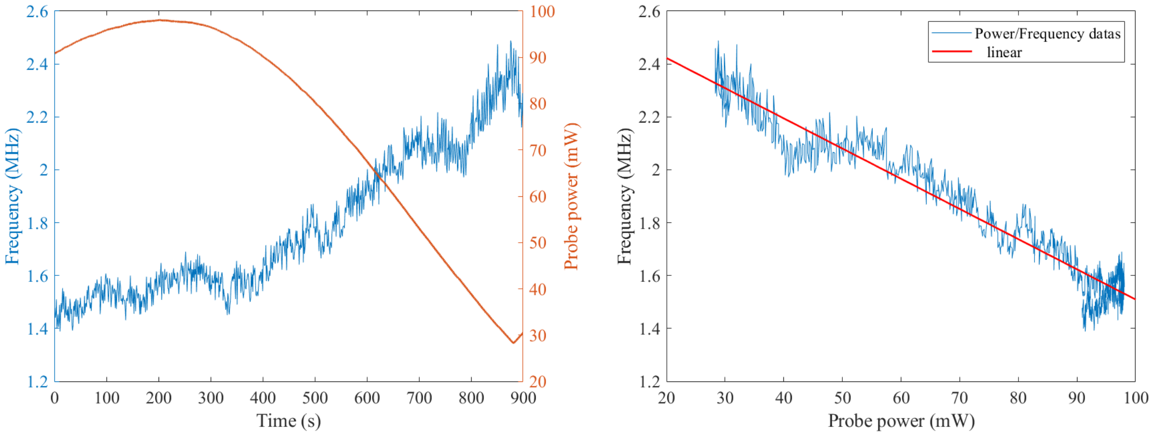

(a) (b)

Figure B.6: Measurement of the probe power sensitivity of the PMC17 (a) Comb measurement of the frequency of the locked laser as a modulation is applied to the RF driver of the AOM to reduce the diffracted power. (b) Linear fit of the frequency data as a function of the optical power.

B.3.2 PMC16

Pump power sensitivity

The PMC16 power fluctuations were recorded using the frequency comb while the beam power is changed. The same technique is used for this measurement than for PMC17. The pump power is changed by turning the half waveplate in front of the first cube in the setup. As the pump beam goes through a second PBS, we can use the reflected part of this second beam splitter to measure a signal proportional to the incident power in the fiber while still being able to lock the laser. We use this signal measured by a powermeter (ThorLabs S132C) to deduce the pump power sensitivity.

On Fig B.7, we can see the power sensitivity measurement. We start at the full power of the pump, used in normal locking situations, and we reduce it progressively. We can see on B.7b a fit of the data on the 250 first seconds corresponding to the highest pump intensities. The linear fit gives a sensitivity to the pump power of 80 kHz.mW^{-1}.

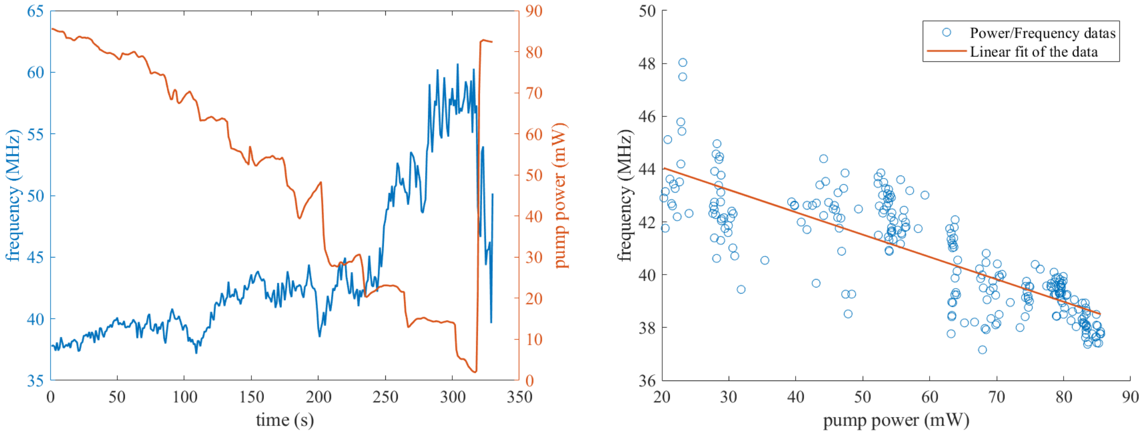

(a) (b)

Figure B.7: Measurement of the pump power sensitivity of the PMC16 (a) Representation of the frequency datas as a function of the optical power. The optical power is varied using the first half wave-plate in front of the polarization filtering cube. (b) Representation of the linear fit used to determine the power sensitivity.

Probe power sensitivity

The probe power sensitivity is measured in the same way as the hybrid sensitivity has been measure. We apply a modulation to the AOM driver on the dedicated amplitude modulation port and measure the corresponding frequency. We then measure the beam power in front of the fiber using a powermeter when the same modulation is applied. For this measurement, there is no saturation effect of the AOM driver as the modulation on the driver had been reduced.

On Fig B.8 we can see that there is no monotonous behaviour of frequency with the probe power. We can see however that the frequency fluctuates of around ~ 2 MHz for small fluctuations near the lock-point at high frequencies.

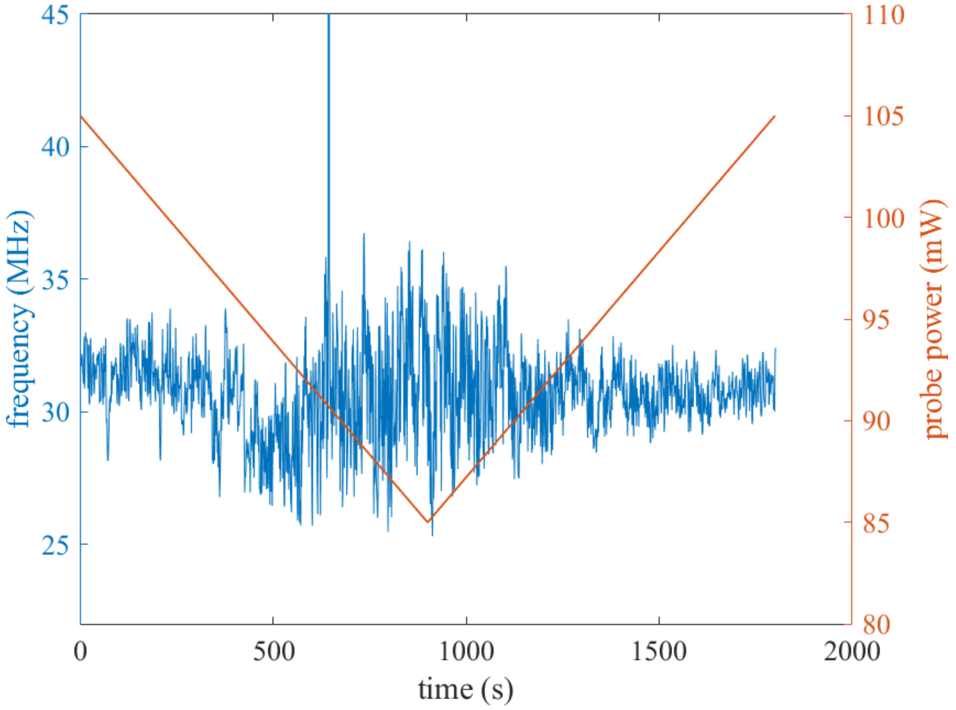

Figure B.8: Measurement of the probe power sensitivity of the PMC16. Comb measurement of the frequency of the locked laser as a modulation is applied to the RF driver of the AOM to reduce the diffracted power.

Appendix C

FPGA Codes

C.1 Frequency counter

The FPGA module for the frequency counter is based on Anton Potočnik's frequency counter project [106]. The frequency counter takes on input the data (typically of the ADCs in our case) and uses a High and a Low thresholds to count the oscillation of the signal.

When the signal is superior to the high threshold and then is lower than the low threshold, an oscillation is counted. The two threshold are necessary to ensure that noise in the signal doesn't result in counted parasitic oscillations.

The module written in Potočnik's project counts the number of clock cycles required to count a certain amount of oscillation in the input signal and outputs this number of clock cycles. This results in an output that is proportional to the inverse of the input frequency.

As we want to implement a feedback loop on the frequency with this module, it has been changed to count and output the number of oscillation of the input signal for a given number of clock cycles.

This way, the output of the *linearised* frequency counter can be used conveniently to lock the frequency of the input signal.

C.1.1 Module Parameters

- `ADC_WIDTH`: Width of the ADC data (default: 14 bits).
- `AXIS_TDATA_WIDTH`: Width of the AXIS data (default: 32 bits).
- `COUNT_WIDTH`: Width of the counter (default: 32 bits).
- `HIGH_THRESHOLD`: Threshold value for detecting high signal transitions (default: 100).
- `LOW_THRESHOLD`: Threshold value for detecting low signal transitions (default: -150).

C.1.2 Inputs

- `S_AXIS_IN_tdata`: Input data stream from the ADC, with width `AXIS_TDATA_WIDTH`.
- `S_AXIS_IN_tvalid`: Input valid signal for the data stream.
- `clk`: Clock input.
- `rst`: Reset input for resetting the module to a known state.
- `Ncounter`: Configurable number of clock cycles to measure the frequency.

C.1.3 Outputs

- `M_AXIS_OUT_tdata`: Output data stream, same as input data `S_AXIS_IN_tdata`.
- `M_AXIS_OUT_tvalid`: Output valid signal for the data stream.
- `counter_output`: Output representing the measured frequency based on the reciprocal method.

Module Description

The `frequency_counter_lin` module performs the following tasks:

1. Extracts the 14-bit ADC data from the input data stream (`S_AXIS_IN_tdata`).
2. Detects signal transitions in the ADC data based on the threshold values (`HIGH_THRESHOLD` and `LOW_THRESHOLD`). Those values can be changed if the input signal amplitude or offset requires it. These value are given for a full scale sin input, taking into account the board's ADC offset.
3. Counts the number of rising edges in the input signal using a state buffer (`state` and `state_next`).
4. Increments the counter (`counter` and `counter_next`) on each clock cycle.
5. Increments the cycle counter (`cycle` and `cycle_next`) on each signal transition.
6. Measures the frequency based on the number of cycles counted within the specified time limit (defined by `Ncounter`$*f_{clk}$ with f_{clk} the frequency clock of the FPGA).

The output frequency is available on the `counter_output` output. The module operates on the rising edges of the clock input (`clk`) and can be reset to a known state using the reset input (`rst`).

C.1.4 Source Code

Listing C.1: Linear Frequency Counter

```
module frequency_counter_lin #
(
parameter ADC_WIDTH = 14,
parameter AXIS_TDATA_WIDTH = 32,
parameter COUNT_WIDTH = 32,
parameter HIGH_THRESHOLD = 100,
parameter LOW_THRESHOLD = -150
)
(
(* X_INTERFACE_PARAMETER = "FREQ_HZ 250000000" *)
input [AXIS_TDATA_WIDTH-1:0]   S_AXIS_IN_tdata,
input                          S_AXIS_IN_tvalid,
input                          clk,
input                          rst,
//    input [4:0]                      dec,
input [COUNT_WIDTH-1:0]        Ncounter,
output [AXIS_TDATA_WIDTH-1:0]  M_AXIS_OUT_tdata,
output                         M_AXIS_OUT_tvalid,
output [COUNT_WIDTH-1:0]       counter_output
);

reg signed [ADC_WIDTH-1:0]     data;
reg                            state, state_next;
reg [COUNT_WIDTH-1:0]          counter=0, counter_next=0;
reg [COUNT_WIDTH-1:0]          counter_output=0,
   counter_output_next=0;
reg [COUNT_WIDTH-1:0]          cycle=0, cycle_next=0;




// Wire AXIS IN to AXIS OUT
assign  M_AXIS_OUT_tdata[AXIS_TDATA_WIDTH-1:0] =
   S_AXIS_IN_tdata[AXIS_TDATA_WIDTH-1:0];
assign  M_AXIS_OUT_tvalid = S_AXIS_IN_tvalid;

// Extract only the 14-bits of ADC data
always @(posedge clk)
begin
data <= S_AXIS_IN_tdata[ADC_WIDTH-1+2:0+2];
end



// Handling of the state buffer for finding signal
   transition at the threshold
always @(posedge clk)
begin
if (~rst)
```

```
state <= 1'b0;
else
state <= state_next;
end


always @*              // logic for state buffer
begin
if (data > HIGH_THRESHOLD)
state_next = 1;
else if (data < LOW_THRESHOLD)
state_next = 0;
else
state_next = state;
end




// Handling of counter, counter_output and cycle buffer
always @(posedge clk)
begin
if (~rst)
begin
counter <= 0;
counter_output <= 0;
cycle <= 0;
end
else
begin
counter <= counter_next;
counter_output <= counter_output_next;
cycle <= cycle_next;
end
end


always @* // logic for counter, counter_output, and cycle buffer
begin
counter_next = counter + 1; // increment on each clock cycle
counter_output_next = counter_output;
cycle_next = cycle;

if (state < state_next) // high to low signal transition
begin
cycle_next = cycle + 1; // increment on each signal transition
if (counter >= Ncounter-1)
begin
counter_next = 0;
```

```
        counter_output_next = cycle;
        cycle_next = 0;
        end
        end
        end


        endmodule
```

C.2 Phase Detection

The `sampler` module is a sampling circuit designed to perform phase detection for an input signal based on the principle explained in section 4.2.4. It takes a 14-bit input signal (`din`) and samples it based on the rising edges of the clock signal (`clk`). The clock frequency is expected to be four times the frequency of the input signal to enable phase detection. Once every two clock cycles, the module captures the input signal value and takes the negative value of the input signal every two acquisitions, allowing for phase comparison. The sampled data is available as an output signal ($\mathtt{d}_\mathtt{o}$), which can be used for phase locking, as it is a signal proportional to the sin of the input signal's phase.

C.2.1 Inputs

- `din`: A 14-bit input signal representing the data to be sampled.
- `clk`: Clock input.

C.2.2 Outputs

- `d_o`: A 14-bit output signal representing the sampled data.

C.2.3 Module Description

The `sampler` module performs the following tasks:

1. The input signal (`din`) is sampled based on the rising edges of the clock signal (`clk`).
2. The clock frequency is assumed to be four times the frequency of the input signal, allowing phase detection between the input signal and the clock.
3. During each input signal cycle, the module captures the current input signal value and the phase opposition value from the previous half cycle.
4. The phase data is averaged over a cycle of the input signal, this allows for removal of any DC offset of the input signal.
5. The sampled data is available at the output signal (`d_o`), which can be used for phase analysis or other applications.

The `sampler` module allows for phase detection by taking advantage of the relationship between the clock frequency and the input signal frequency. The output data at the output can be used as an error signal to determine the phase difference between the input signal and the FPGA clock.

C.2.4 Source Code

Listing C.2: Sampling Phase detector

```
module sampler( din , dout , clk );

input  [13:0] din;
input         clk;
output reg [14:0] dout;

reg [13:0] dout_buff;
reg [13:0] dout_buff2;
wire[13:0] din;
wire clk;
wire [14:0] dout_sum;

reg [1:0] count = 0;

always @( posedge clk )
begin
if( count == 1)
begin
dout_buff = din;
end
if( count == 3)
begin
dout_buff2 = -din;
end
count = count + 1;
end

assign dout_sum = $signed(dout_buff) + $signed(dout_buff2);

always @( posedge clk)
begin
if( count[0] == 0)
dout = dout_sum;
end

endmodule
```

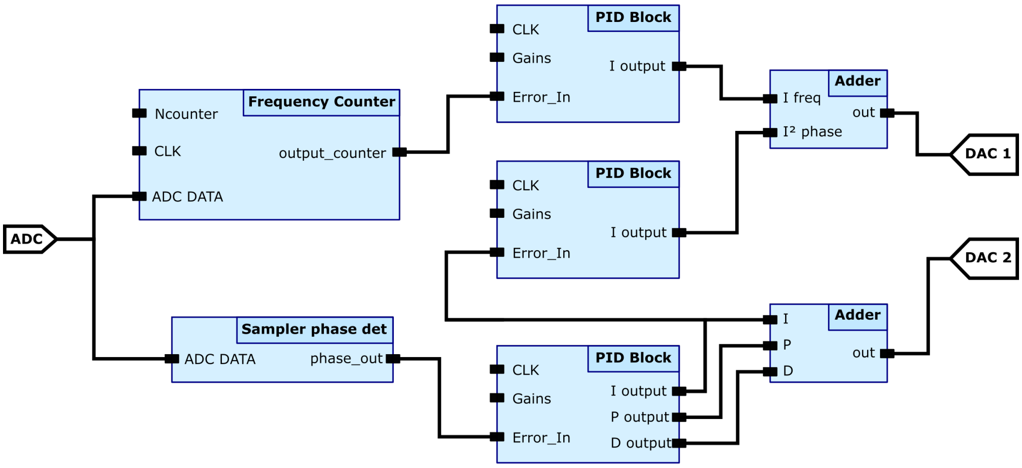

Figure C.1: Block diagram of the frequency and phase loop.

C.3 Frequency and Phase loop

In this annex, we present the block diagram of the FPGA design used to lock the frequency and the phase of the lasers. The design is used to measure and lock the frequency and the phase of the input signal, the loop gains can be adjusted by using a C program that writes data on dedicated section of the FPGA. We summarize here each component's functionality and their role within the system. On Fig C.1 the design is presented as a simplified block diagram.

The FPGA design starts with the Analog-to-Digital Converter (ADC) pins. The ADC's data is received as $14bits$ values proportional to the input voltage. The converted digital data is then picked up by the frequency counter and the sampler phase detector.

The frequency counter receives the ADC signal and measures its frequency. It also takes as input the number of clock cycles (Ncounter) during which it measures the frequency (see C.1). Care must be taken with this input since the output of the frequency counter is dependent on its value. Not represented is a set-point input that ensures the frequency counter gives an error signal that is null when the desired frequency is measured, and this set-pins also depends on the Ncounter input. The frequency counter also uses the ADC's clock (CLK) for synchronization.

Running parallel to the frequency counter, the sampler phase detector calculates the phase of the ADC signal. The details of this phase calculation are outlined in section 4.2.4 and annex C.2.

The outputs of the frequency counter and sampler phase detector are fed into separate PID modules. These modules have gains controllable by an input referred to as *Gains*. The PID module following the frequency counter adds its output to the I^2 *phase* signal before passing it to DAC 1.

The sampler phase detector's output feeds into another PID module. The output of each P, I, and D component of this PID module is split. The I output is integrated again in another PID block, generating an I^2 output. As it is the phase being doubly integrated, it is also equivalent to the frequency integrated once. This allows the frequency lock part to be stopped when the phase is locked. The P and D outputs are added together and sent to DAC 2 for phase lock.

Finally, the outputs from the PID modules are converted back into analog signals by the two DACs, DAC 1 and DAC 2.

Bibliography

[1] Andreas Bauch. Caesium atomic clocks: function, performance and applications. *Measurement Science and Technology*, 14(8):1159–1173, jul 2003.

[2] Iván Alonso et al. Cold atoms in space: community workshop summary and proposed road-map. *EPJ Quantum Technology*, 9(1), nov 2022.

[3] Ch Antoine and Ch J Bord. Quantum theory of atomic clocks and gravito-inertial sensors: an update. *Journal of Optics B: Quantum and Semiclassical Optics*, 5(2):S199–S207, apr 2003.

[4] Robert W. Boyd, Daniel J. Gauthier, and Alexander L. Gaeta. Applications of slow light in telecommunications. *Optics and Photonics News*, 17(4):18, apr 2006.

[5] B. Battelier, B. Barrett, L. Fouché, L. Chichet, L. Antoni-Micollier, H. Porte, F. Napolitano, J. Lautier, A. Landragin, and P. Bouyer. Development of compact cold-atom sensors for inertial navigation. apr 2016.

[6] Md Habib Ullah, Rozhin Eskandarpour, Honghao Zheng, and Amin Khodaei. Quantum computing for smart grid applications. *IET Generation, Transmission, Distribution*, 16(21):4239–4257, sep 2022.

[7] F.X. Esnault, N. Rossetto, D. Holleville, J. Delporte, and N. Dimarcq. HORACE: A compact cold atom clock for galileo. *Advances in Space Research*, 47(5):854–858, mar 2011.

[8] Daniel Tazartes. An historical perspective on inertial navigation systems. In *2014 International Symposium on Inertial Sensors and Systems (ISISS)*. IEEE, feb 2014.

[9] Vincent Ménoret, Pierre Vermeulen, Nicolas Le Moigne, Sylvain Bonvalot, Philippe Bouyer, Arnaud Landragin, and Bruno Desruelle. Gravity measurements below 10-9 g with a transportable absolute quantum gravimeter. *Scientific Reports*, 8(1), aug 2018.

[10] V. Schkolnik, O. Hellmig, A. Wenzlawski, J. Grosse, A. Kohfeldt, K. Döringshoff, A. Wicht, P. Windpassinger, K. Sengstock, C. Braxmaier, M. Krutzik, and A. Peters. A compact and robust diode laser system for atom interferometry on a sounding rocket. *Applied Physics B*, 122(8), jul 2016.

[11] Philippe Laurent, Didier Massonnet, Luigi Cacciapuoti, and Christophe Salomon. The ACES/PHARAO space mission. *Comptes Rendus Physique*, 16(5):540–552, jun 2015.

[12] Chenchen Wang, Natalie V. Wheeler, Coralie Fourcade-Dutin, Michael Grogan, Thomas D. Bradley, Brian R. Washburn, Fetah Benabid, and Kristan L. Corwin. Acetylene frequency references in gas-filled hollow optical fiber and photonic microcells. *Applied Optics*, 52(22):5430, jul 2013.

[13] F. Benabid, F. Couny, J. C. Knight, T. A. Birks, and P. St J. Russell. Compact, stable and efficient all-fibre gas cells using hollow-core photonic crystal fibres. *Nature*, 434(7032):488–491, mar 2005.

[14] Charbel Cherfan, Isam Manai, Samir Zemmouri, Jean-Claude Garreau, Jean-François Clément, Pascal Szriftgiser, and Radu Chicireanu. Acetylene-based frequency stabilization of a laser system for potassium laser cooling. *Optics Express*, 28(1):494, jan 2020.

[15] J. Le Gouët, J. Kim, C. Bourassin-Bouchet, M. Lours, A. Landragin, and F. Pereira Dos Santos. Wide bandwidth phase-locked diode laser with an intracavity electro-optic modulator. *Optics Communications*, 282(5):977–980, mar 2009.

[16] Richard L. Boyd. An optical phase locked loop for semiconductor lasers, 1988.

[17] Henri de Bellecize. La réception synchrone. *L Onde Electrique*, June 1932.

[18] A. Davis, M. Pettitt, J. King, and S. Wright. Phase diversity techniques for coherent optical receivers. *Journal of Lightwave Technology*, 5(4):561–572, 1987.

[19] Rongqing Hui. *Introduction to Fiber-Optic Communications*. Elsevier Science and Technology Books, 2019.

[20] Yunfeng Gu, Sheng Cui, Changjian Ke, Keji Zhou, and Deming Liu. All-digital timing recovery for free space optical communication signals with a large dynamic range and low OSNR. *IEEE Photonics Journal*, 11(6):1–11, dec 2019.

[21] Takako Hirokawa, Sergio Pinna, Navid Hosseinzadeh, Aaron Maharry, Hector Andrade, Junqian Liu, Thomas Meissner, Stephen Misak, Ghazal Movaghar, Luis A. Valenzuela, Yujie Xia, Shireesh Bhat, Fabrizio Gambini, Jonathan Klamkin, Adel A. M. Saleh, Larry Coldren, James F. Buckwalter, and Clint L. Schow. Analog coherent detection for energy efficient intra-data center links at 200 gbps per wavelength. *Journal of Lightwave Technology*, 39(2):520–531, jan 2021.

[22] Daniel A. Steck. Rubidium 87 d line data. https://steck.us/alkalidata/rubidium87numbers.1.6.pdf, 2019.

[23] R.A. Valenzuela, L.J. Cimini, R.W. Wilson, K.C. Reichmann, and A. Grot. Frequency stabilisation of AlGaAs lasers to absorption spectrum of rubidium using zeeman effect. *Electronics Letters*, 24(12):725, 1988.

[24] T.G. Tiecke. Properties of potassium. https://www.tobiastiecke.nl/archive/PotassiumProperties.p 2019.

[25] K. Nakagawa, M. de Labachelerie, Y. Awaji, and M. Kourogi. Accurate optical frequency atlas of the 15-μm bands of acetylene. *Journal of the Optical Society of America B*, 13(12):2708, dec 1996.

[26] Kenichi Nakagawa and Atsushi Onae. Development of an acetylene optical frequency standard at 1.5 um and its applications. In *SPIE Proceedings*. SPIE, may 2001.

[27] Sarah Gilbert and William Swann. Acetylene ¹²c₂h₂ absorption reference for 1510 nm to 1540 nm wavelength calibration srm 2517a, 2001-02-01 00:02:00 2001.

[28] Thomas Talvard, Philip G. Westergaard, Michael V. DePalatis, Nicolai F. Mortensen, Michael Drewsen, Bjarke Gøth, and Jan Hald. Enhancement of the performance of a fiber-based frequency comb by referencing to an acetylene-stabilized fiber laser. *Optics Express*, 25(3):2259, jan 2017.

[29] K. Nakagawa, A. Onse, K. Okumura, and J. Yoda. Development of a compact acetylene optical frequency standard at 1.5 μm. In *Conference on Precision Electromagnetic Measurements. Conference Digest. CPEM 2000 (Cat. No.00CH37031)*. IEEE.

[30] Jan Hald, Lars Nielsen, Jan C. Petersen, Poul Varming, and Jens E. Pedersen. Fiber laser optical frequency standard at 1.54 um. *Optics Express*, 19(3):2052, jan 2011.

[31] Marco Triches, Mattia Michieletto, Jan Hald, Jens K. Lyngsø, Jesper Lægsgaard, and Ole Bang. Optical frequency standard using acetylene-filled hollow-core photonic crystal fibers. *Optics Express*, 23(9):11227, apr 2015.

[32] Alan Fried, James R. Drummond, Bruce Henry, and Jack Fox. Reduction of interference fringes in small multipass absorption cells by pressure modulation. *Applied Optics*, 29(7):900, mar 1990.

[33] John U. White. Long optical paths of large aperture. *Journal of the Optical Society of America*, 32(5):285, may 1942.

[34] Claude Robert. Simple, stable, and compact multiple-reflection optical cell for very long optical paths. *Applied Optics*, 46(22):5408, jul 2007.

[35] Manuel Graf, Herbert Looser, Lukas Emmenegger, and Béla Tuzson. Beam folding analysis and optimization of mask-enhanced toroidal multipass cells. *Optics Letters*, 42(16):3137, aug 2017.

[36] Zachary L. Newman, Vincent Maurice, Tara Drake, Jordan R. Stone, Travis C. Briles, Daryl T. Spencer, Connor Fredrick, Qing Li, Daron Westly, B. R. Ilic, Boqiang Shen, Myoung-Gyun Suh, Ki Youl Yang, Cort Johnson, David M. S. Johnson, Leo Hollberg, Kerry J. Vahala, Kartik Srinivasan, Scott A. Diddams, John Kitching, Scott B. Papp, and Matthew T. Hummon. Architecture for the photonic integration of an optical atomic clock. *Optica*, 6(5):680, may 2019.

[37] H. Schmidt, Dongliang Yin, J.P. Barber, and A.R. Hawkins. Hollow-core waveguides and 2-d waveguide arrays for integrated optics of gases and liquids. *IEEE Journal of Selected Topics in Quantum Electronics*, 11(2):519–527, mar 2005.

[38] Thomas Billotte. *Conception et élaboration de micro-capsules photoniques pour les références de fréquences et la photonique atomique*. PhD thesis, 2021. Thèse de doctorat dirigée par Benabid, Fetah et Debord, Benoît Electronique des hautes fréquences, photonique et systèmes Limoges 2021.

[39] Marco Triches, Anders Brusch, and Jan Hald. Portable optical frequency standard based on sealed gas-filled hollow-core fiber using a novel encapsulation technique. *Applied Physics B*, 121(3):251–258, sep 2015.

[40] Jan Hald, Jan C. Petersen, and Jes Henningsen. Saturated optical absorption by slow molecules in hollow-core photonic band-gap fibers. *Physical Review Letters*, 98(21):213902, may 2007.

[41] Sune Svanberg. *Atomic and Molecular Spectroscopy.* Springer Berlin Heidelberg, 2004.

[42] I.E. Gordon, L.S. Rothman, R.J. Hargreaves, R. Hashemi, E.V. Karlovets, F.M. Skinner, E.K. Conway, C. Hill, R.V. Kochanov, Y. Tan, P. Wcisło, A.A. Finenko, K. Nelson, P.F. Bernath, M. Birk, V. Boudon, A. Campargue, K.V. Chance, A. Coustenis, B.J. Drouin, J.–M. Flaud, R.R. Gamache, J.T. Hodges, D. Jacquemart, E.J. Mlawer, A.V. Nikitin, V.I. Perevalov, M. Rotger, J. Tennyson, G.C. Toon, H. Tran, V.G. Tyuterev, E.M. Adkins, A. Baker, A. Barbe, E. Canè, A.G. Császár, A. Dudaryonok, O. Egorov, A.J. Fleisher, H. Fleurbaey, A. Foltynowicz, T. Furtenbacher, J.J. Harrison, J.–M. Hartmann, V.–M. Horneman, X. Huang, T. Karman, J. Karns, S. Kassi, I. Kleiner, V. Kofman, F. Kwabia–Tchana, N.N. Lavrentieva, T.J. Lee, D.A. Long, A.A. Lukashevskaya, O.M. Lyulin, V.Yu. Makhnev, W. Matt, S.T. Massie, M. Melosso, S.N. Mikhailenko, D. Mondelain, H.S.P. MÃ¼ller, O.V. Naumenko, A. Perrin, O.L. Polyansky, E. Raddaoui, P.L. Raston, Z.D. Reed, M. Rey, C. Richard, R. Tóbiás, I. Sadiek, D.W. Schwenke, E. Starikova, K. Sung, F. Tamassia, S.A. Tashkun, J. Vander Auwera, I.A. Vasilenko, A.A. Vigasin, G.L. Villanueva, B. Vispoel, G. Wagner, A. Yachmenev, and S.N. Yurchenko. The HITRAN2020 molecular spectroscopic database. *Journal of Quantitative Spectroscopy and Radiative Transfer*, 277:107949, jan 2022.

[43] J. L. Hall, C. J. Bordé, and K. Uehara. Direct optical resolution of the recoil effect using saturated absorption spectroscopy. *Physical Review Letters*, 37(20):1339–1342, nov 1976.

[44] Stephen E. Harris. Electromagnetically induced transparency. *Physics Today*, 50(7):36–42, jul 1997.

[45] E. Arimondo. V coherent population trapping in laser spectroscopy. In *Progress in Optics*, pages 257–354. Elsevier, 1996.

[46] Norman F. Ramsey. A molecular beam resonance method with separated oscillating fields. *Physical Review*, 78(6):695–699, jun 1950.

[47] Ch. J. Bordé, Ch. Salomon, S. Avrillier, A. van Lerberghe, Ch. Bréant, D. Bassi, and G. Scoles. Optical ramsey fringes with traveling waves. *Physical Review A*, 30(4):1836–1848, oct 1984.

[48] Sumanta Khan, Molahalli Panidhara Kumar, Vineet Bharti, and Vasant Natarajan. Coherent population trapping (CPT) versus electromagnetically induced transparency (EIT). *The European Physical Journal D*, 71(2), feb 2017.

[49] G. Camy, Ch.J. Bordé, and M. Ducloy. Heterodyne saturation spectroscopy through frequency modulation of the saturating beam. *Optics Communications*, 41(5):325–330, may 1982.

[50] M. Ducloy and D. Bloch. Theory of degenerate four-wave mixing in resonant doppler-broadened media. - II. doppler-free heterodyne spectroscopy via collinear four-wave mixing in two- and three-level systems. *Journal de Physique*, 43(1):57–65, 1982.

[51] Daniel Bloch. Mélange dégénéré à quatre ondes en milieu gazeux résonnant : applications à la conjugaison de phase et à la spectroscopie hétérodyne à haute fréquence, 1984.

[52] A. Icsevgi and W. E. Lamb. Propagation of light pulses in a laser amplifier. *Physical Review*, 185(2):517–545, sep 1969.

[53] Y.K. Wang and I.C. Khoo. On the wigner-weisskopf approximation in quantum optics. *Optics Communications*, 11(4):323–326, aug 1974.

[54] Willis E. Lamb. Theory of an optical maser. *Physical Review*, 134(6A):A1429–A1450, jun 1964.

[55] Amnon Yariv and David M. Pepper. Amplified reflection, phase conjugation, and oscillation in degenerate four-wave mixing. *Optics Letters*, 1(1):16, jul 1977.

[56] Tilman Preuschoff, Malte Schlosser, and Gerhard Birkl. Optimization strategies for modulation transfer spectroscopy applied to laser stabilization. *Optics Express*, 26(18):24010, aug 2018.

[57] Daniel A. Steck. Quantum and atom optics. available online at http://steck.us/teaching. (revision 0.13.19, 6 April 2023).

[58] Wolfgang Demtröder. *Laser Spectroscopy*. Springer Berlin Heidelberg, 2008.

[59] L Fonda, G C Ghirardi, and A Rimini. Decay theory of unstable quantum systems. *Reports on Progress in Physics*, 41(4):587–631, apr 1978.

[60] W. C. Swann and S. L. Gilbert. Pressure-induced shift and broadening of 1510–1540-nm acetylene wavelength calibration lines. *Journal of the Optical Society of America B*, 17(7):1263, jul 2000.

[61] C. J. Bordé, J. L. Hall, C. V. Kunasz, and D. G. Hummer. Saturated absorption line shape: Calculation of the transit-time broadening by a perturbation approach. *Physical Review A*, 14(1):236–263, jul 1976.

[62] Muhammad Adnan. *Experimental platform towards in-fibre atom optics and laser cooling*. Theses, Université de Limoges, December 2017.

[63] J. Rutman and F.L. Walls. Characterization of frequency stability in precision frequency sources. *Proceedings of the IEEE*, 79(7):952–960, jul 1991.

[64] L.S. Cutler and C.L. Searle. Some aspects of the theory and measurement of frequency fluctuations in frequency standards. *Proceedings of the IEEE*, 54(2):136–154, 1966.

[65] Enrico Rubiola, Ertan Salik, Shouhua Huang, Nan Yu, and Lute Maleki. Photonic-delay technique for phase-noise measurement of microwave oscillators. *Journal of the Optical Society of America B*, 22(5):987, may 2005.

[66] Fritz Riehle. *Frequency Standards.* Wiley, sep 2003.

[67] Andrea Cardenas Olaya. *Digital instrumentation for the measurement of high spectral purity signals.* Theses, Université Bourgogne Franche-Comté ; Politecnico di Torino, July 2018.

[68] StemLABS. Redpitaya documentation, 2023.

[69] Leonhard Neuhaus. *Cooling a macroscopic mechanical oscillator close to its quantum ground state.* Theses, Université Pierre et Marie Curie - Paris VI, December 2016.

[70] T. Billotte, G. Baclet, J. H. Osório, F. Delahaye, V. Mançois, A. Hilico, M. Maurel, M. Chafer, F. Amrani, F. Gérôme, B. Debord, P. Bouyer, S. Bernon, and F. Benabid. Single mode inhibited coupling fiber for sub doppler spectroscopy. In *Conference on Lasers and Electro-Optics.* Optica Publishing Group, 2021.

[71] Gilmore J. Dunning and R. C. Lind. Demonstration of image transmission through fibers by optical phase conjugation. *Optics Letters*, 7(11):558, nov 1982.

[72] Antonio M. Caravaca-Aguirre, Eyal Niv, Donald B. Conkey, and Rafael Piestun. Real-time resilient focusing through a bending multimode fiber. *Optics Express*, 21(10):12881, may 2013.

[73] Martin Plöschner, Tomáš Tyc, and Tomáš Čižmár. Seeing through chaos in multimode fibres. *Nature Photonics*, 9(8):529–535, jul 2015.

[74] Vinayak Dangui, Hyang Kyun Kim, Michel J. F. Digonnet, and Gordon S. Kino. Phase sensitivity to temperature of the fundamental mode in air-guiding photonic-bandgap fibers. *Optics Express*, 13(18):6669, 2005.

[75] Thomas Billotte, Matthieu Chafer, Martin Maurel, Foued Amrani, Frederic Gerome, Benoit Debord, and Fetah Benabid. Contaminant-free end-capped and single-mode acetylene photonic microcell for sub-doppler spectroscopy. *Optics Letters*, 46(3):456, jan 2021.

[76] Klaas Bergmann. STIRAP: A historical perspective and some news. In *Molecular Beams in Physics and Chemistry*, pages 445–462. Springer International Publishing, 2021.

[77] Claude Cohen-Tannoudji. Dark resonances from optical pumping to cold atoms and molecules. *Physica Scripta*, 90(8):088013, jul 2015.

[78] C. H. Raymond Ooi. Laser cooling of molecules by zero-velocity selection and single spontaneous emission. *Physical Review A*, 82(5):053408, nov 2010.

[79] Jack Saywell, Max Carey, Mohammad Belal, Ilya Kuprov, and Tim Freegarde. Optimal control of raman pulse sequences for atom interferometry. *Journal of Physics B: Atomic, Molecular and Optical Physics*, 53(8):085006, mar 2020.

[80] Mark Kasevich and Steven Chu. Atomic interferometry using stimulated raman transitions. *Physical Review Letters*, 67(2):181–184, jul 1991.

[81] Patrick Cheinet. *Conception et réalisation d'un gravimètre à atomes froids*. PhD thesis, 2006. Thèse de doctorat dirigée par Tuckey, Philip Laser et matière Paris 6 2006.

[82] B Fermigier, G Lucas-Leclin, J Dupont, F Plumelle, and M Houssin. Self-aligned external-cavity semiconductor lasers for high resolution spectroscopy. *Optics Communications*, 153(1-3):73–77, jul 1998.

[83] LUNA, RIO. Planex 1550 nm laser diode, 2023.

[84] Jürgen Appel, Andrew MacRae, and A I Lvovsky. A versatile digital GHz phase lock for external cavity diode lasers. *Measurement Science and Technology*, 20(5):055302, apr 2009.

[85] S. Kobayashi, Y. Yamamoto, M. Ito, and T. Kimura. Direct frequency modulation in AlGaAs semiconductor lasers. *IEEE Transactions on Microwave Theory and Techniques*, 30(4):428–441, 1982.

[86] Edmund Optics Inc. Thermal properties of optical substrates, 2023.

[87] Amnon Yariv and Pochi Yeh. *Optical Waves in Crystals*. Wiley-Interscience.

[88] M.C. Fischer. Frequency domain measurement systems. 10th Annual Precise Time and Time Interval Applications and Planning Meeting, December 1978.

[89] James A. Crawford. *Frequency Synthesizer Design Handbook*. artechhouse, 1 edition, 1994.

[90] S. Soliman, F. Yuan, and K. Raahemifar. An overview of design techniques for CMOS phase detectors. In *2002 IEEE International Symposium on Circuits and Systems. Proceedings (Cat. No.02CH37353)*. IEEE.

[91] Walt Kester. *Mixed-signal and DSP design techniques*. Newnes, 2003.

[92] John R. Barry. *Digital Communication*. Springer US, 2004.

[93] C.E. Shannon. Communication in the presence of noise. *Proceedings of the IRE*, 37(1):10–21, jan 1949.

[94] J Saniie and M Luukkala. Digital phase detection based on in-phase and quadrature sampling. *Journal of Physics E: Scientific Instruments*, 16(7):606–607, jul 1983.

[95] AMD, Xilinx. Zynq-7000 soc technical reference manual, 2023.

[96] Koheron. Software development kit, 2023.

[97] Claudio E. Calosso and Enrico Rubiola. Phase noise and jitter in digital electronics, 2017.

[98] MathWorks. Power spectral density estimates using fft. https://fr.mathworks.com/help/signal/ug/power-spectral-density-estimates-using-fft.html, 2023.

[99] Arthur Schuster. On the investigation of hidden periodicities with application to a supposed 26 day period of meteorological phenomena. *Journal of Geophysical Research*, 3(1):13, 1898.

[100] Peter Bloomfield. *Fourier Analysis of Time Series An Introduction.* Wiley and Sons, Incorporated, John, 2004.

[101] M. S. Bartlett. Smoothing periodograms from time-series with continuous spectra. *Nature*, 161(4096):686–687, may 1948.

[102] P. Welch. The use of fast fourier transform for the estimation of power spectra: A method based on time averaging over short, modified periodograms. *IEEE Transactions on Audio and Electroacoustics*, 15(2):70–73, jun 1967.

[103] K. Warwick. *An introduction to control systems.* World Scientific, 1996.

[104] D. Hassin and R. Vahldieck. Feedforward linearization of analog modulated laser diodes-theoretical analysis and experimental verification. *IEEE Transactions on Microwave Theory and Techniques*, 41(12):2376–2382, 1993.

[105] Ralf Kohlhaas, Thomas Vanderbruggen, Simon Bernon, Andrea Bertoldi, Arnaud Landragin, and Philippe Bouyer. Robust laser frequency stabilization by serrodyne modulation. *Optics Letters*, 37(6):1005, mar 2012.

[106] Potočnik. Fpga programming. https://antonpotocnik.com/.